SANDIA REPORT

SAND88-0868 • R51533/DD/00082
Nuclear Weapon Data •
Printed July 1989

THIS DOCUMENT CONTAINS

Relative Effectiveness of a Shallow Earth-Penetrating Nuclear Weapon (U)

Archie V. Farnsworth, Jr.

Prepared by
Sandia National Laboratories
Albuquerque, New Mexico 87185 and Livermore, California 94550
for the United States Department of Energy
under Contract DE-AC04-76DP00789

Classified by Paul Yarrington, Supervisor, Computational Physics and Mechanics Division II, 1533, March 10, 1989.

CRITICAL NUCLEAR WEAPON DESIGN INFORMATION
DOD DIRECTIVE 5210.2 APPLIES.

RESTRICTED DATA This document contains Restricted Data as defined in the Atomic Energy Act of 1954. Unauthorized disclosure subject to Administrative and Criminal Sanctions.

SF 2900-QA(8-81)

Issued by Sandia National Laboratories, operated for the United States Department of Energy by Sandia Corporation.

SAND88—0868

Relative Effectiveness of a Shallow Earth-Penetrating Nuclear Weapon (U)

Archie V. Farnsworth, Jr.

Computational Physics and Mechanics Division II
Sandia National Laboratories
Albuquerque, New Mexico 87185

ABSTRACT (U)

We examine here the energy coupling and subsequent material motion resulting from a nuclear burst slightly below the surface of the ground, and compare the results with those for above-ground, near-surface bursts and for the more deeply buried bursts that might characterize a rigid earth-penetrating weapon. Our results show a considerable enhancement in the lethal volume for buried structures in comparison with contact or proximity fused weapons of the same yield, but reduced effectiveness in comparison with more deeply buried bursts. The results are used to construct a curve of effective energy coupling vs. height or depth of burst, using a physically rigorous technique.

THIS PAGE INTENTIONALLY LEFT BLANK

Contents

THIS PAGE INTENTIONALLY LEFT BLANK

List of Figures

List of Figures

1 Introduction

Recent interest in hardened and deeply buried targets in the Soviet Union has made the relative effectiveness of the ground shock produced by various weapons and delivery modes a matter of significant concern. One recent study[1] performed at Sandia National Laboratories (SNL) compares the ground shock effectiveness for contact and proximity fused options for the W88/Mk5, while another study[2] at this laboratory addresses bursts at the fairly deep depths typical of a rigid earth-penetrating weapon (EPW). The present study concerns the energy coupling effectiveness and resulting ground shock propagation for a nuclear burst at a shallow depth of burial ($\sim$ 1 m), where the total prompt coupling of the weapon energy to the ground cannot be assumed *a priori*.

This work was done in conjunction with the studies of References 1 and 2 to produce a relatively complete study of the effect of height and depth of burst, with other parameters (e.g. yield, geology, etc.) held constant. We use the present results with those from the other studies, to form a self-consistent curve of energy promptly coupled to the ground as a function of height/depth of burst.

The suggestion of shallow earth penetration by a ballistic missile-delivered warhead has been discussed recently, starting in the DNA community[3], and early work[4] there suggested that a substantial gain in hard target kill probability was possible over that for an above ground burst. The work reported here confirms those early findings. While this work was largely motivated by these early suggestions, the work has application not only for a weapon designed to be a shallow EPW, but also as a special case of a rigid EPW which fails to penetrate deeply because of a hard geology, or hard rubble encountered above the ground.

The two-dimensional (2-D) hydrocodes used for this work are the Lagrangian radiation/hydrodynamics code LASNEX[5] at Los Alamos National Laboratory (LANL), and the Eulerian radiation/hydrodynamics code CSQ[6] at SNL. The LASNEX code is used for very early problem times ($\lesssim 10^{-7}$s) when radiation flow and energy cou-

pling to ground are the dominant physical processes and deformations are relatively small. This code features several options for radiation transport, including multi-group diffusion and implicit Monte-Carlo (IMC) techniques for one- or two-dimensional calculations, and the P_n moment method for one-dimensional studies. (A discussion of the implications of choosing different radiation transfer methods for weapon effects studies is found in the appendices of Reference 7. Briefly summarizing, the coupling to ground through air is best done using IMC, fairly well done using multi-group diffusion, and very poorly done using single group diffusion.) The CSQ hydrocode treats radiation transport using single group diffusion, which is adequate for the later times when hydrodynamic response to the deposited energy and wave propagation are the dominant physical processes, and the energy coupling by radiation has been essentially accomplished. Because it is Eulerian, and provides models for handling finite material strength and fracture, the CSQ hydrocode is useful for the later portions of the calculation, when distortions are large and strength effects become important.

For this study, we have chosen to minimize physical complexities (such as a layered geology) that might obscure the enhancement of early time energy coupling resulting from shallow burial of the device. To this end, a homogeneous geology of saturated tuff[8] was selected. This simple geology allows rigorous scaling comparisons with other

DOD b(3)

DOE b(3)

This report emphasizes both the present computational results, and comparisons with results reported elsewhere[1,2] for calculations at different heights and depths of burst, to provide a measure of the enhancement resulting from burial of the device before explosion.

2 Initial Conditions

We describe here the initial setup for the early part of the shallow buried burst calculation with the LASNEX hydrocode, including the hole, the secondary model[7], device debris outside the secondary, and the surrounding environment of ground and air. We also describe our motivations for the choices made.

The shallow earth penetrator Impactor Coupling Enhancement (ICE) concept that provided much of the original motivation for this work, was envisioned as a ballistic missile-delivered system in which a slender rod-like forebody of the reentry vehicle (RV) would strike the ground at hypersonic speed, clearing a path a short distance into the ground for the explosive system to follow, as the rod wore away (see Figure 1). It was presumed that such a reentry vehicle would strike the ground at a fairly shallow angle such that the path of the warhead into the ground would be about twice its burial depth of approximately one meter. The system would then detonate before being destroyed by the forces of ground impact. Thus, at the moment of explosion, the nuclear device may rest one meter below ground surface, but the hole through which some of the device energy is lost by radiation could be two meters or more in length at the slant angle of entry.

DOE
b(3)

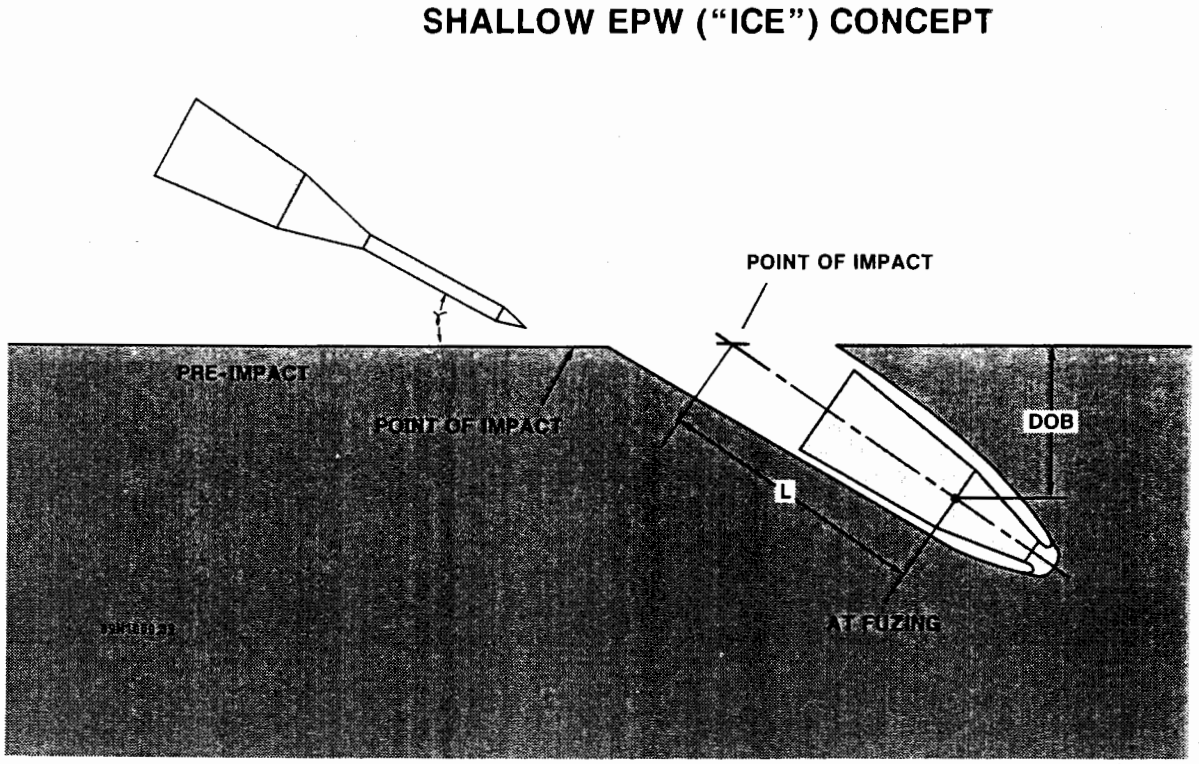

Figure 1: The concept of the proposed "ICE" shallow earth penetrator.

DOE
b(3)

In the model description that follows, numerous simplifying assumptions have been employed. While reasons exist for each of these, no claim of uniqueness or "correctness" is made for our particular choices. Much uncertainty existed at the time of the initiation of this work, both as to the design of a shallow earth penetrating weapon system, and the configuration of the entry hole. The assumptions described here are thought by the author to be reasonable, to both address the dominant physics issues and to obtain a numerically tractable calculation.

DOE
b(3)

The assumption of a homogeneous distribution of materials in the hole ignores the possibility of preferential paths in the debris for the loss of radiation to the atmosphere. One assumes however that a system specifically designed as a shallow earth penetrator would include design features to minimize such radiative losses. The debris surrounding the lower part of the secondary has a somewhat higher density than the average of 0.3

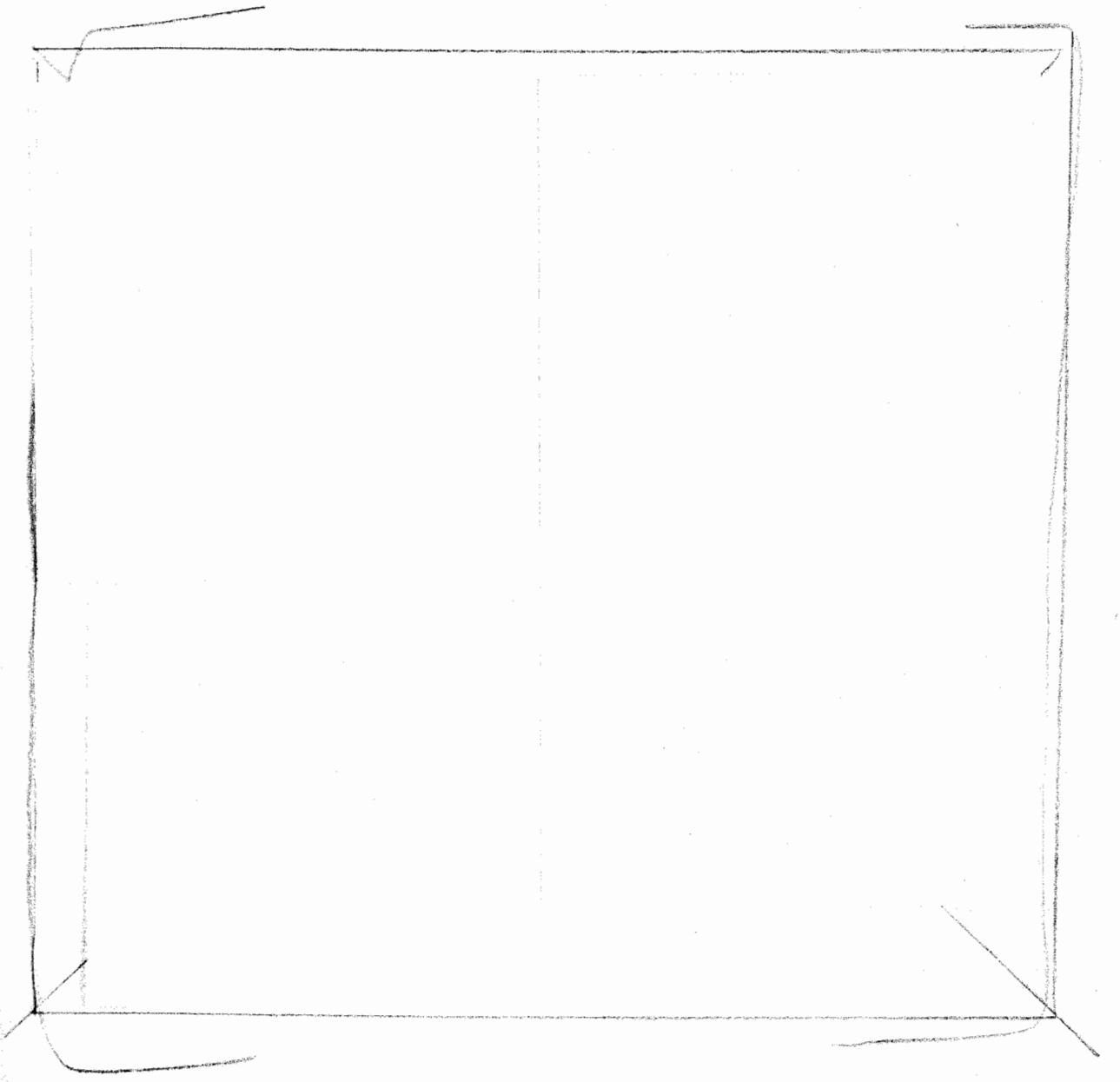

DOE
b(3)

Figure 2: Initial region boundaries and grid for LASNEX calculation.

Mg/m^3 (0.3 g/cm^3) assumed elsewhere in the hole. This seems reasonable because of the confining walls; however, the values used were chosen for numerical convenience. Some numerical experimentation has been performed varying the assumptions of density and properties of the material filling the hole. The results suggest only modest sensitivity to such changes in initial assumptions (see Appendix 1).

DOE
b(3)

Mg/m^3 (0.3 g/cm^3) assumed elsewhere in the hole. This seems reasonable because of the confining walls; however, the values used were chosen for numerical convenience. Some numerical experimentation has been performed varying the assumptions of density and properties of the material filling the hole. The results suggest only modest sensitivity to such changes in initial assumptions (see Appendix 1).

DOE
b(3)

3 The LASNEX Calculation of Energy Coupling

The LASNEX grid employed for the early part of the calculation is shown in Figures 2 and 3. Details of the LASNEX grid and other input instructions are found in Appendix 2.

The deposition of energy in the secondary source model is described in Reference 7. We summarize here by noting that energy is deposited in the various layers of the secondary with specified time dependencies, and allowed to flow self-consistently after deposition. At the early times calculated with LASNEX, energy transport by radiation dominates, since the rapid energy production rates interior to the device lead to high temperatures and therefore high radiative fluxes. The heating of the surrounding ground and air by radiation flow is illustrated by the time sequence of temperature contours shown in Figure 4. The transport of radiation is performed using multigroup diffusion in the deep interior of the source model, regions 1 – 3 of Table I, and using an implicit Monte-Carlo method outside those regions. This combination seems to produce the best present estimate of radiant energy coupling to ground from a nuclear device. (See Appendix 1 of Reference 7 for a comparison of energy coupling with differing transport models.)

DOE
b(3)

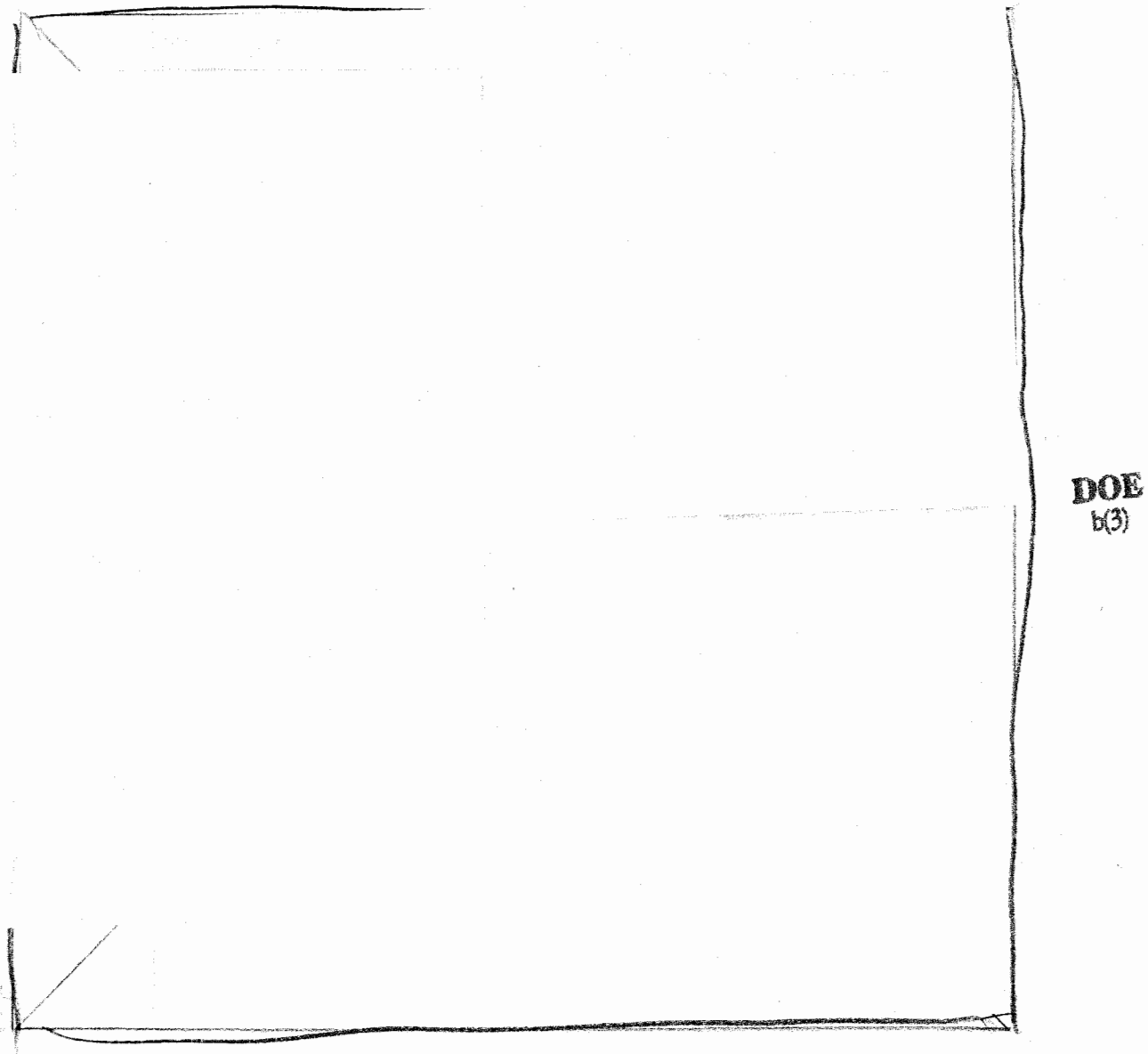

Figure 3: Detail of the LASNEX grid near the explosive device.

Figure 4: Sequence of temperature contours showing early energy deposition. The contours labeled A - F correspond to .1, .3, 1, 1.5, 2, 3 keV temperatures respectively.

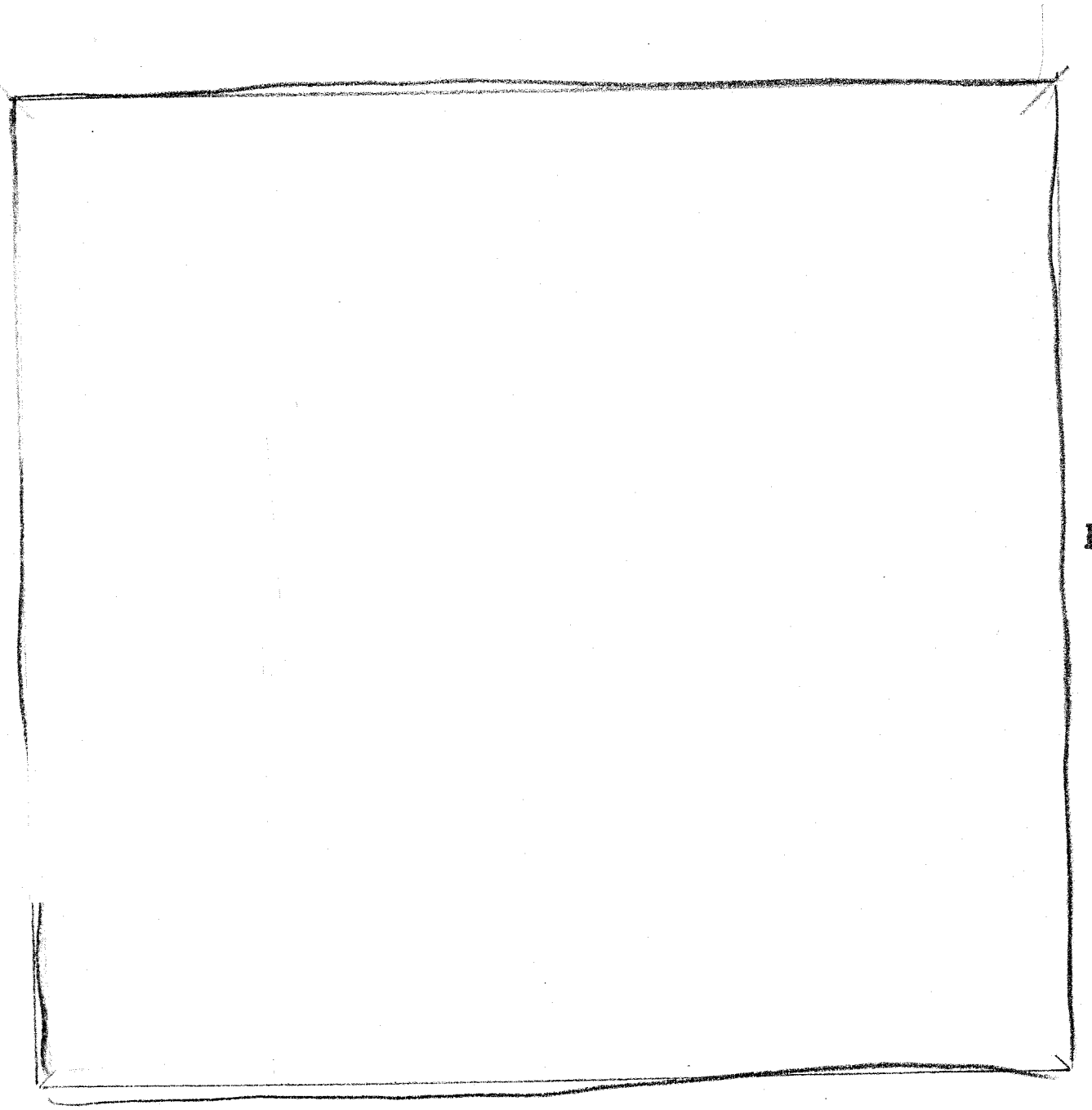

DOE
b(3)

Figure 5: Time history of early energy deposition in various materials.

After the first few tens of nanoseconds of the problem, the extremely rapid changes associated with the prompt energy release of the device are concluded and the radiation transport process becomes quite diffusive.

DOE
b(3)

The pressure, temperature, and density of the materials in the heated region are plotted as functions of depth on axis in Figure 6.

DOE
b(3)

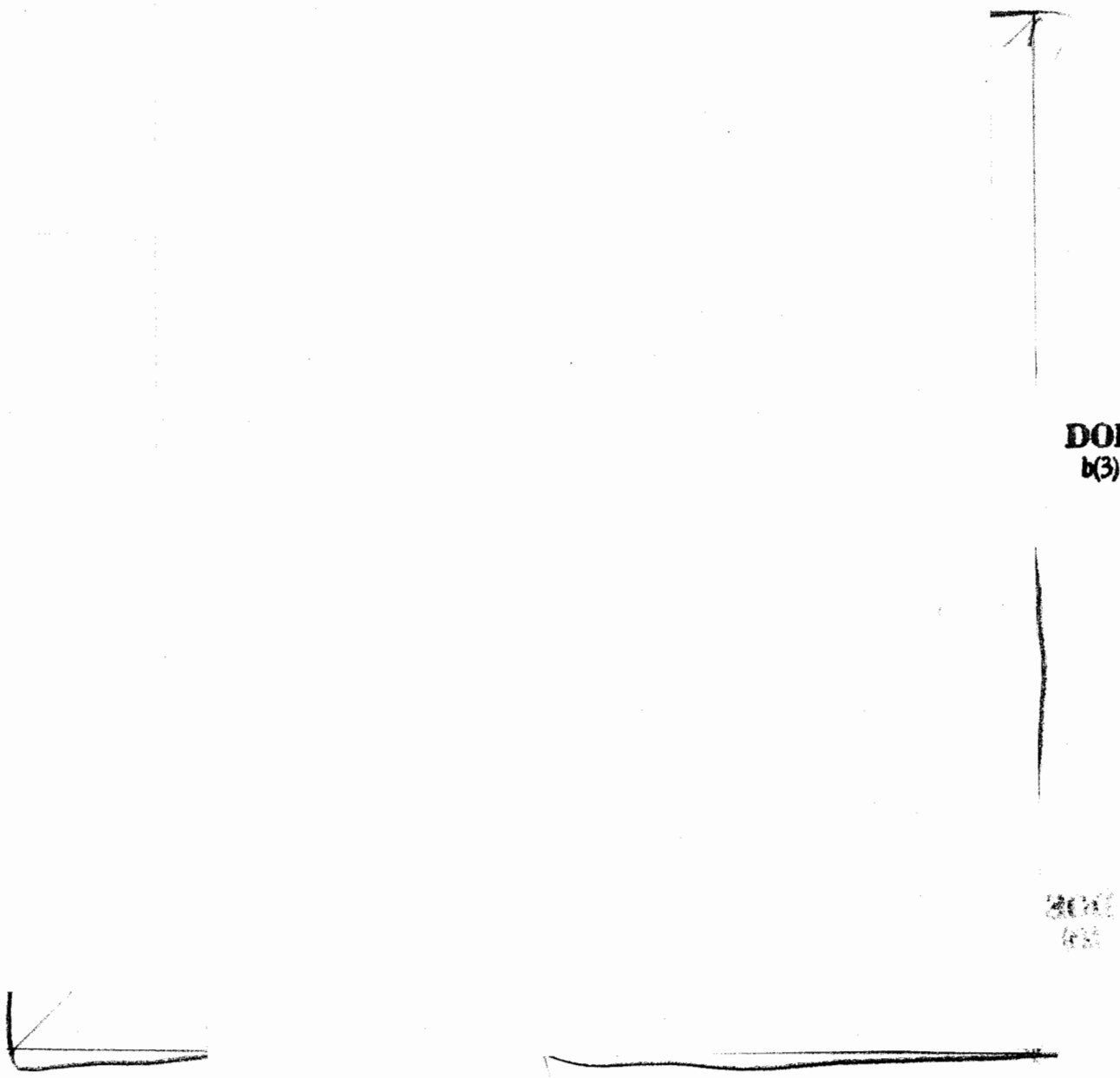

Figure 6: Pressure, density, and temperature vs. depth on axis, at link time.

4 Linking to CSQ

The process of linking the LASNEX results to the CSQ hydrocode is done with the aid of the LASTRAN[10] code. Data read from the LASNEX "universal" dump includes the coordinates of each LASNEX cell, the mass density, temperatures (electron, ion, and radiation), pressure, and the energies of each cell (kinetic, electron, ion, and radiation), as well as the cell corner velocities in the radial and axial directions. The LASTRAN code prepares this data in a CSQ readable file, along with other options specified by the user.

DOE b(3)

The procedures used preserve the mass, momentum, and internal energy very well.

DOE b(3)

The calculations of hydrodynamic response and wave propagation with the Eulerian CSQ hydrocode required ten submissions, separated by hand rezones to adapt the mesh

to the constantly expanding domain of the problem. A consistent zoning philosophy was employed, which we now describe.

DOE
b(3)

5 A Discussion of Phenomena

In this section, we are concerned with the phenomena associated with the shallow buried burst, many of which are different, qualitatively or quantitatively, from those encountered in either above-surface bursts or bursts at greater depths of burial. For completeness, we include here some items already touched upon in earlier sections. For additional detail on some phenomena, beyond the present discussion, the interested reader is referred to Appendix 4.

As previously indicated, the phenomena associated with delivery and burial of the explosive device establish the environment or initial conditions which affect subsequent developments. The conditions that have been assumed for this calculation are believed to adequately describe a shallow nuclear burst from either an ICE hypersonic delivery system, or a cruise-missile-delivered or aircraft-dropped, parachute-retarded system that fails to penetrate deeply.

DOE
b(3)

DOE
b(3)

DOE
b(3)

DOE
b(3)

Figure 7: Density, temperature and horizontal velocity vs. horizontal range at 0.6 μs,

DOE
b(3)

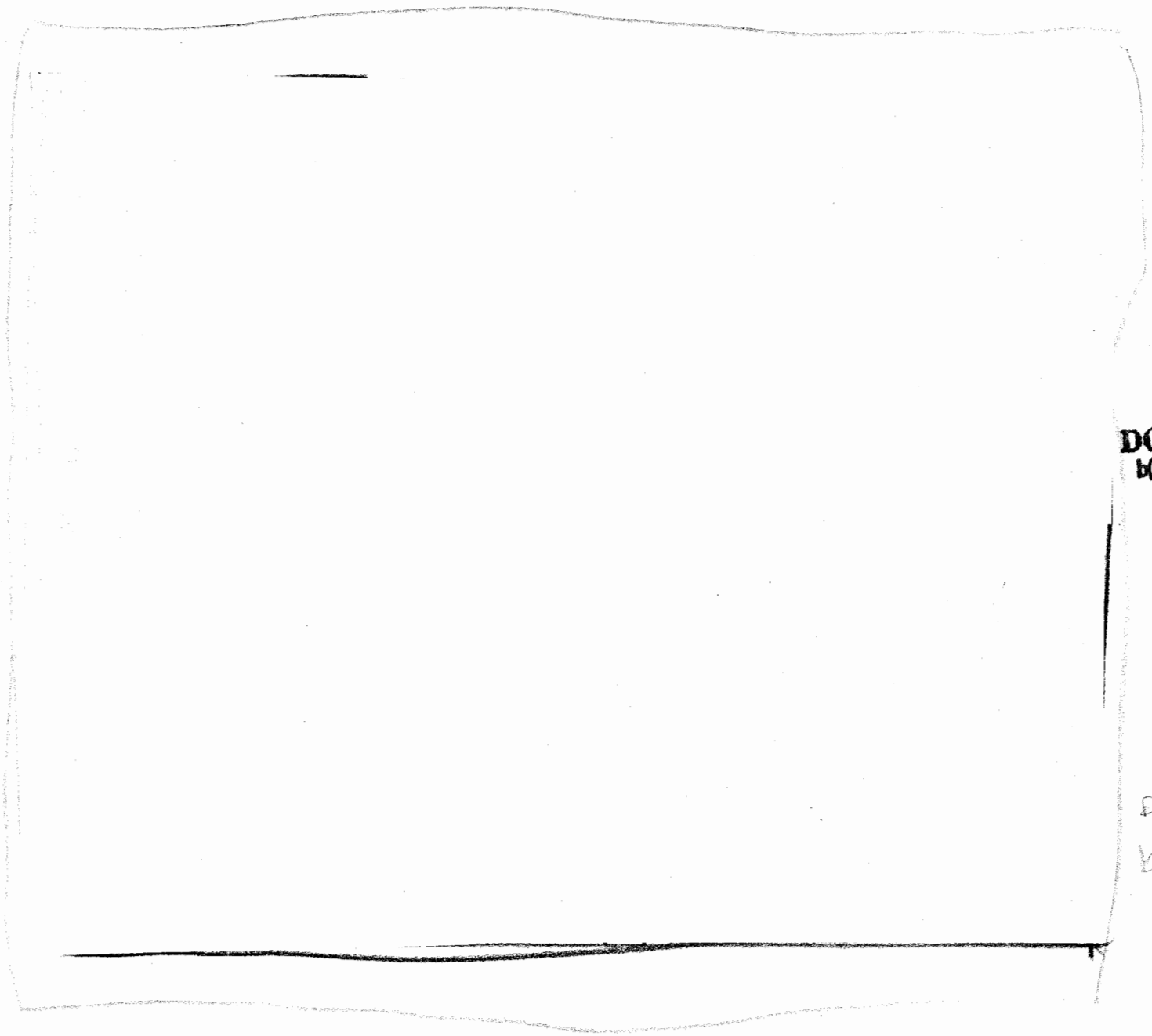

DOE
b(3)

DOE
b(3)

Figure 8: Comparison of conditions at link time, 66 ns, (left) and 1μs, right.

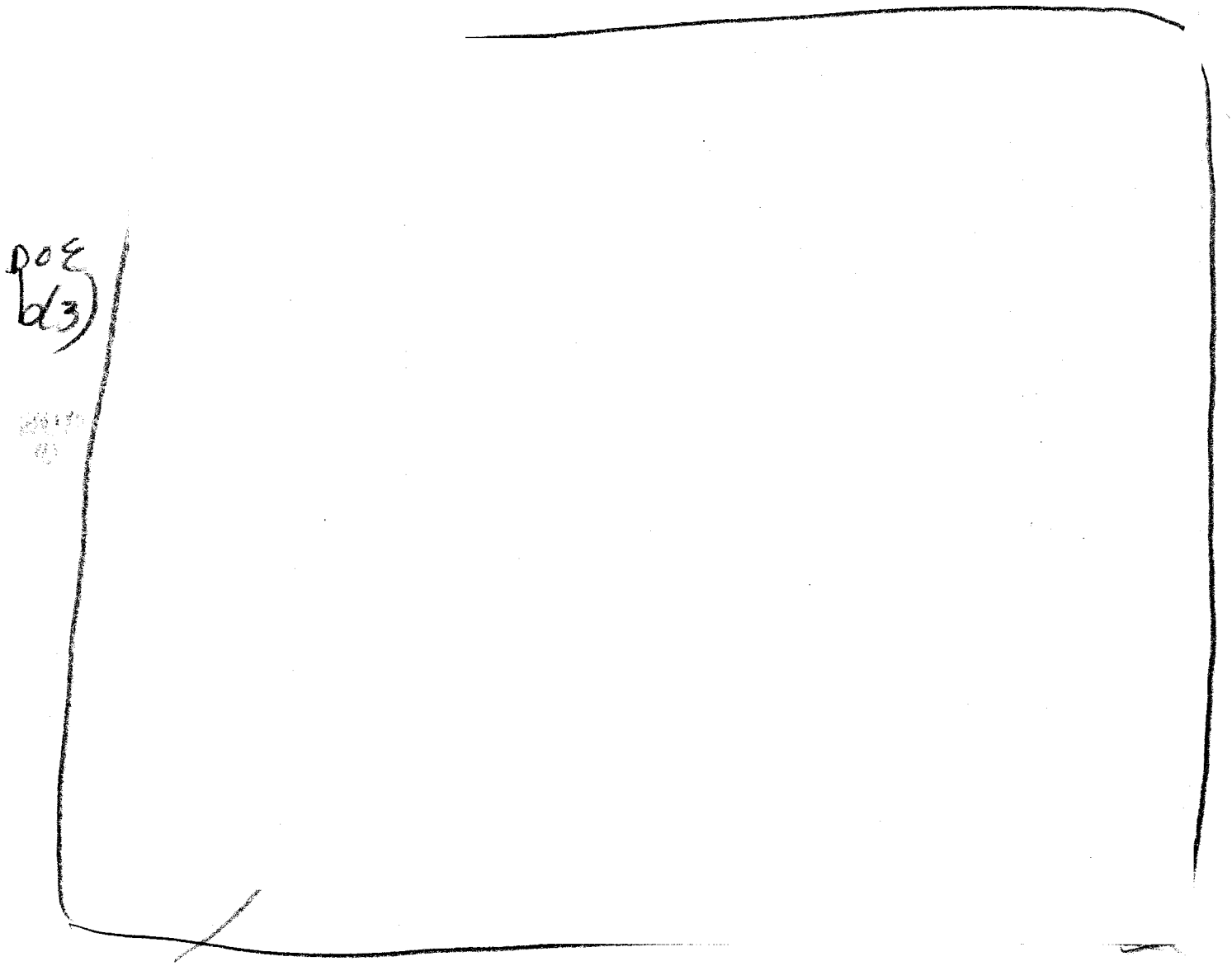

Figure 9: Distance vs. time diagram for features down the axis. Shown here are the locations of the radiative temperature front, the shock wave pressure peak, and cavity density edge, as functions of time.

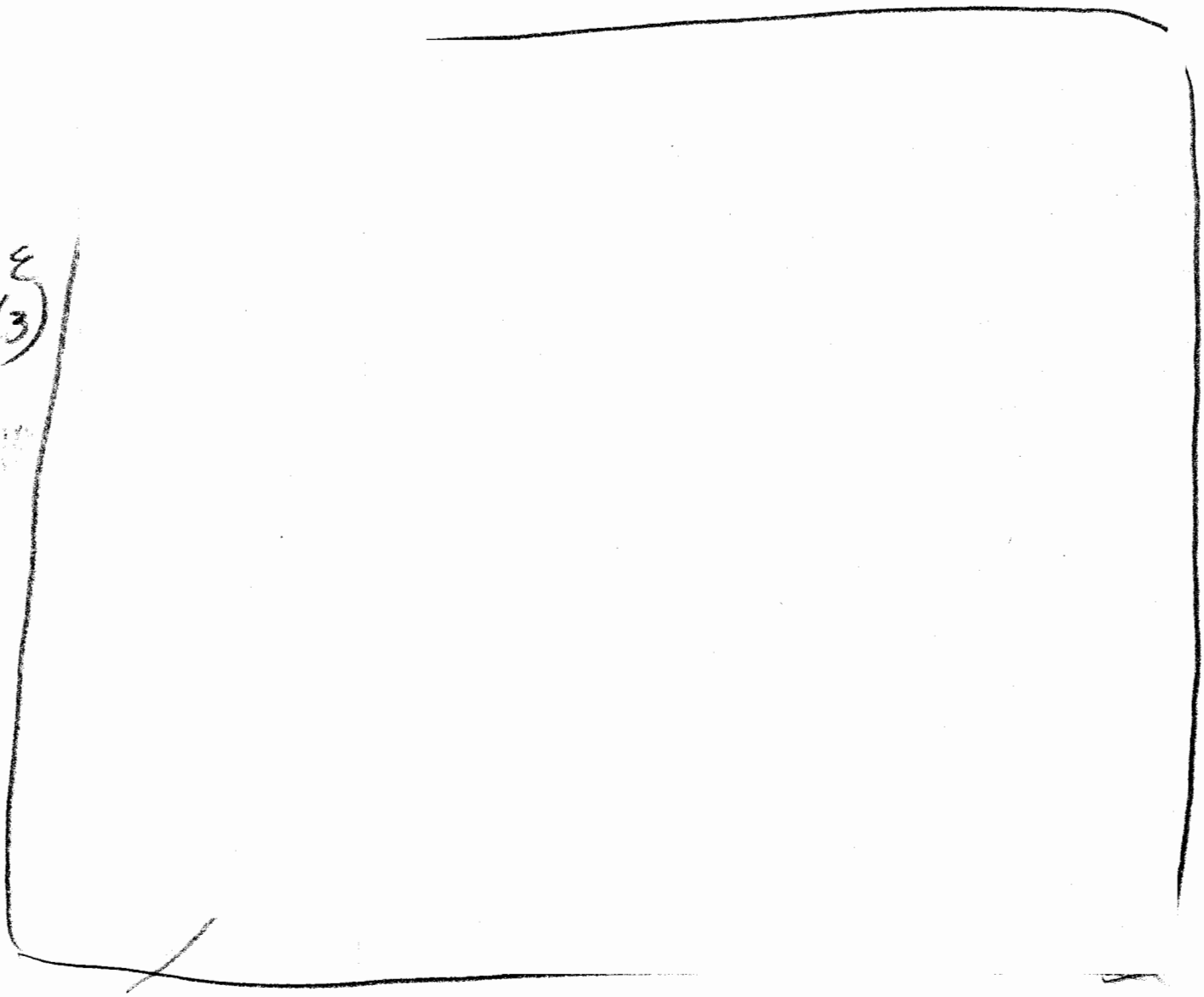

Figure 9: Distance vs. time diagram for features down the axis. Shown here are the locations of the radiative temperature front, the shock wave pressure peak, and cavity density edge, as functions of time.

DOE
b(3)

Figure 11: The shocked material and cavity at 10 μs.

DOE
(b)(3)

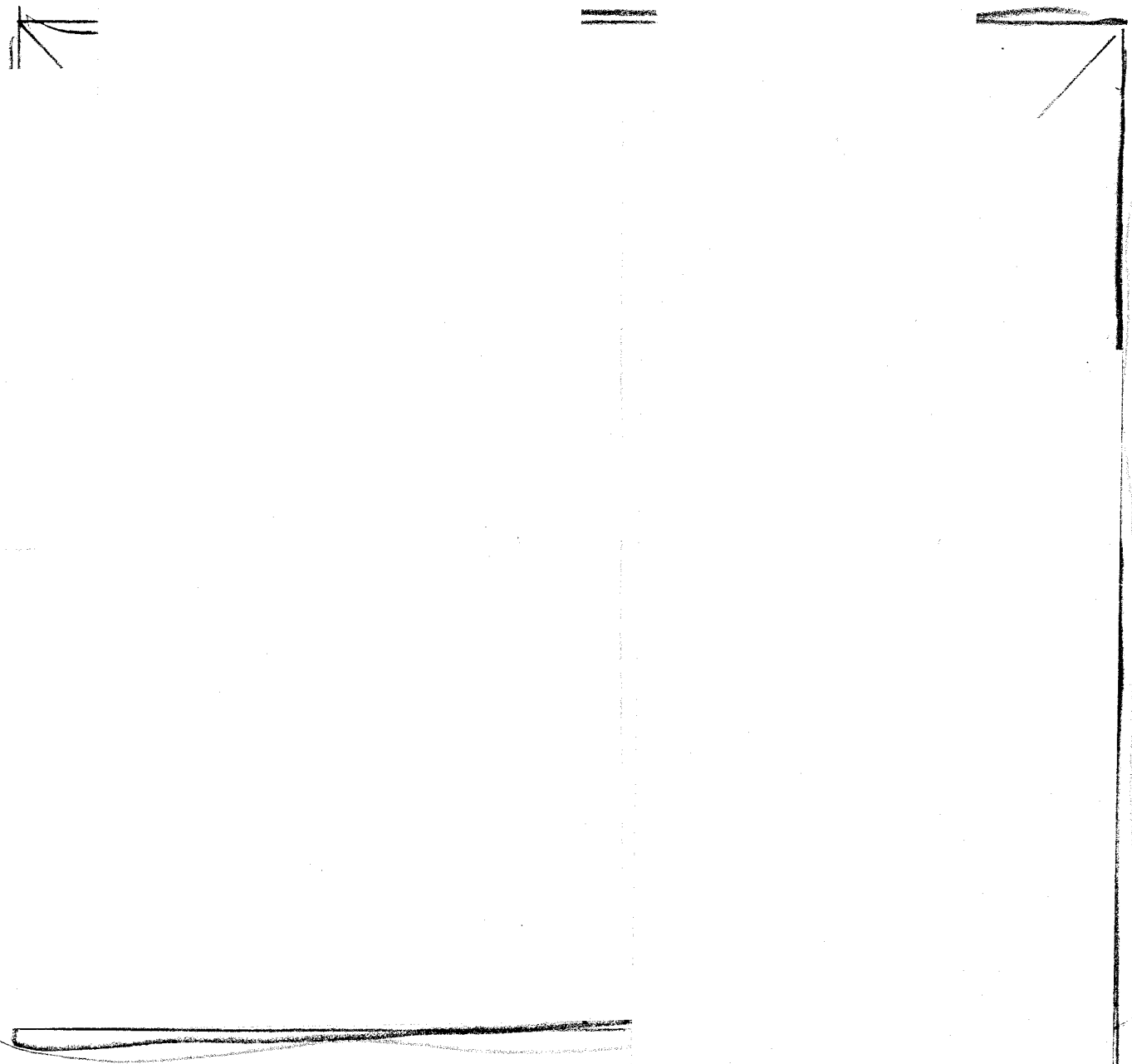

Figure 12: The radiative fireball in air at 10 μs.

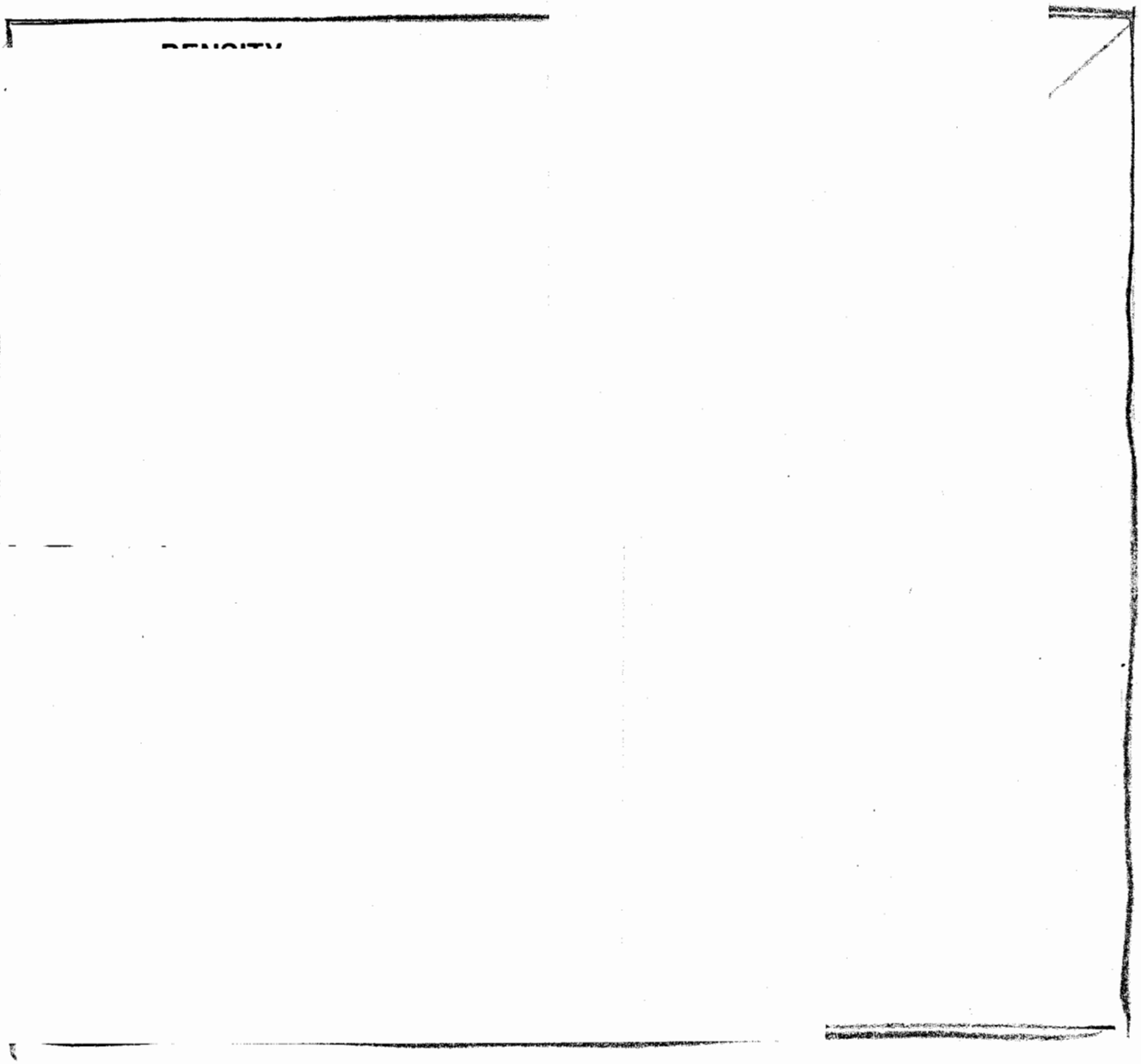

Figure 14: Pressure, density, and temperature vs. depth on axis at 50 μs.

DOE
(b)(3)

DOE
b(3)

Figure 15: The airblast, and shock induced ground cavity at 100 μs,

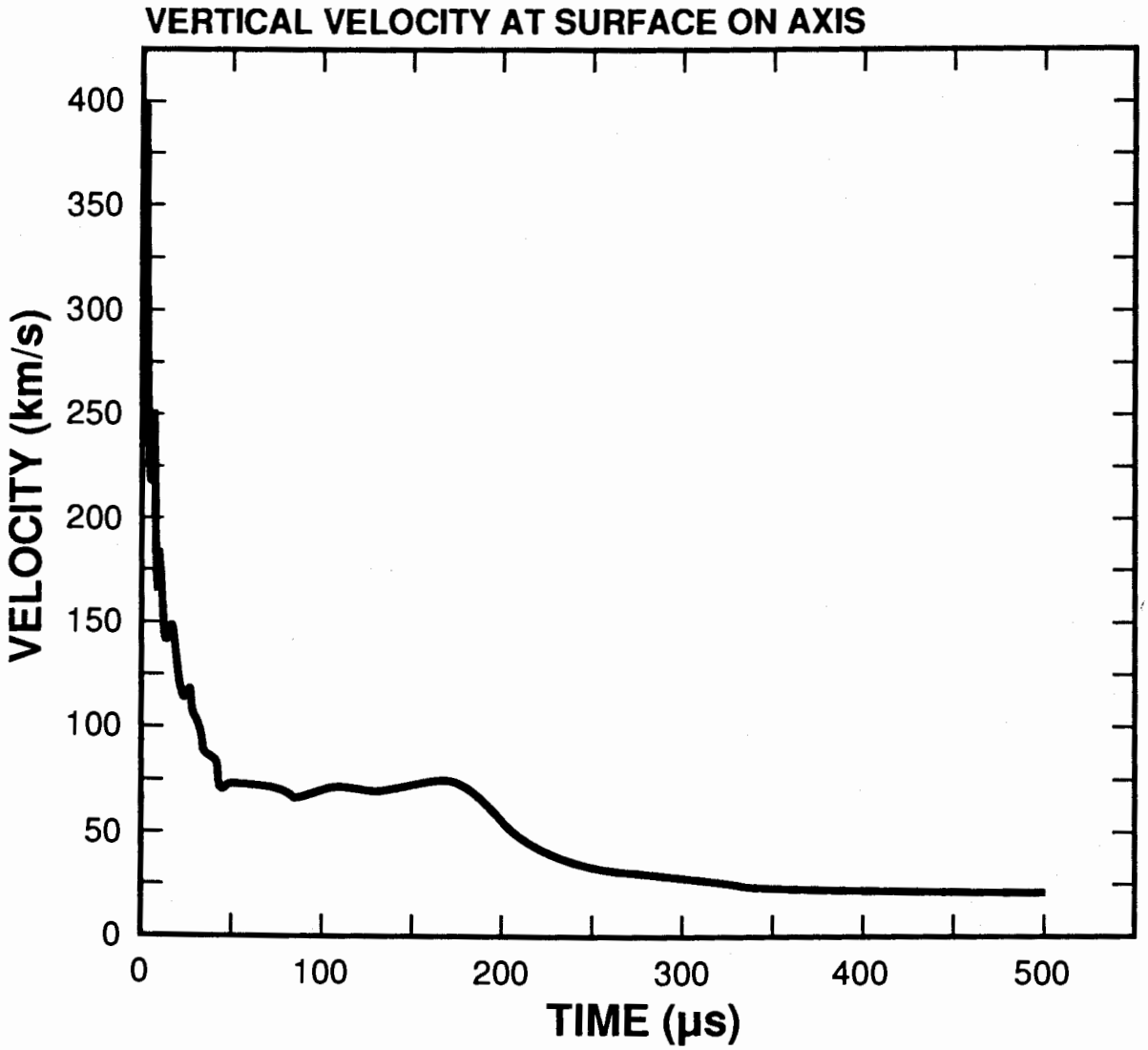

Figure 16: Velocity history at the ground surface, centerline location.

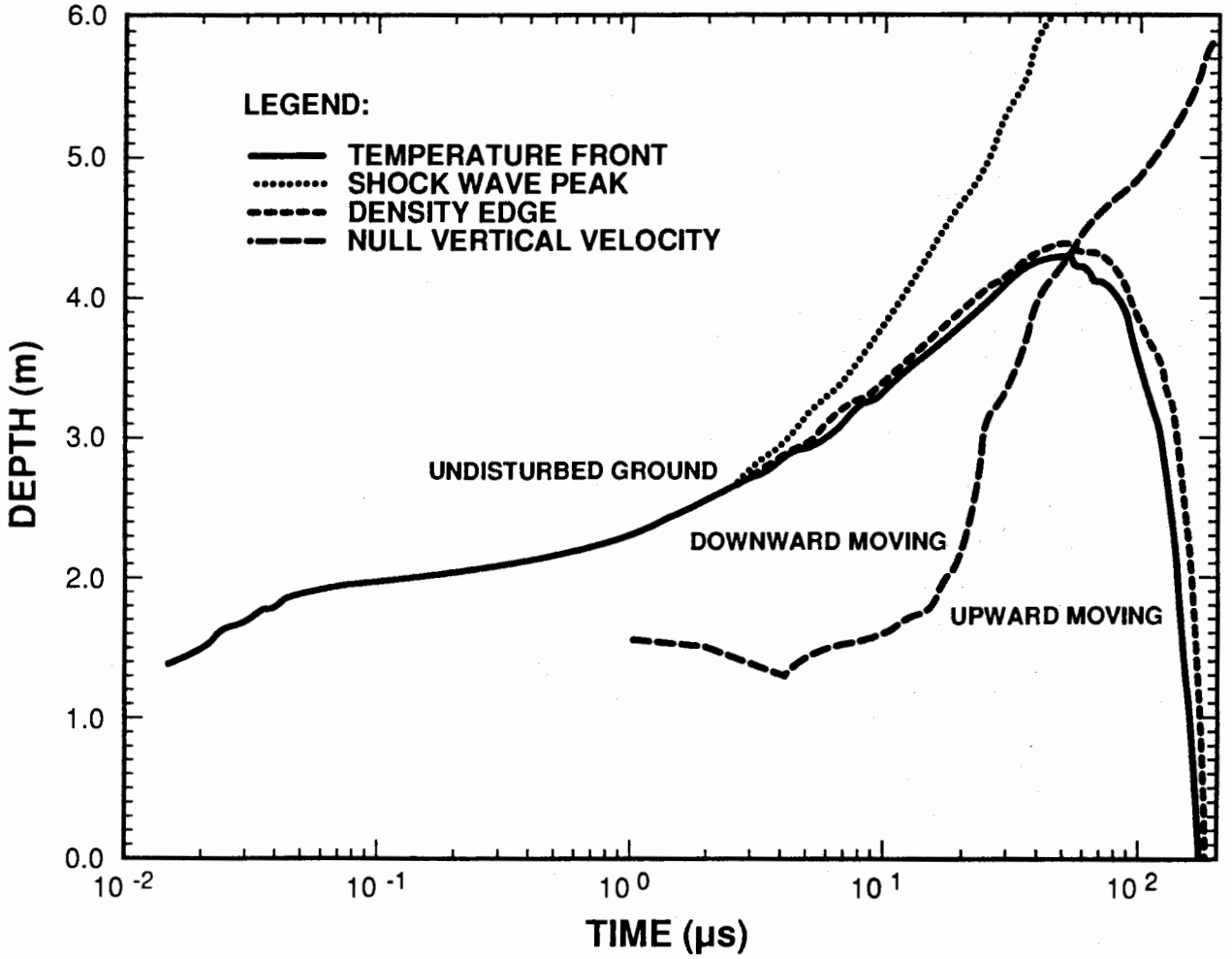

Figure 17: Depth vs. time diagram for phenomenologic features down axis.

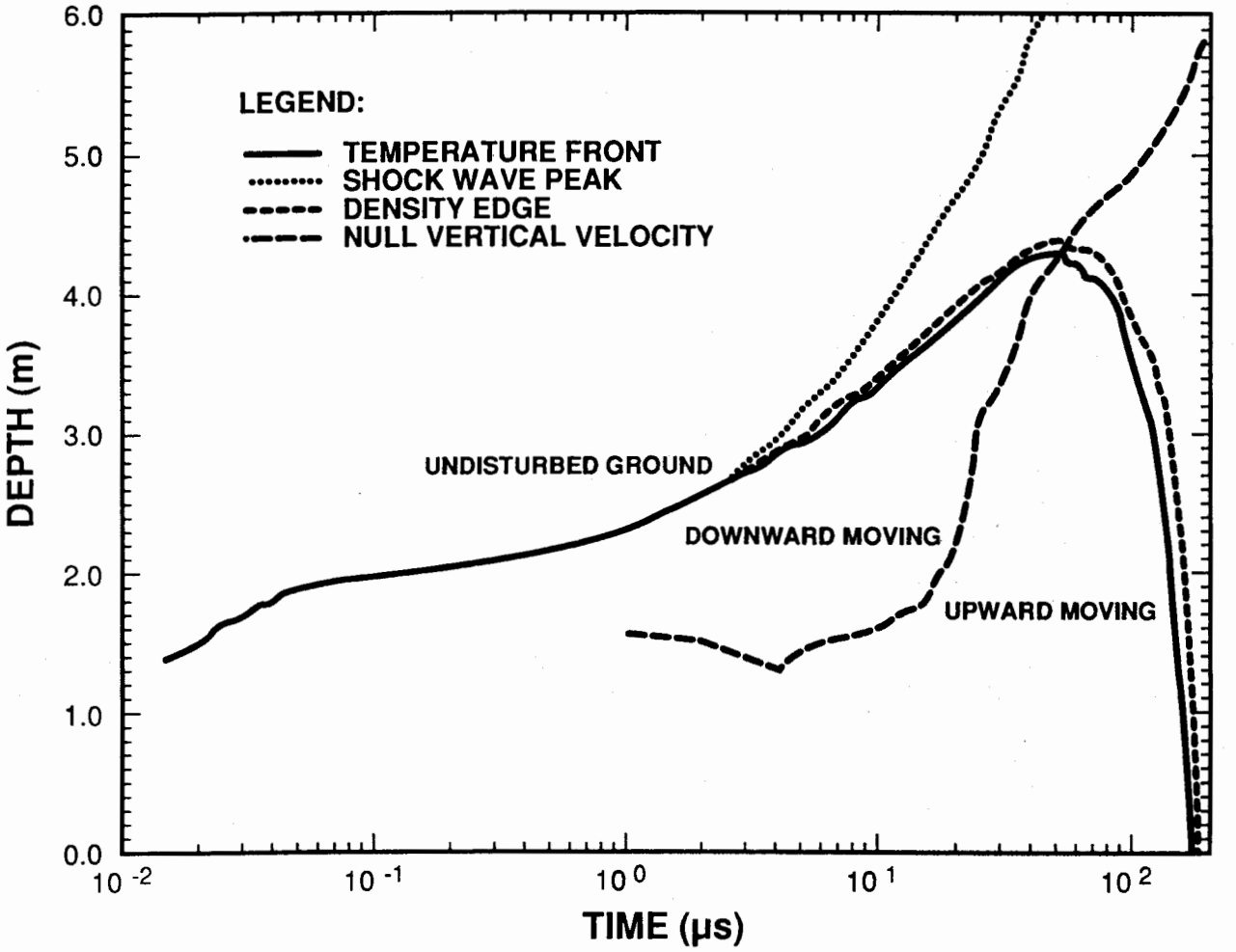

Figure 17: Depth vs. time diagram for phenomenologic features down axis.

[redacted] During this same time interval, the air shock continues to expand under the influence of the warm ejected tuff. The pressure (left) and temperature (right) contours as well as the material interfaces of Figures 19 and 20 show the structure of the above surface phenomena.

[redacted]

In Figure 24, the airblast peak pressure attenuation with range, at several heights, is compared with a reference airblast attenuation curve for a slightly above surface (contact) burst of 250 kT, due to Brode[12]. The lack of smoothness seen in the curves for this calculation results from the late time ejection of higher density, lower temperature, aggregations of tuff, that pass through regions of the grid out of pressure equilibrium

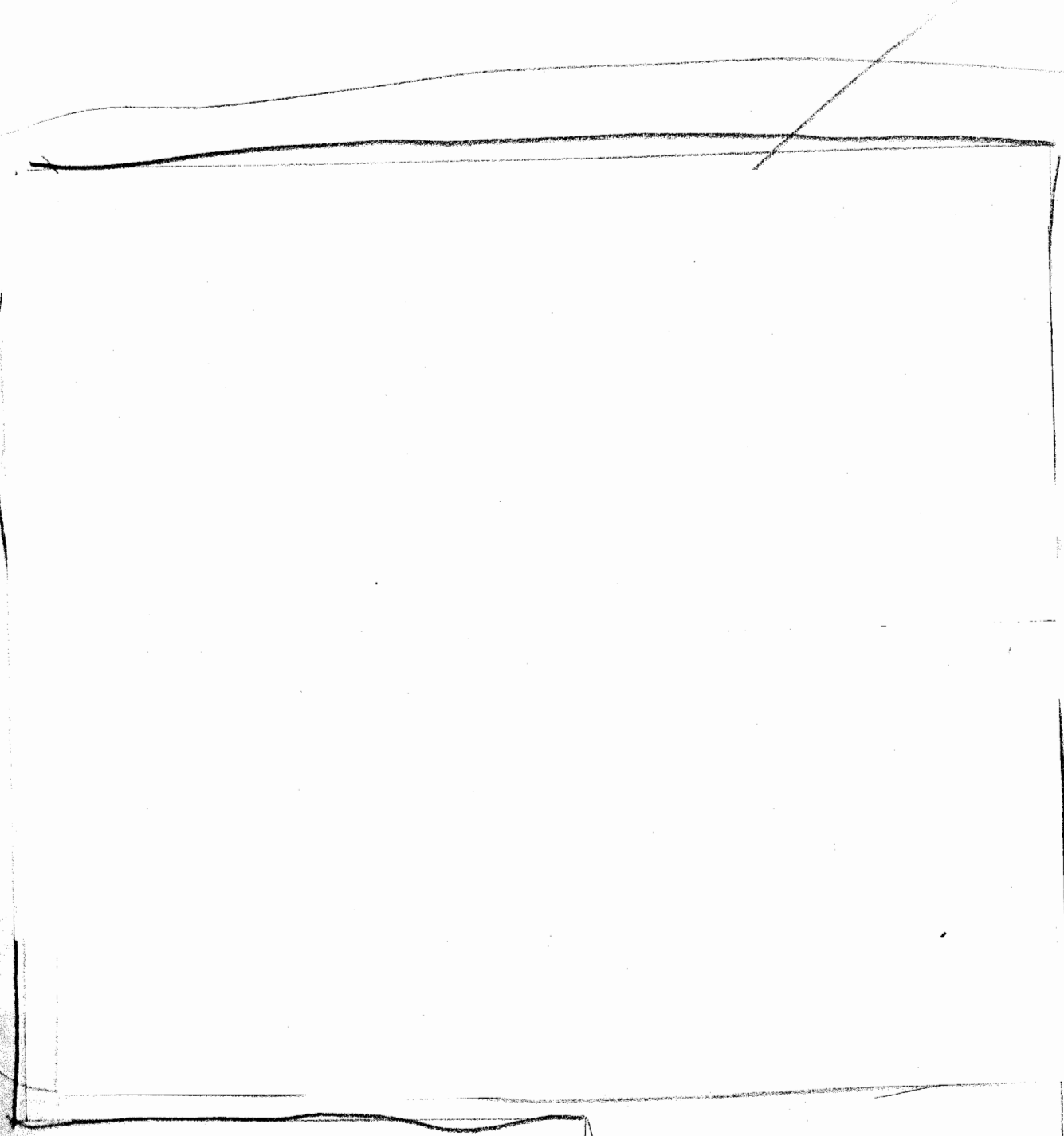

DOE
b(3)

Figure 19: Ground shock and airblast at 1.6 ms.

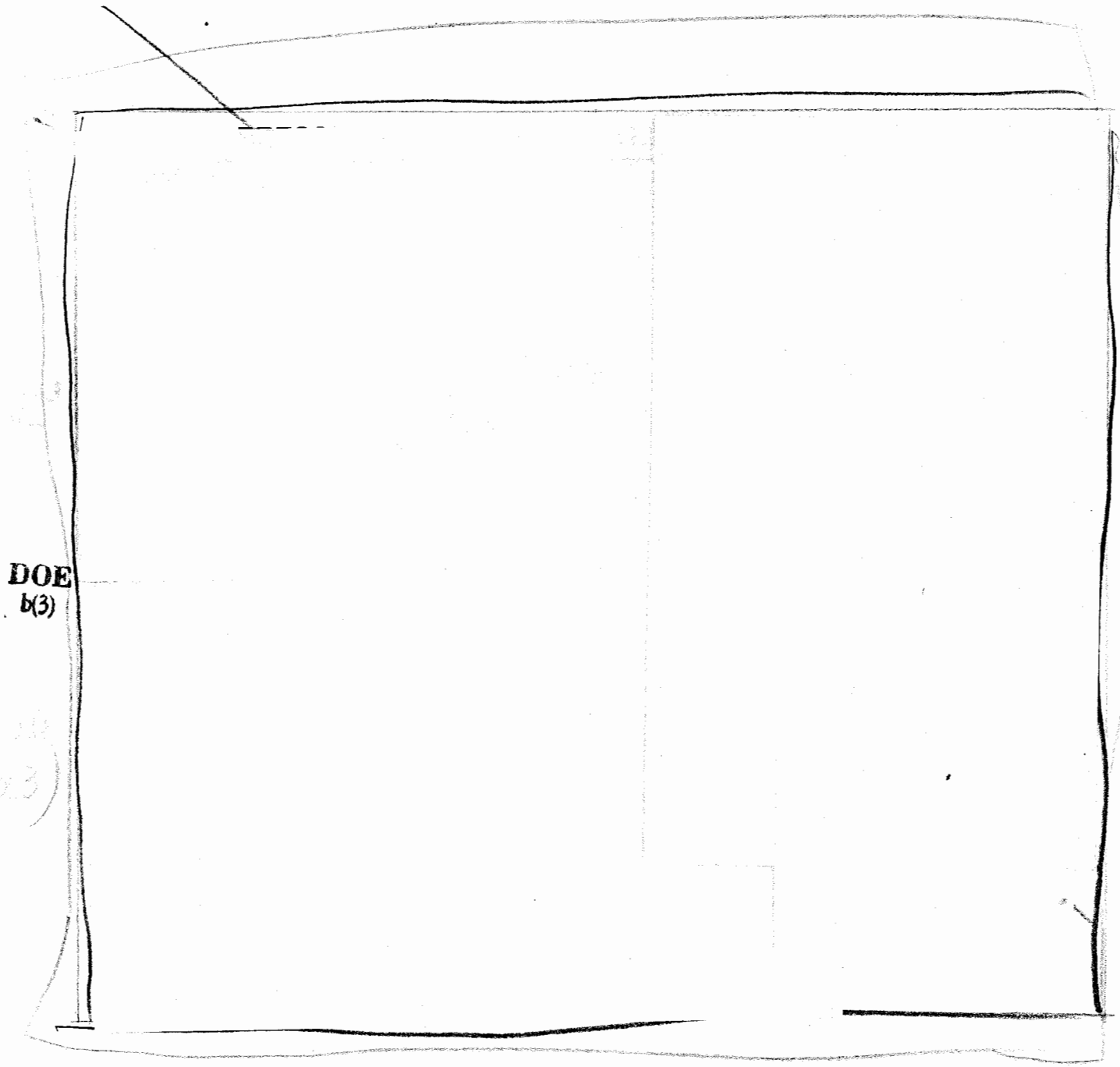

Figure 20: Ground shock and airblast at 10 ms, with pressure (left) and temperature (right) contours illustrated.

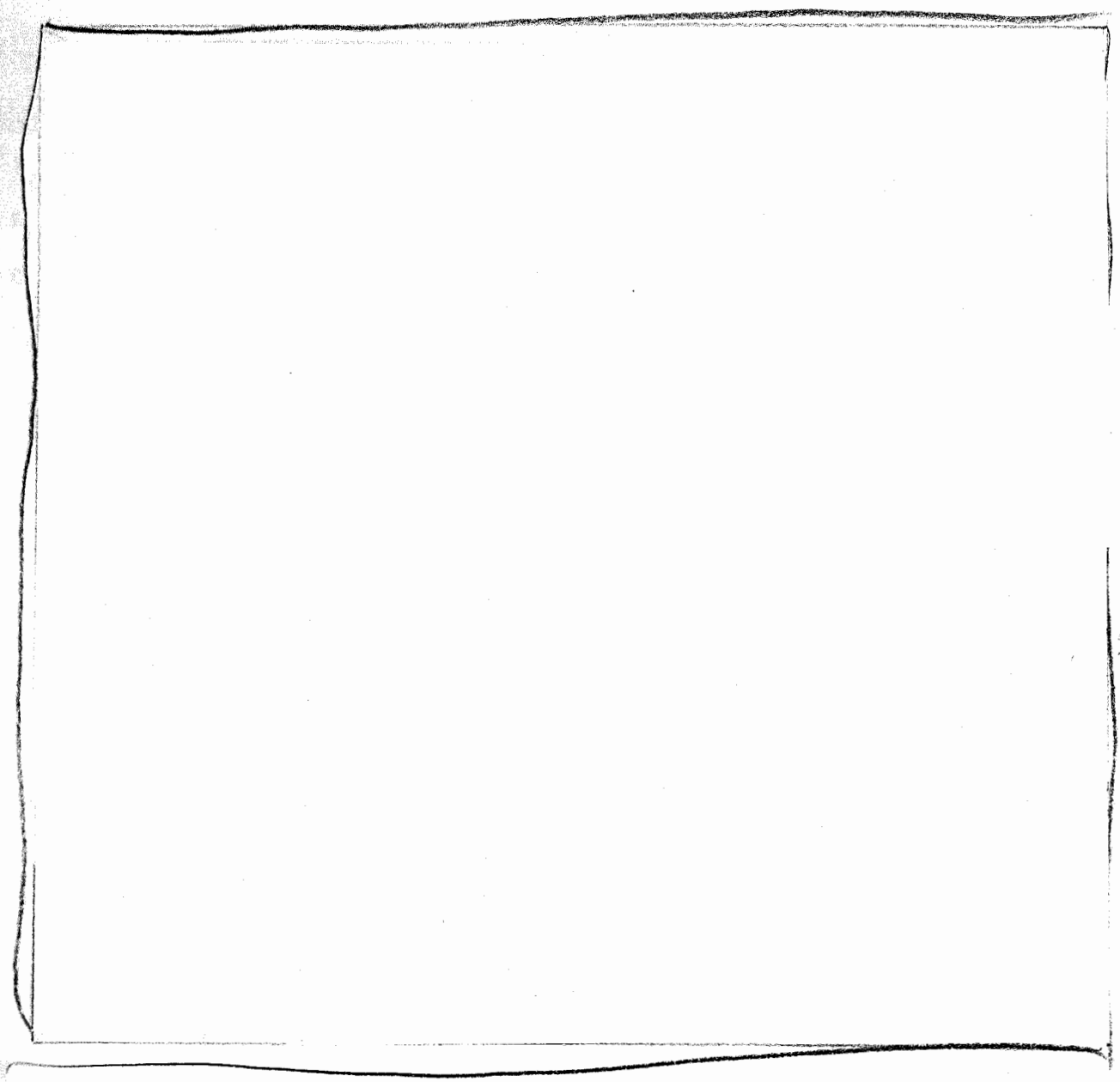

Figure 21: Pressure, density, and velocity profiles on axis in air at 10 ms.

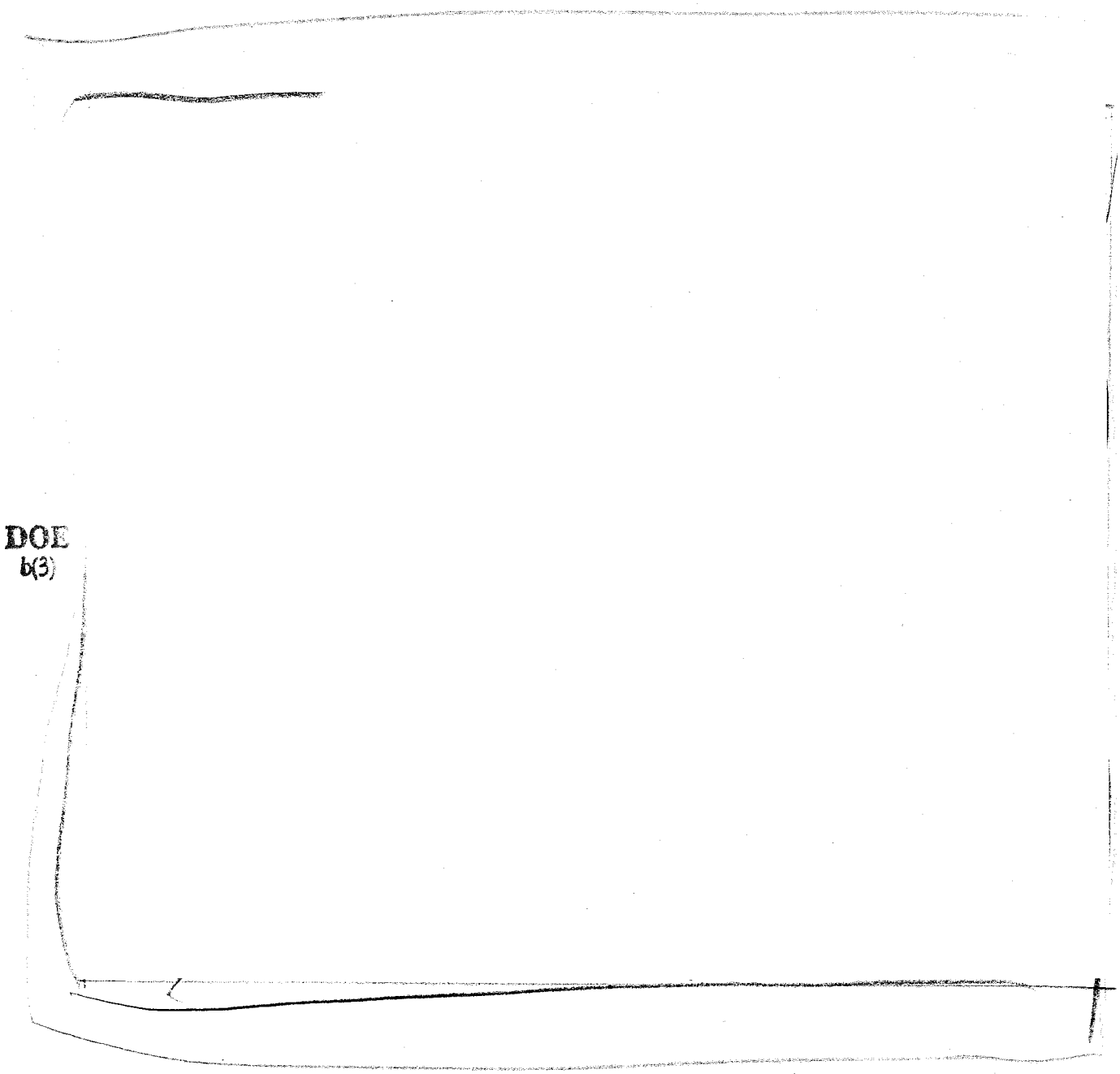

Figure 22: Ground shock and airblast at end of calculation, 0.2 s. The contour in ground is pressure, while contours in air are temperatures.

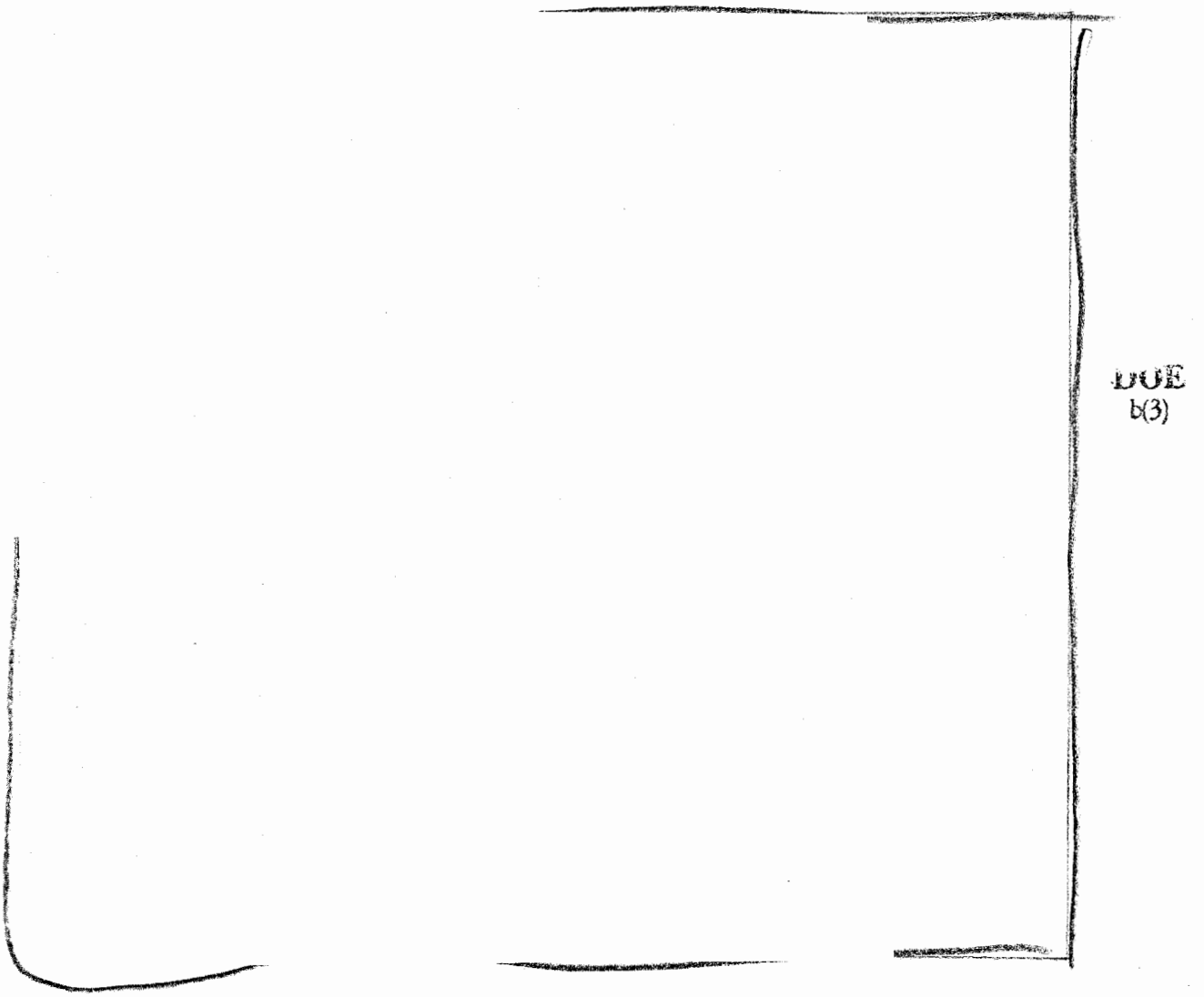

Figure 23: Vertical stress history on axis, 500 m below ground surface.

with the surrounding air. The overall comparison with the Brode reference curve, however, is rather good, and suggests that this shallow burst provides essentially half of its energy in airblast effects. It must be remembered, however, that the Brode curve describes an airblast that is driven by the prompt deposition of energy, almost entirely delivered by radiation, at very early time, whereas in the present calculation the energy reaches the atmosphere over a very much longer period of time, largely through the work done by the expansion of heated tuff.

Contours of maximum vertical stress in the ground for this calculation are shown in Figure 25. These contours represent the regions within which all points were subjected to at least the levels of vertical stress noted. The contour quantities are time independent, although they are displayed against the background of a dot density plot of mass density at 0.2 seconds, the concluding time of the calculation. Peak horizontal stresses, peak vertical velocities and peak horizontal velocities are similarly displayed in Figures 26-28, respectively.

DOE
b(3)
+
b(1)
1.5(e):X2

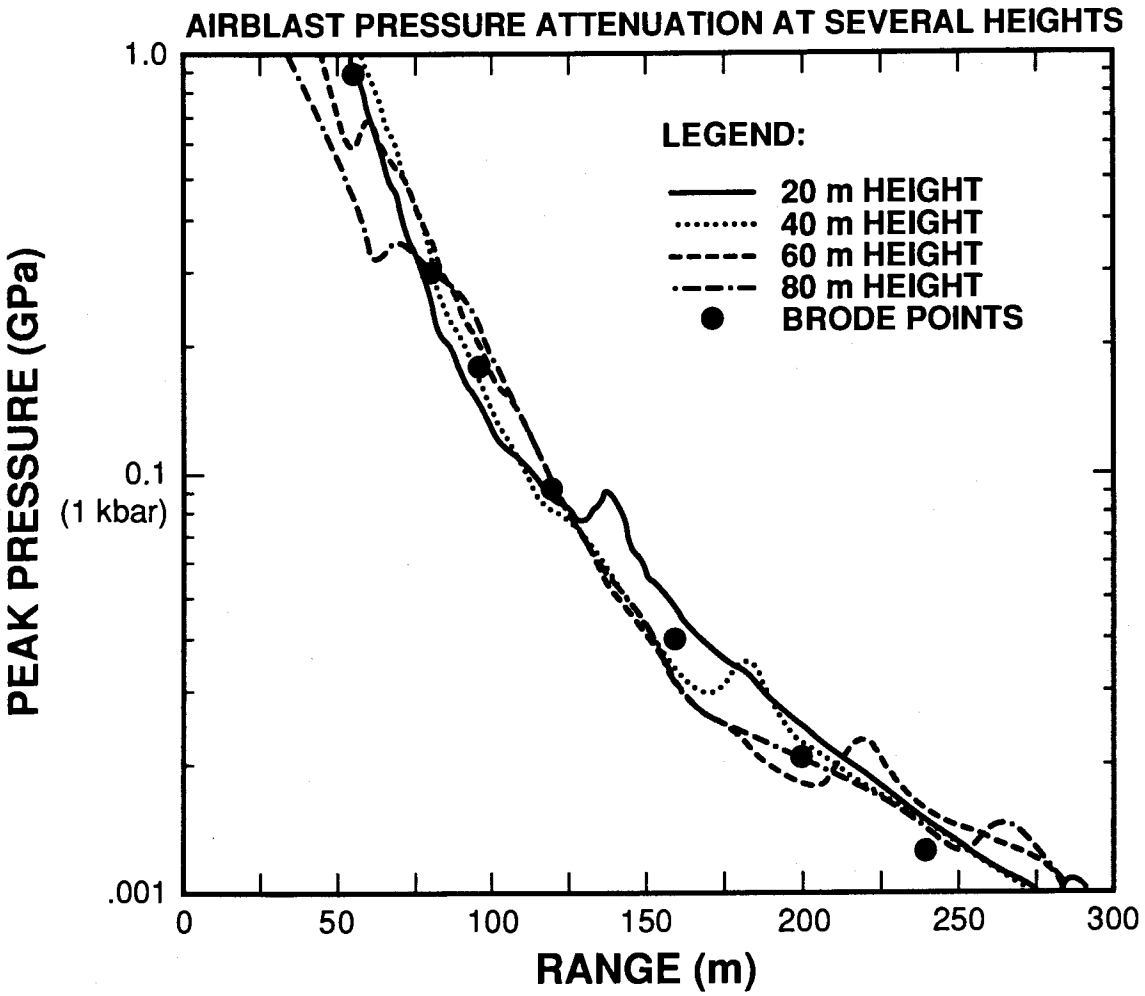

Figure 24: Airblast pressure attenuation with range, at several heights, compared with the Brode airblast results for a 250 kT burst slightly above the surface.

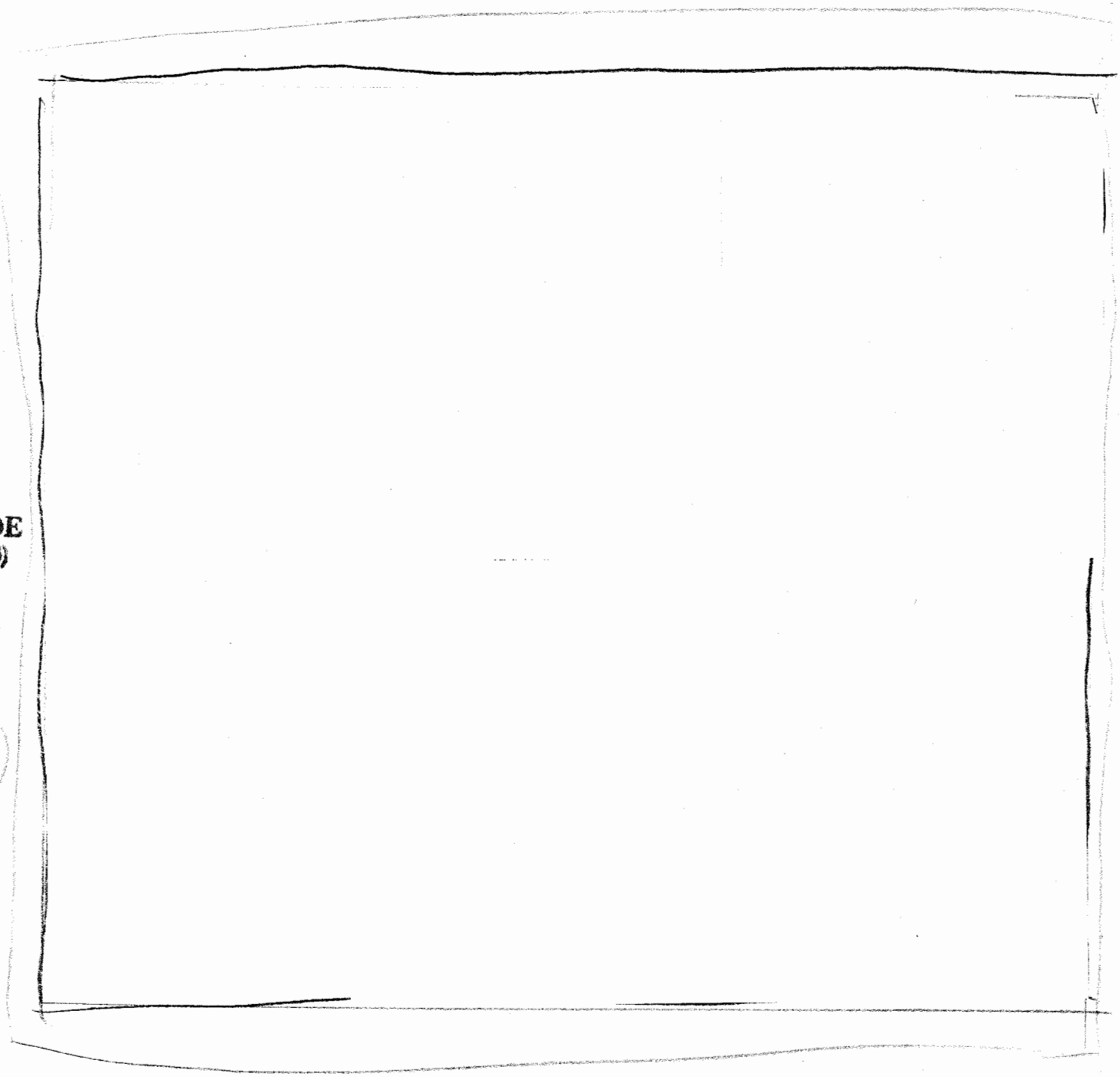

Figure 25: Contours of peak vertical stress in air and ground.

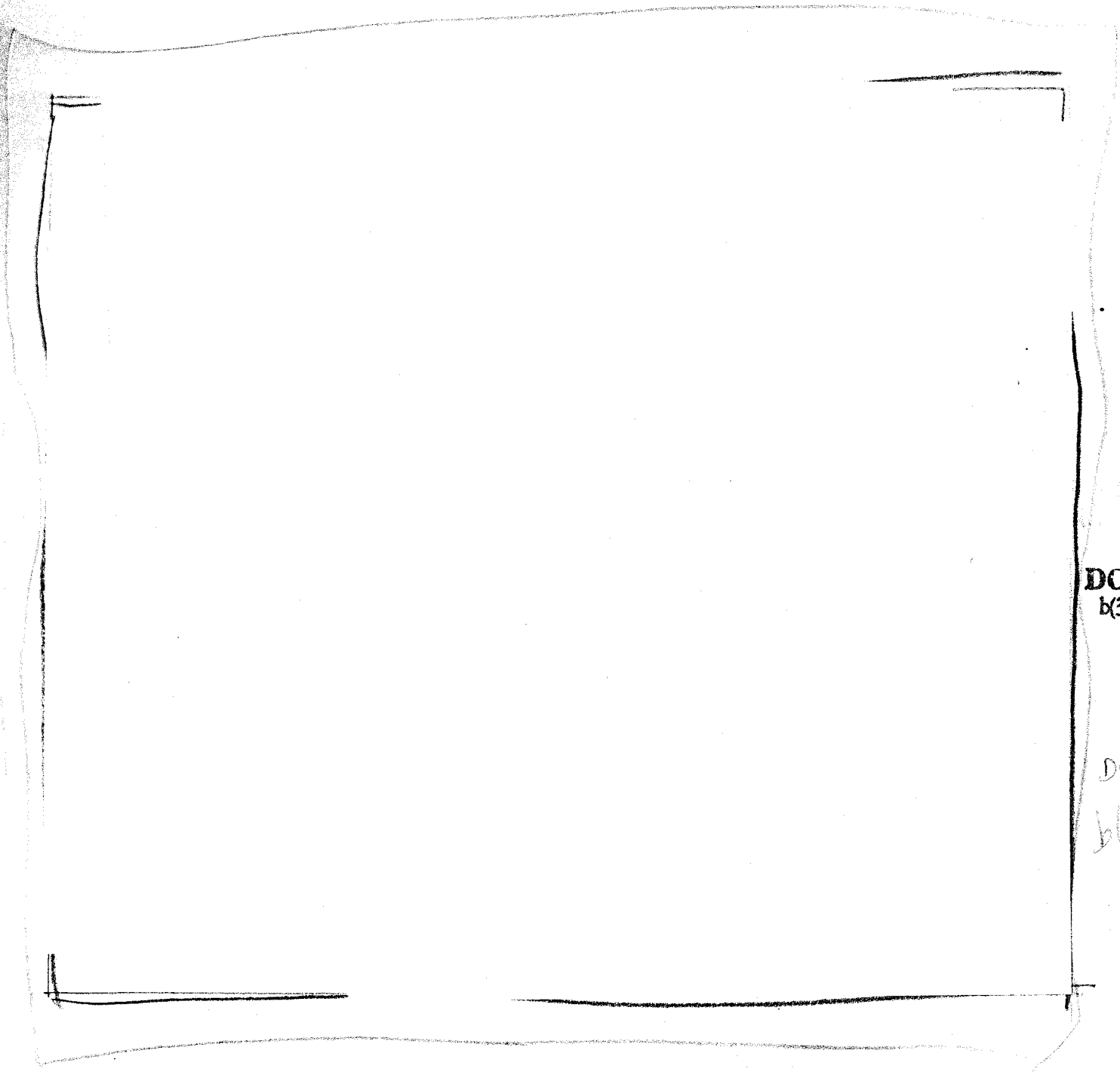

Figure 26: Contours of peak horizontal stress in air and ground.

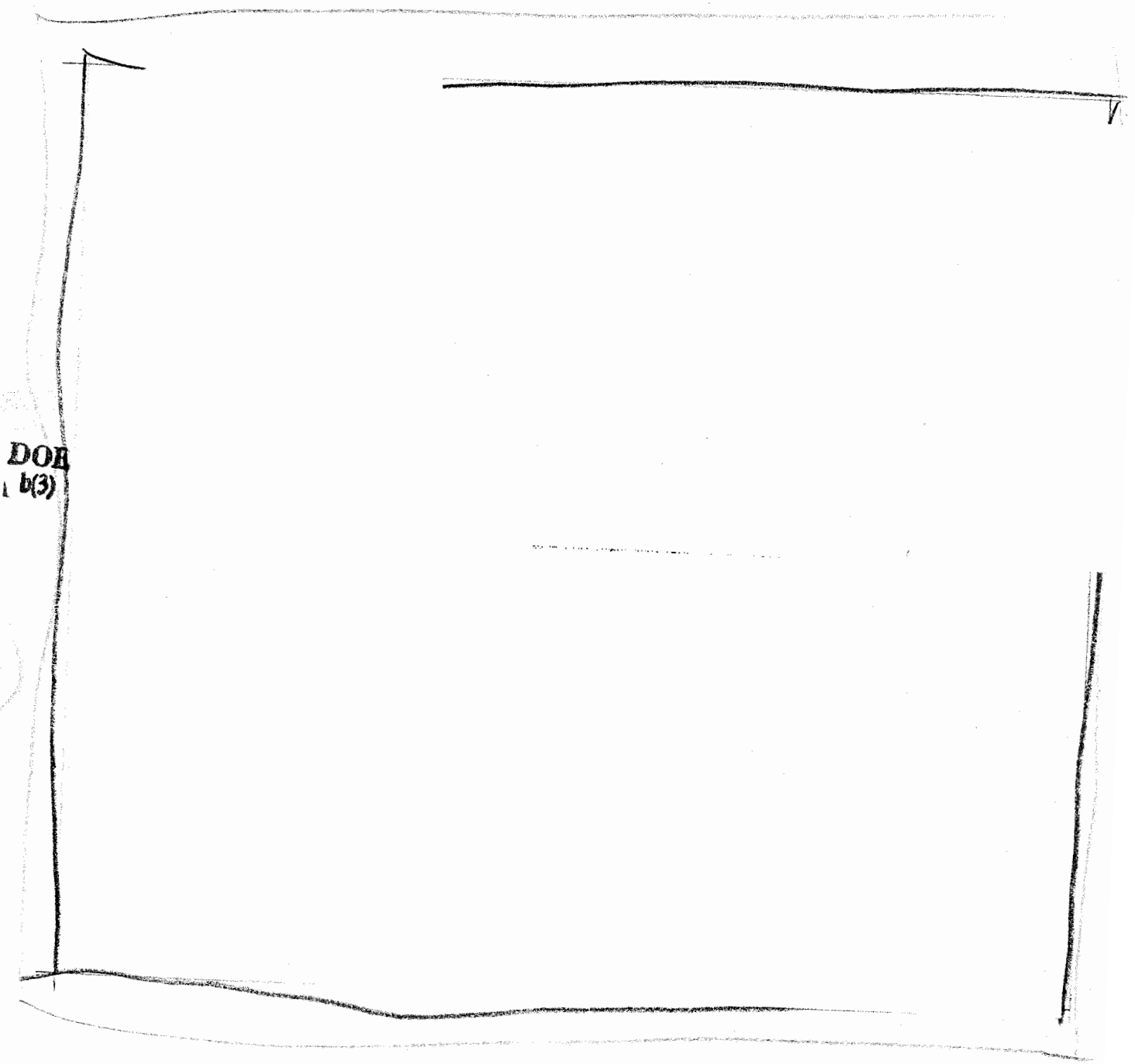

Figure 27: Contours of peak vertical velocity.

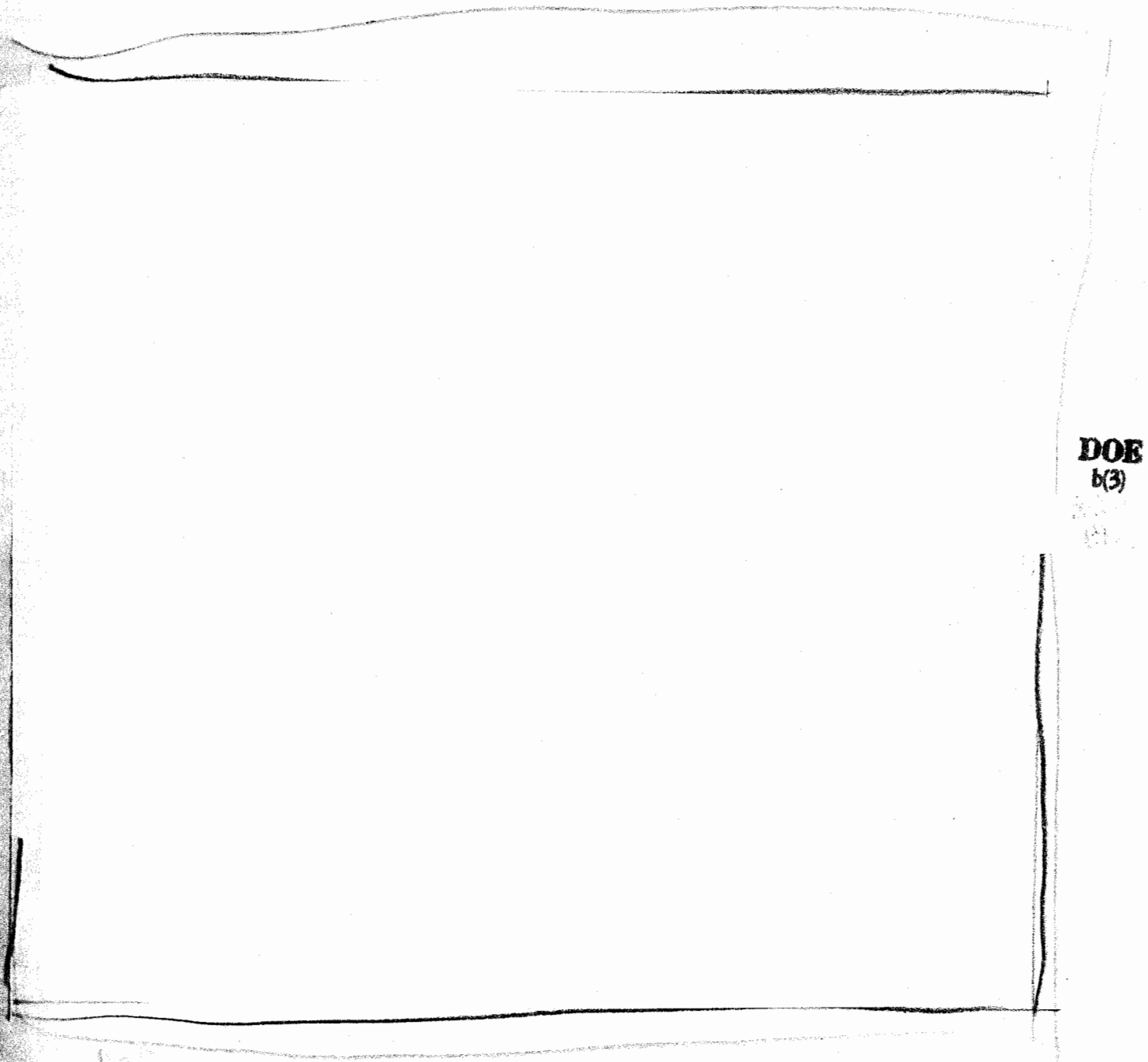

Figure 28: Contours of peak horizontal velocity.

Figure 29: Vertical stress histories at several points down axis.

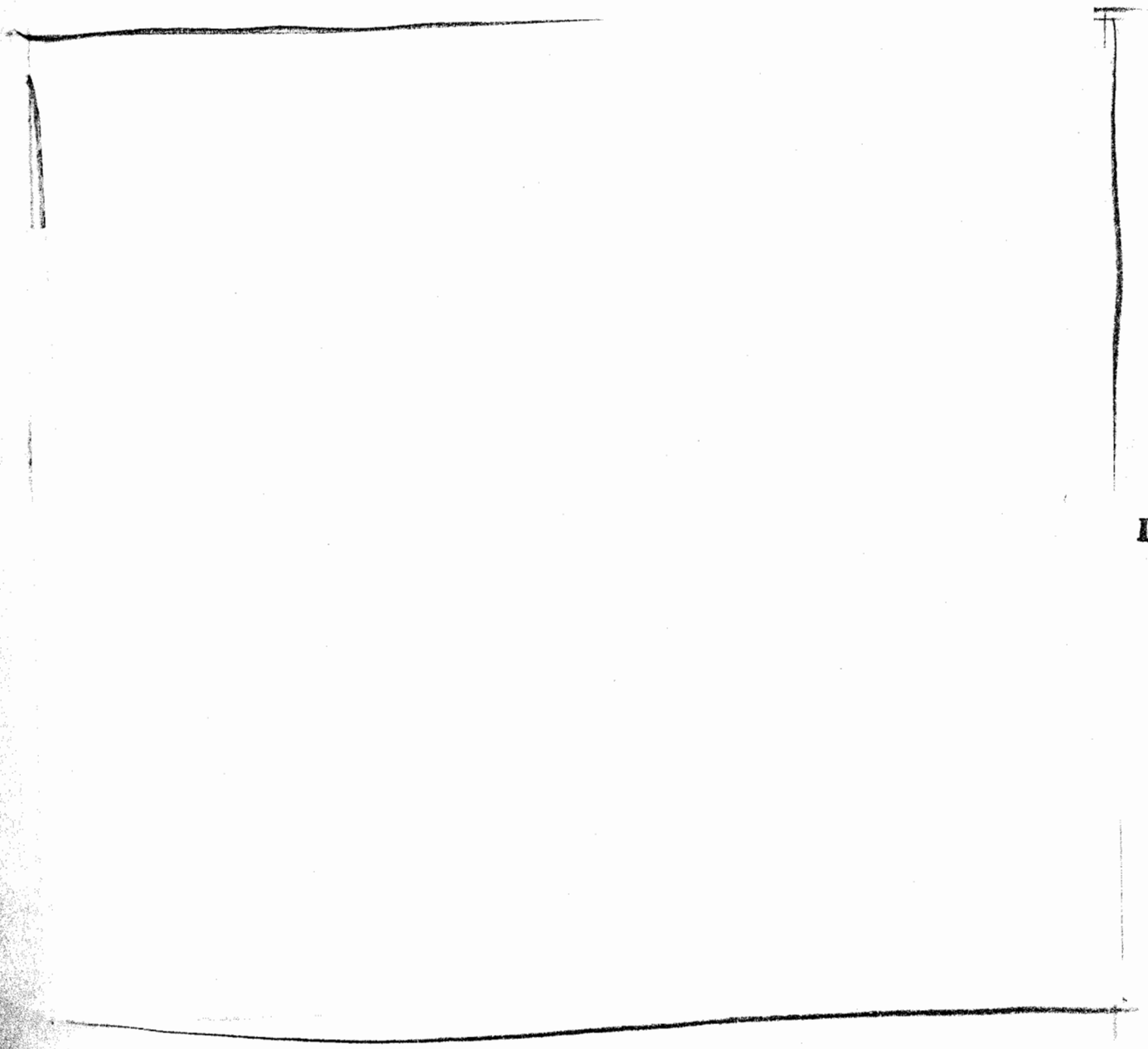

DOE
b(3)

Figure 30: Vertical velocity histories at several points down axis.

6 Comparisons with Other Calculations

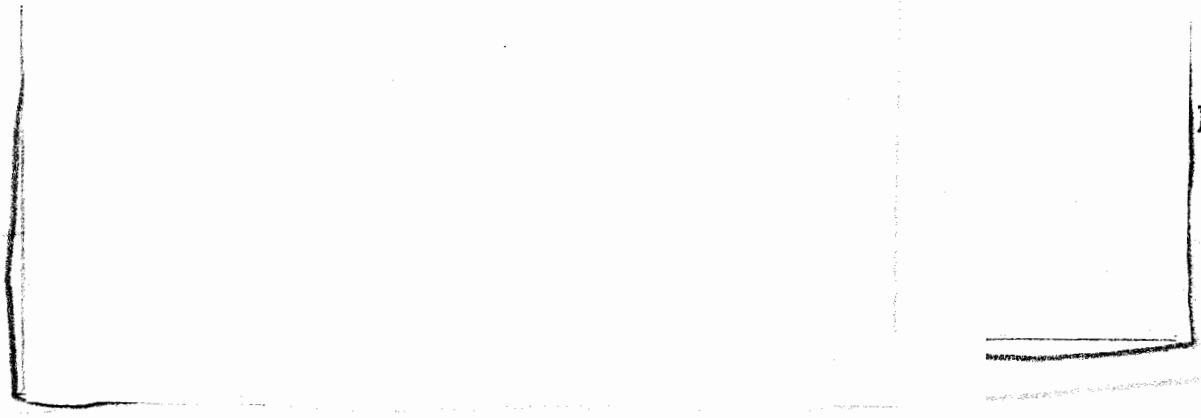

DOE
b(3)

One measure of the relative effectiveness of ground shock produced by different heights and depths of burst is the depth and range obtained by effects that may be

DOE
b(3)
1.5(e)
b(3)

These figures of parameter attenuation with depth include the attenuation curve for a fully contained burst[13] (infinite depth of burst) in the same geology. This allows comparison with the case for which no surface effects are present and, in general, is the

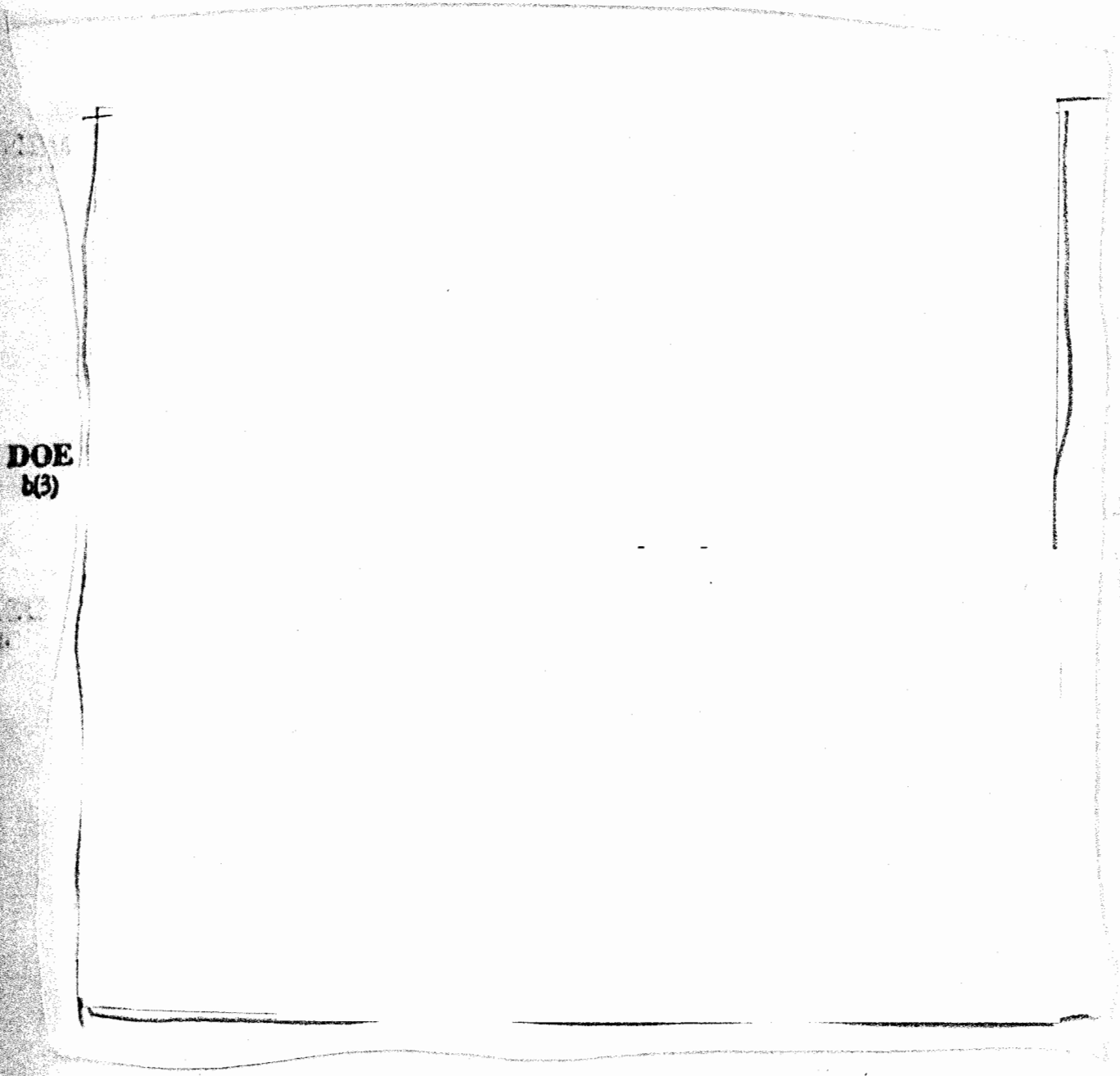

Figure 31: Peak vertical stress contours for several heights and depths of burst.

Figure 32: Peak horizontal stress contours for several heights and depths of burst.

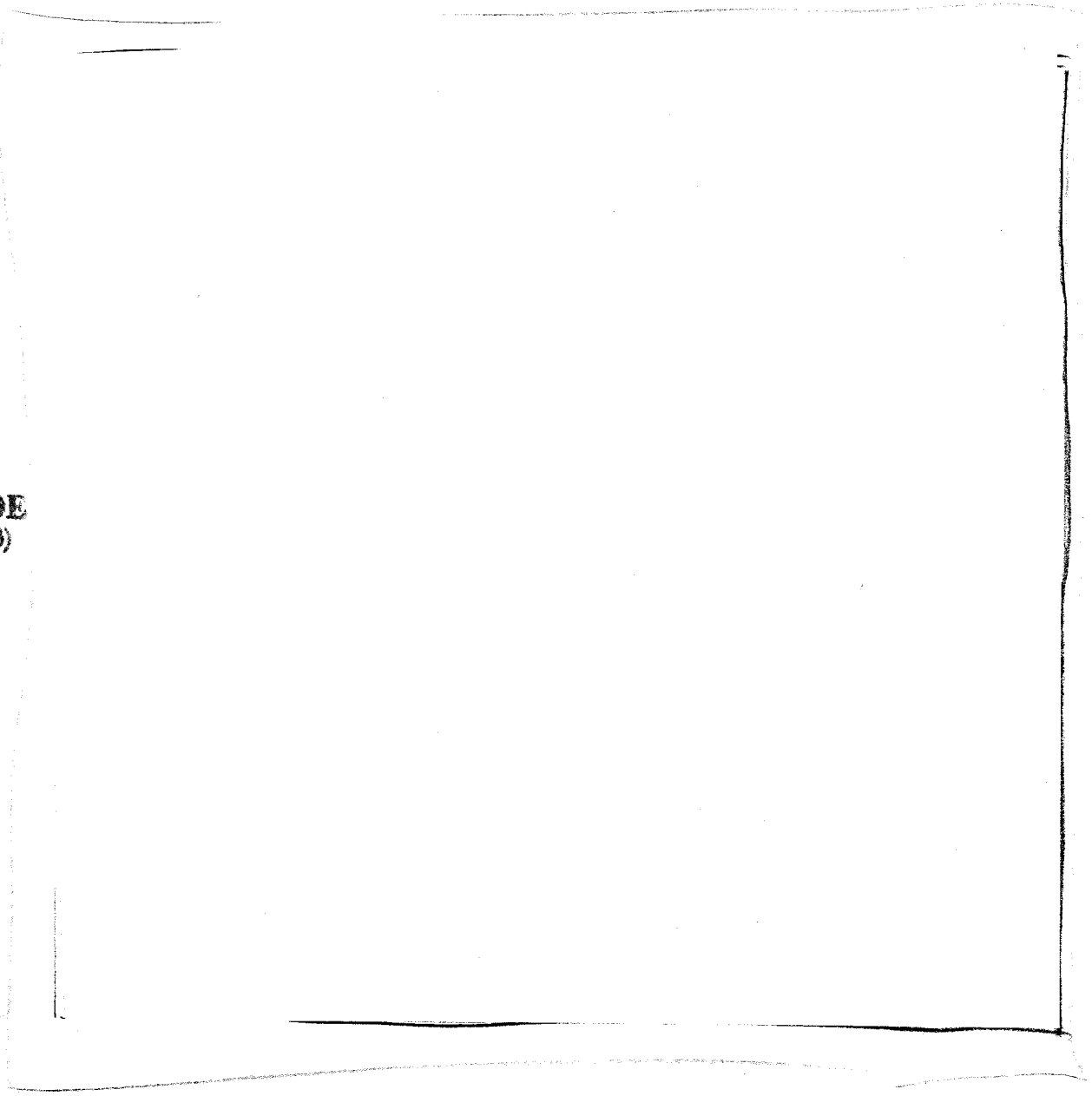

DOE
b(3)

Figure 32: Peak horizontal stress contours for several heights and depths of burst.

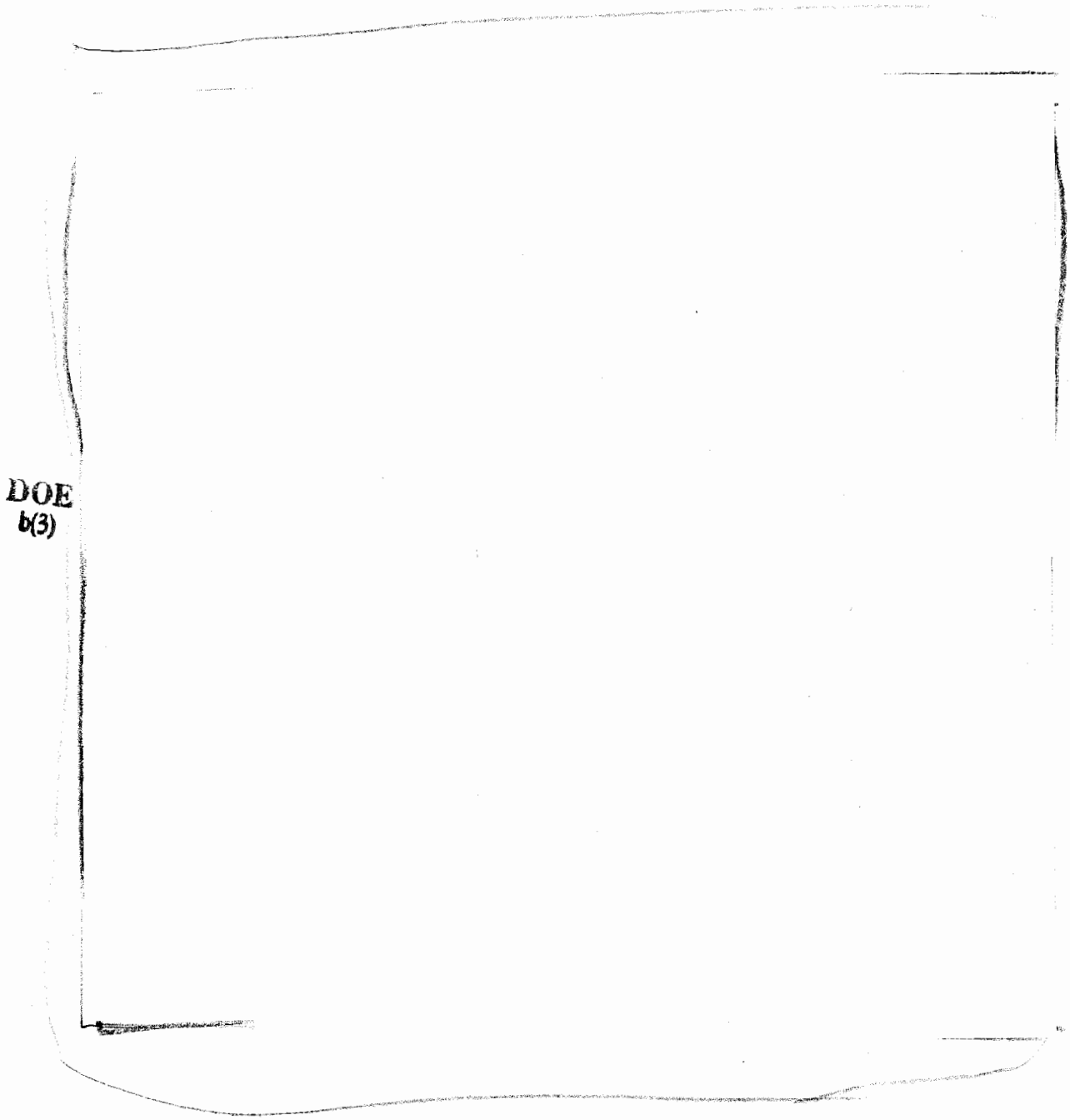

Figure 34: Peak horizontal velocity contours for several heights and depths of burst.

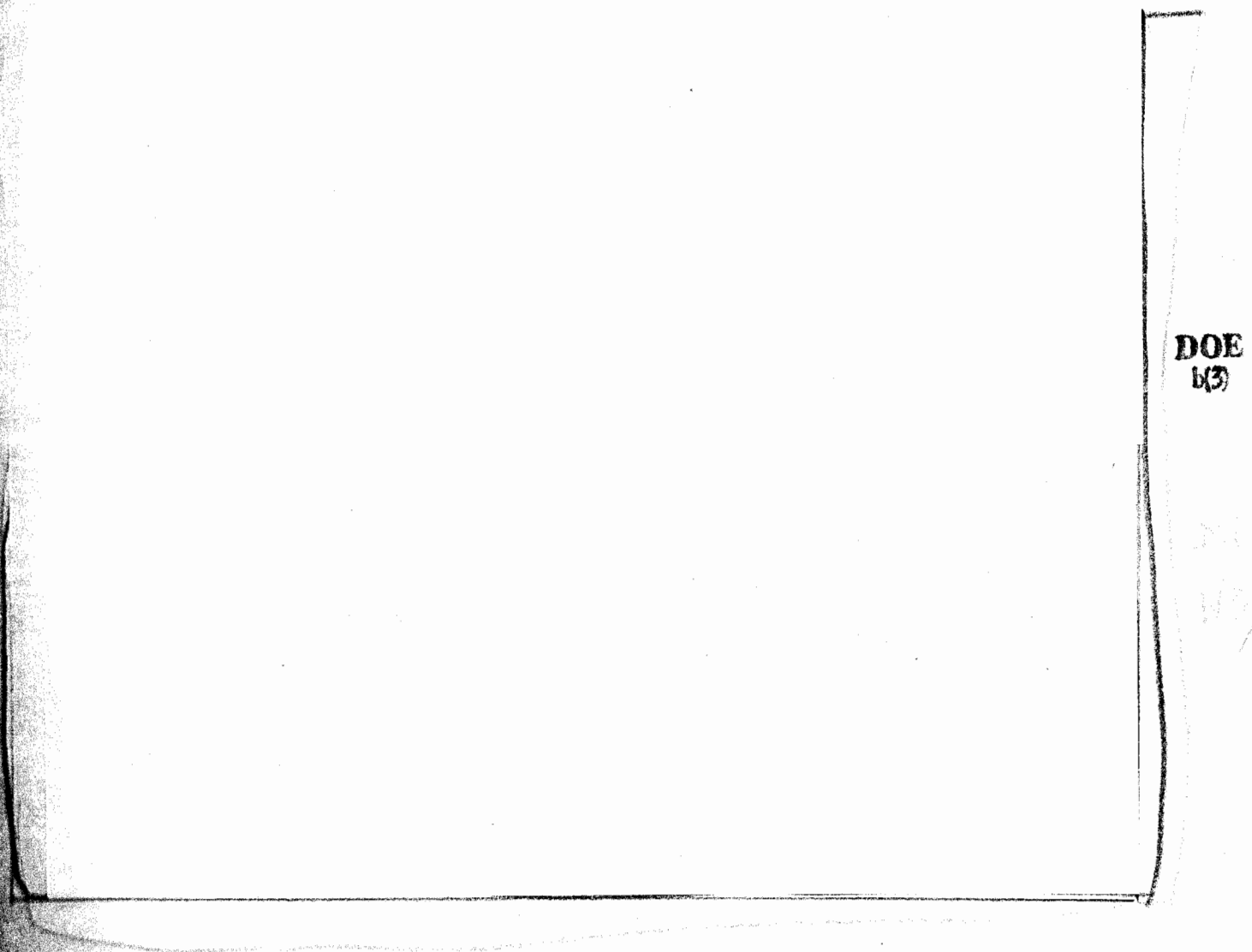

Figure 35: Peak vertical stress attenuation for several heights and depths of burst.

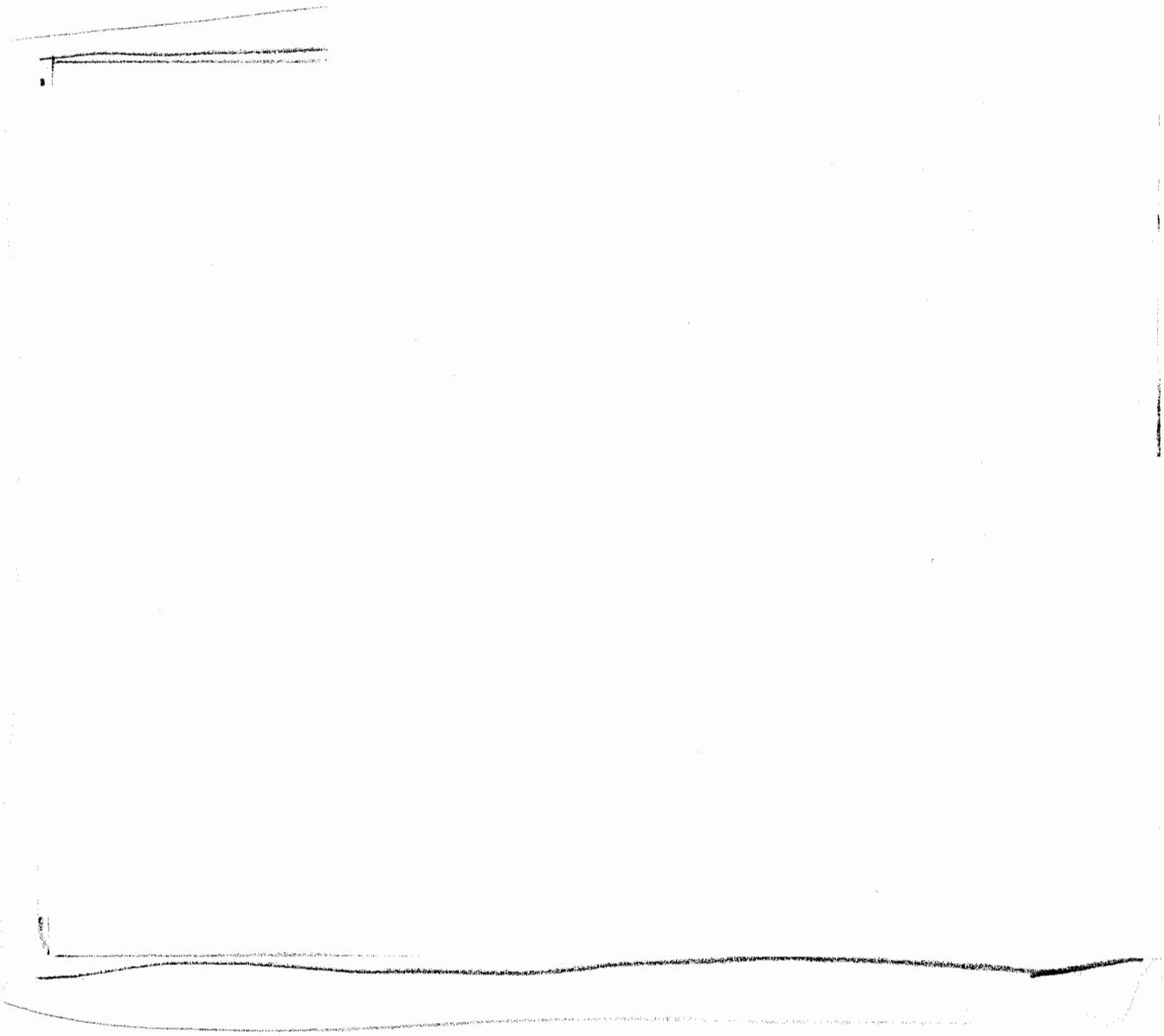

DOE
b(3)

Figure 36: Low end vertical stress attenuations curves for several burst conditions.

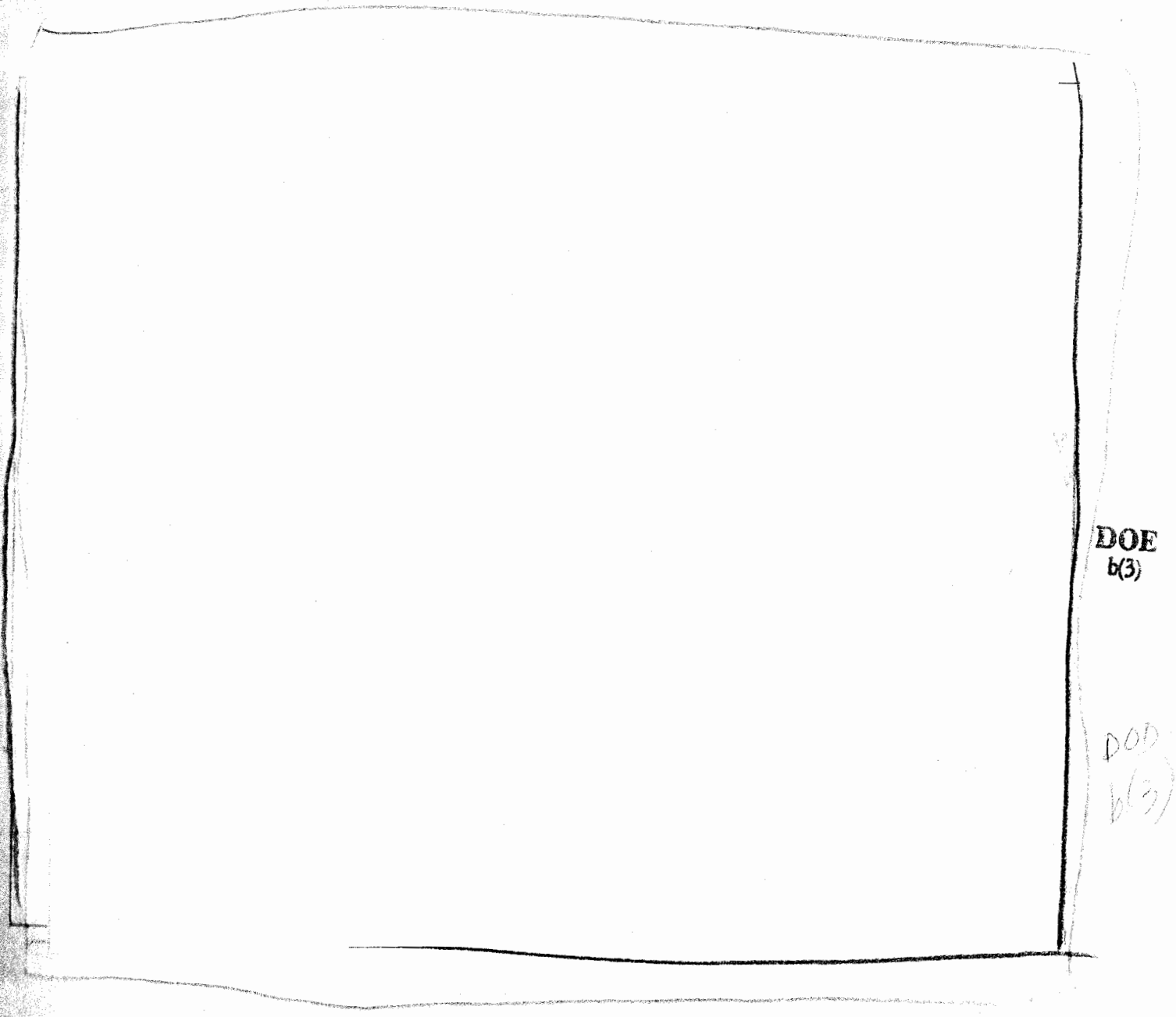

Figure 37: Vertical velocity attenuation for several heights and depths of burst.

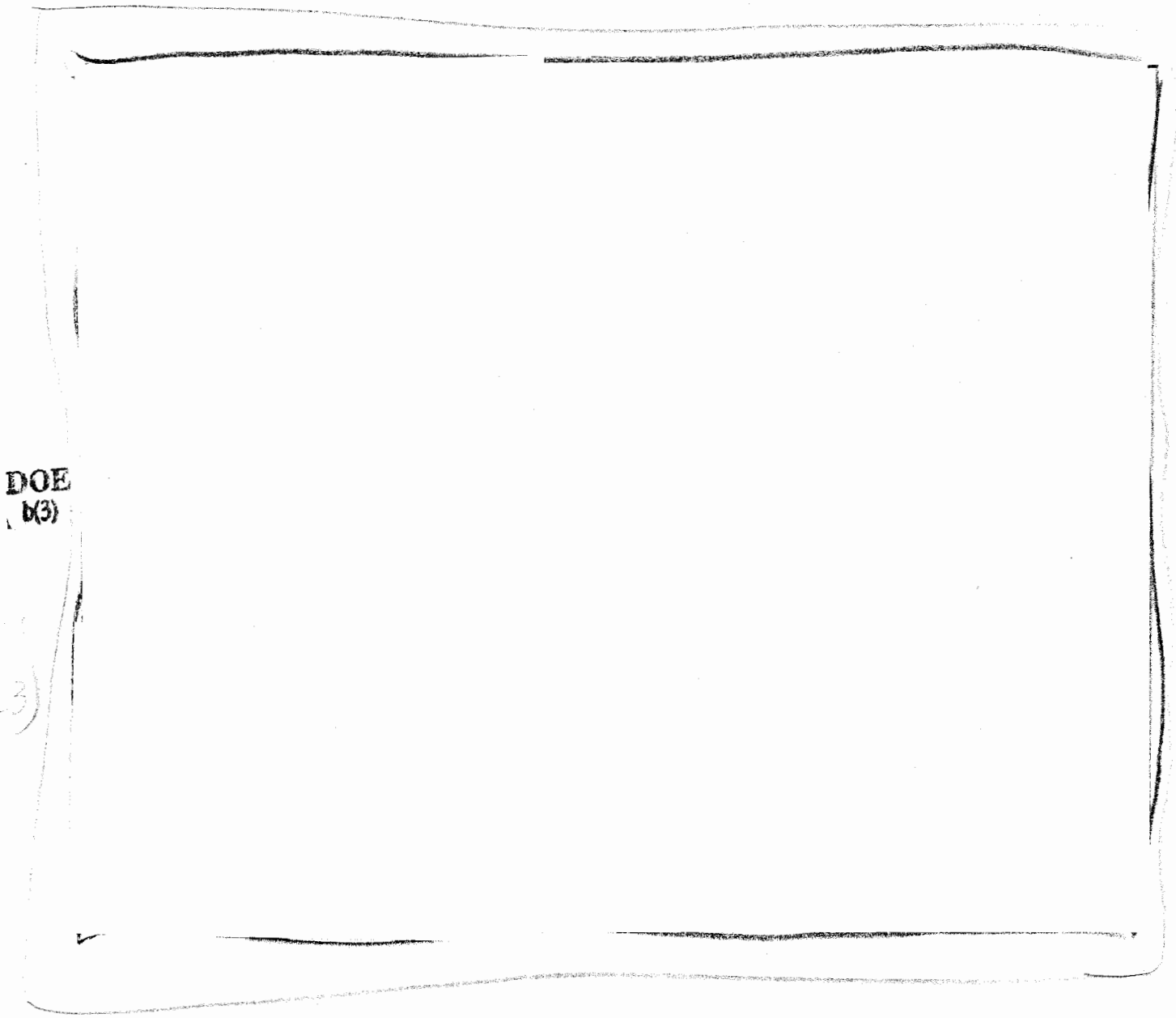

Figure 38: Low end velocity attenuation curves for several burst conditions.

case we prefer to use as a reference in making comparisons.

DOE
b(3)

Figure 39: Comparison of stress attenuation curves for the present calculation and the ICE calculation by S-Cubed.

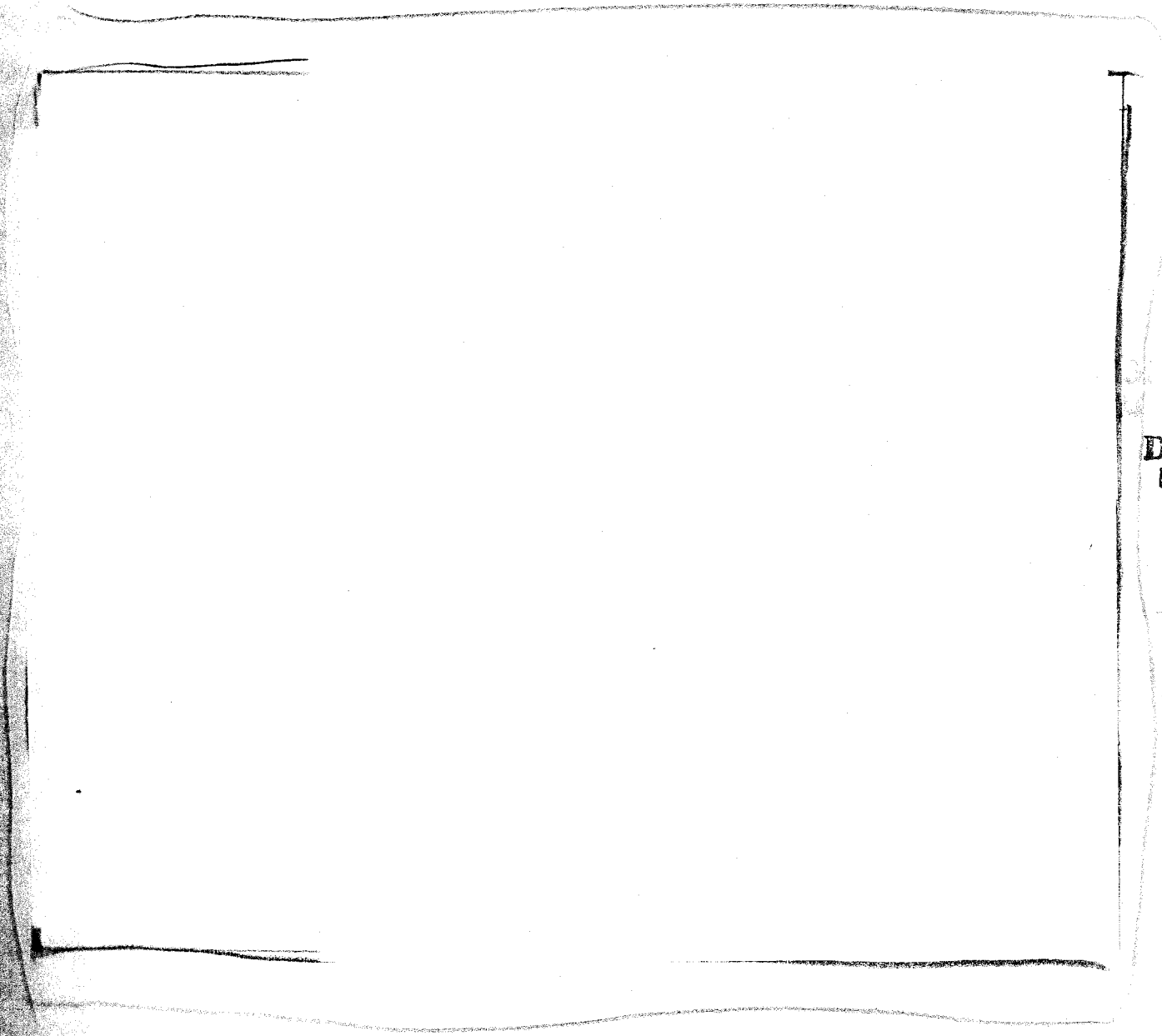

Figure 40: Comparison of velocity attenuation curves for present calculation and ICE calculation, by S-Cubed.

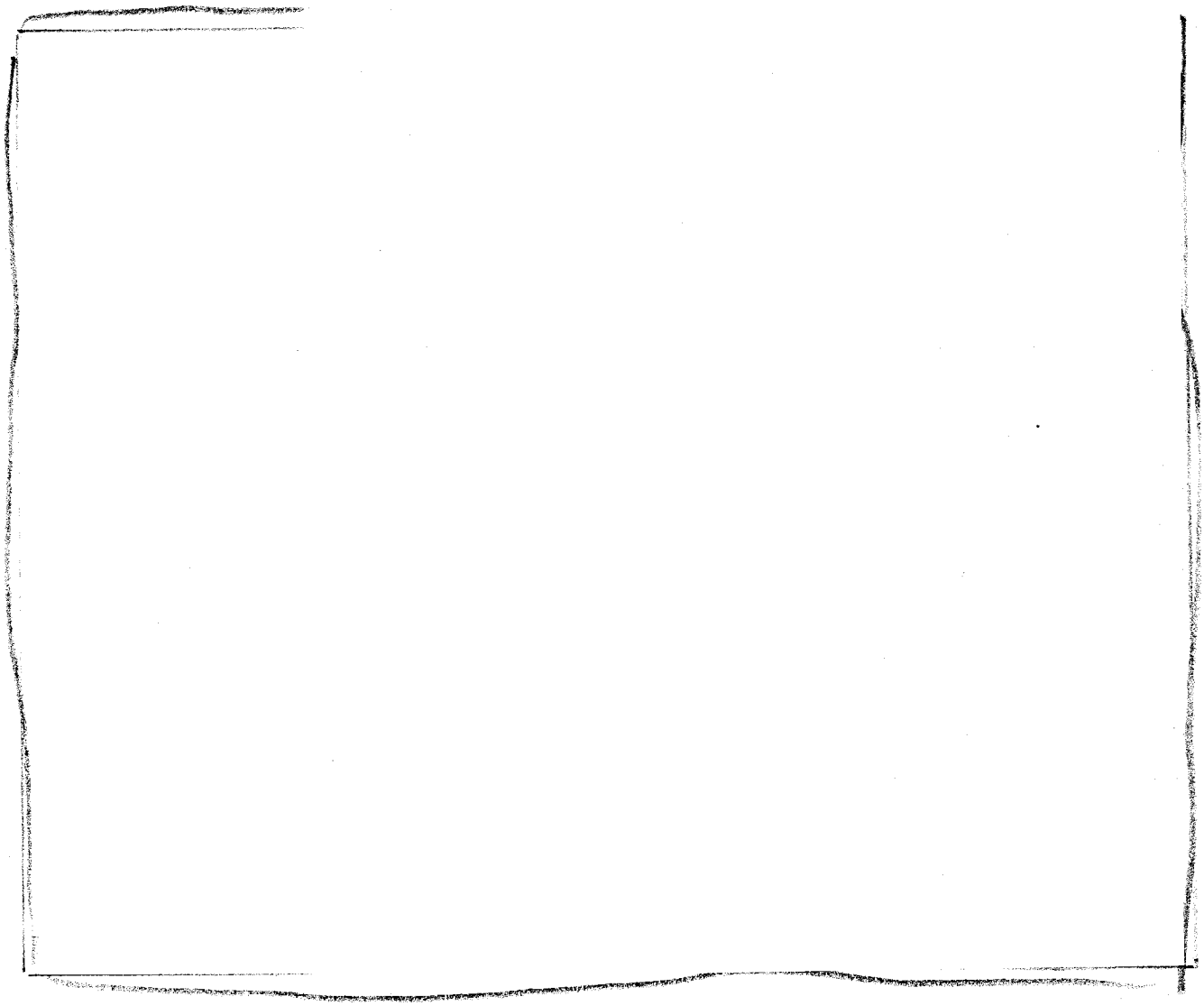

Figure 41: Downward directed kinetic energy vs. time for the present calculation and the S-Cubed ICE calculation.

DOE
b(3)

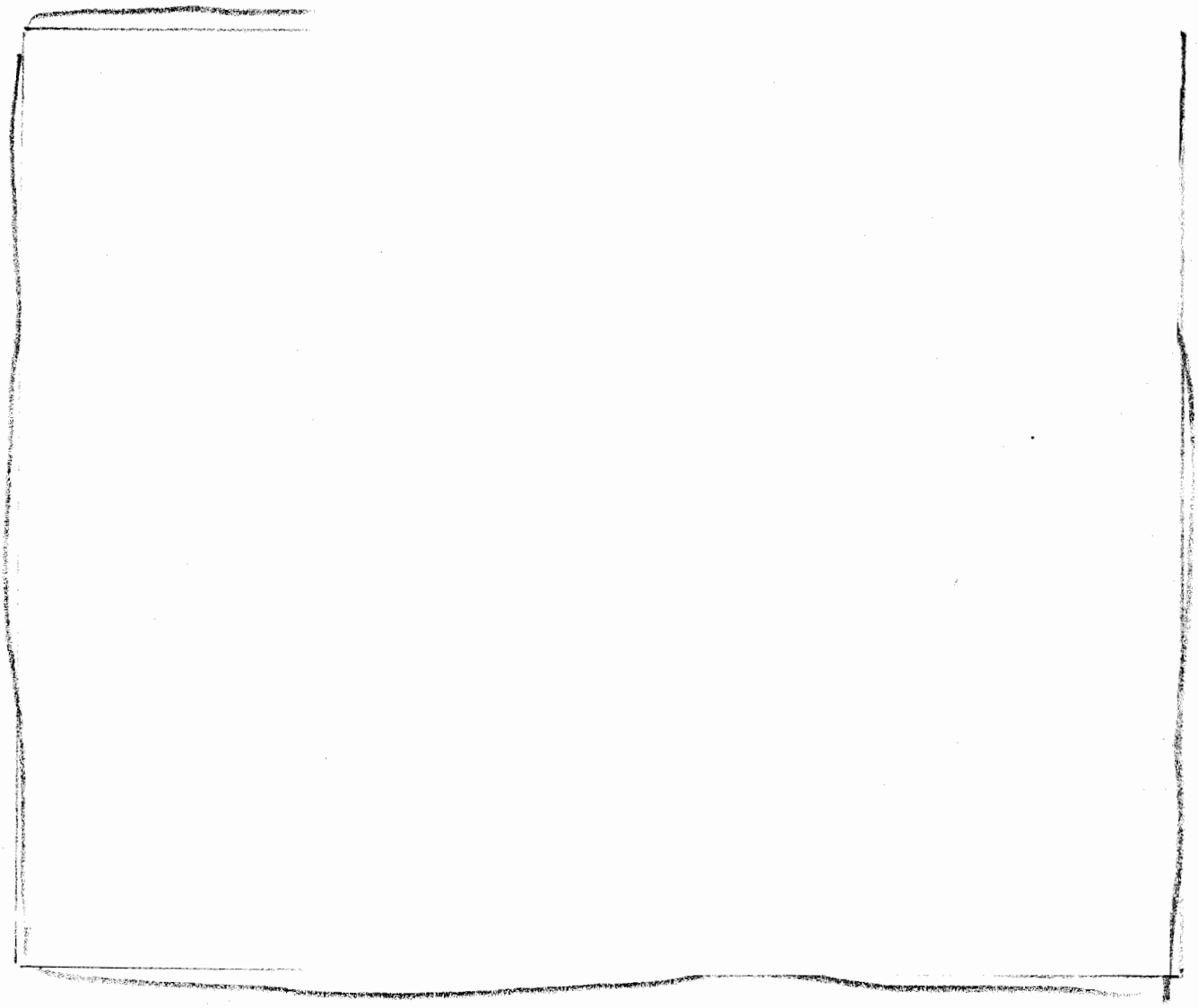

Figure 41: Downward directed kinetic energy vs. time for the present calculation and the S-Cubed ICE calculation.

7 Energy Coupling: Discussion and Comparisons

In comparing weapon effects calculations, there is frequently a need to reduce the comparison to a simple, single parameter that can be used as a figure of merit, spanning a wide variety of possible conditions. One such parameter is that expressed by the frequently used concept of "equivalent yield"[15], by which is usually meant the yield at which a chosen reference explosion and environment produces a result that is, in some sense, the same as that for the subject explosion and environment. Obviously, such a simple concept for comparisons will not be satisfactory for every need, but its utility for some purposes makes it quite compelling. Associated with this concept is that of the "yield factor", which can be defined as the ratio of two equivalent yields. We consider here some of the possible yield factors obtainable from the series of calculations recently completed at Sandia National Laboratories, to quantify the effect of height or depth of burst on ground shock. In doing so, we shall utilize the well known scaling rules[16] for explosion effects in which distance and time are scaled by the cube root of the input energy, and other parameters are scaled according to their units, taking energy, time, and length units as fundamental.

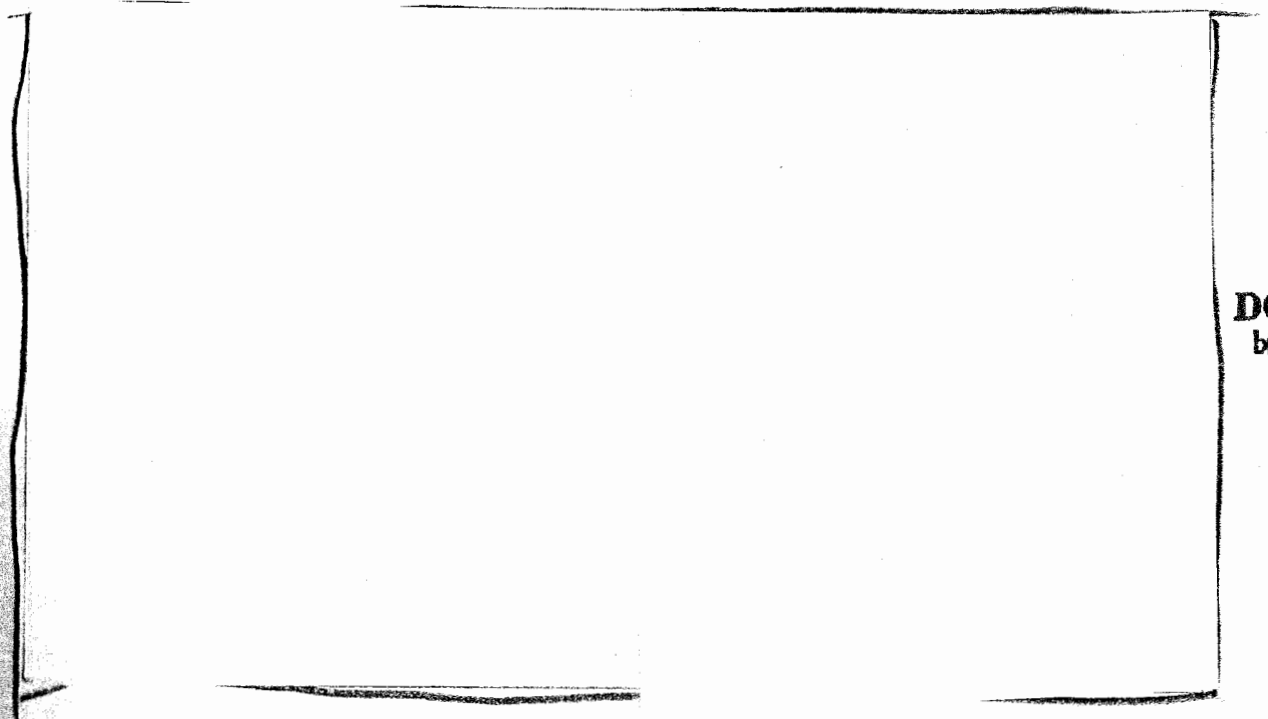

DOE
b(3)

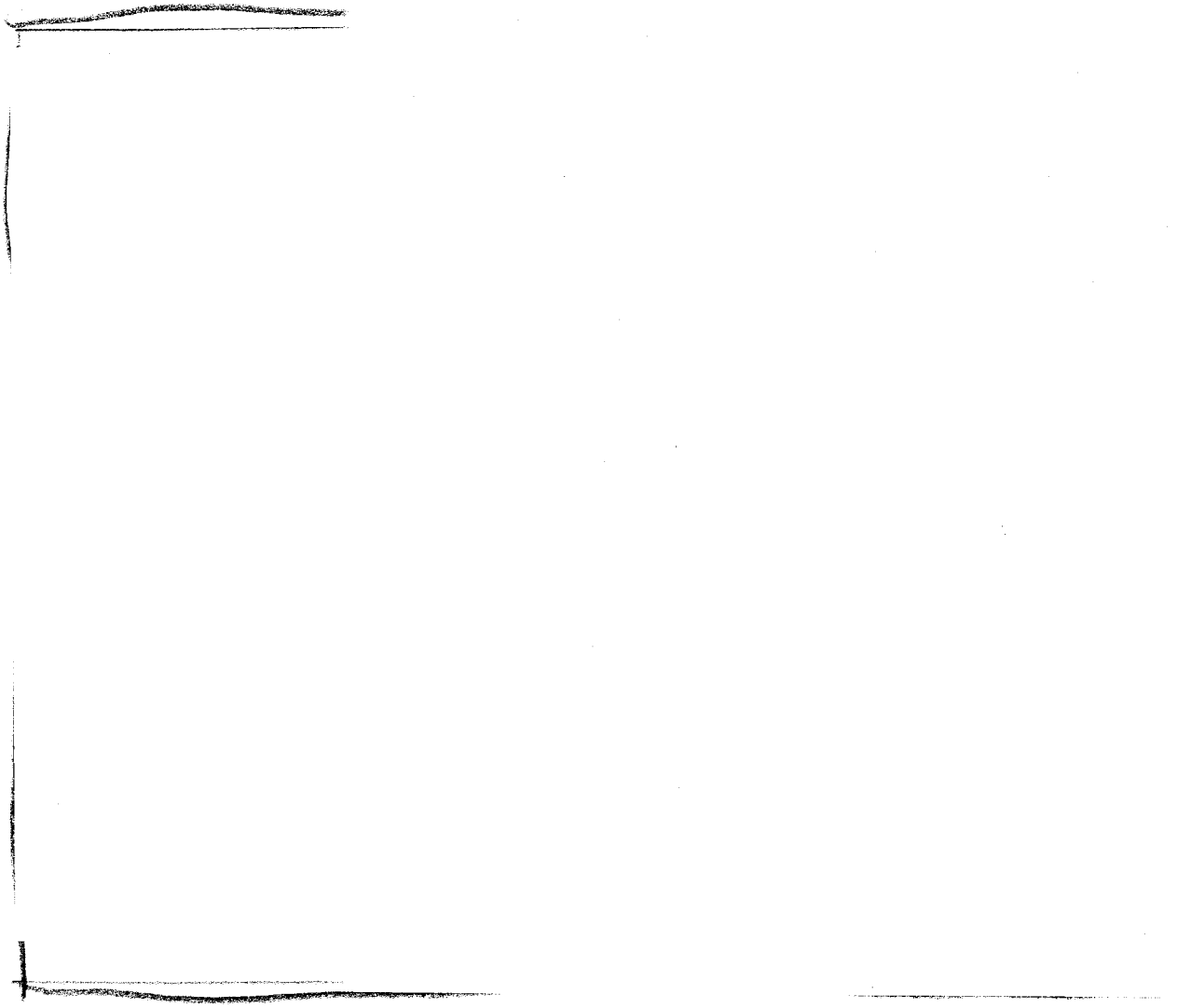

Figure 42: Scaled curves of contact burst comparing with shallow buried burst. Here different "effective yield" factors have been used.

We suggest that this yield factor provides a more meaningful measure of the energy effectively coupled to the ground than does a yield factor based on distances to a particular stress, or other effect.

In Figures 43 and 44, we have constructed curves of yield factor as functions of height/depth of burst from the present series of calculations using the techniques mentioned.

DOE
b(3)

Our examination of the present calculations suggests that the two effects just discussed are associated with two different aspects of the expansion of the ground resulting from the proximity of the burst to the surface. These aspects are: (1) the early time expansion and ejection of radiatively heated ground from the prompt coupling region

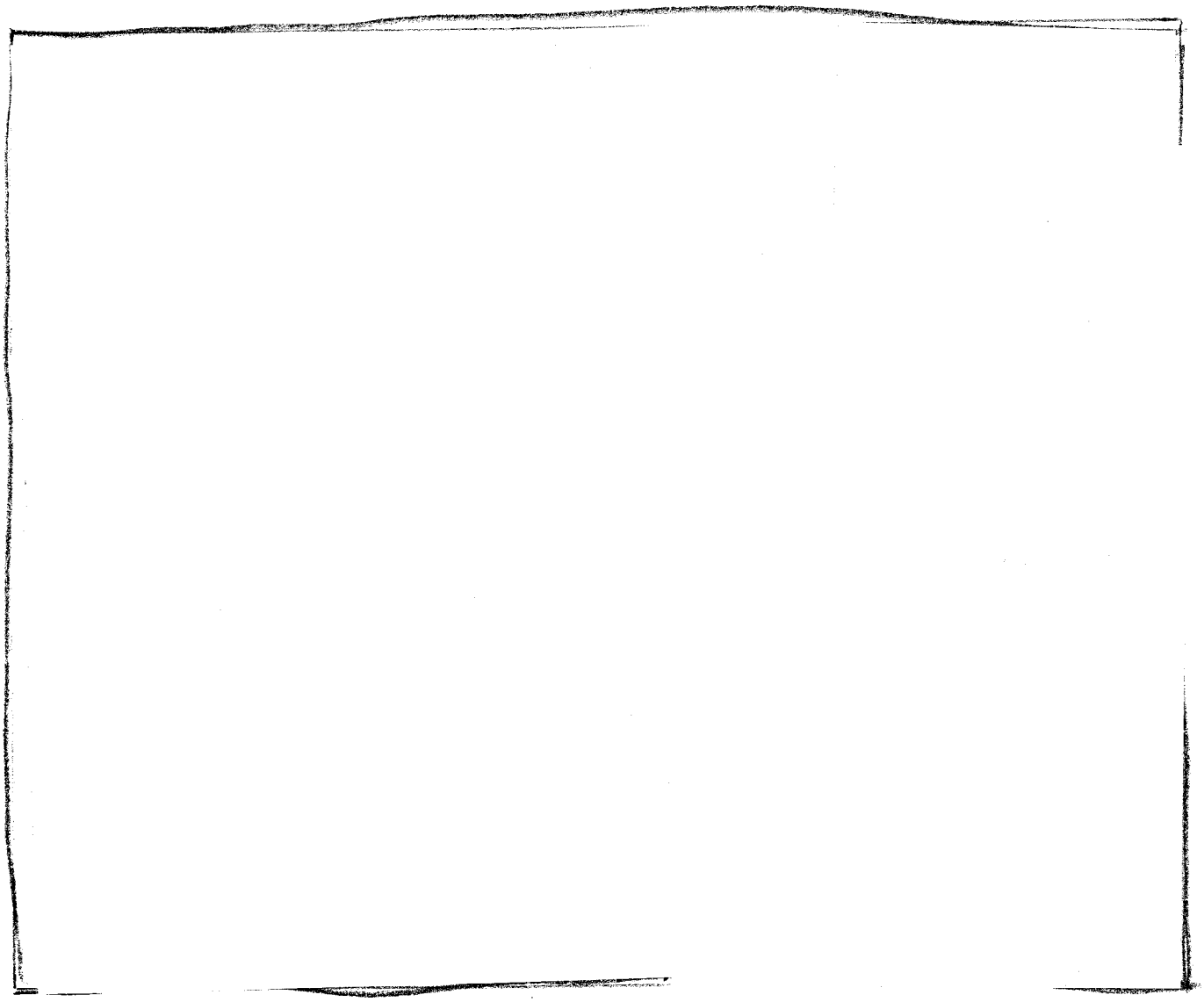

Figure 43: Yield factors as functions of height and depth of burst, using the contact burst as reference.

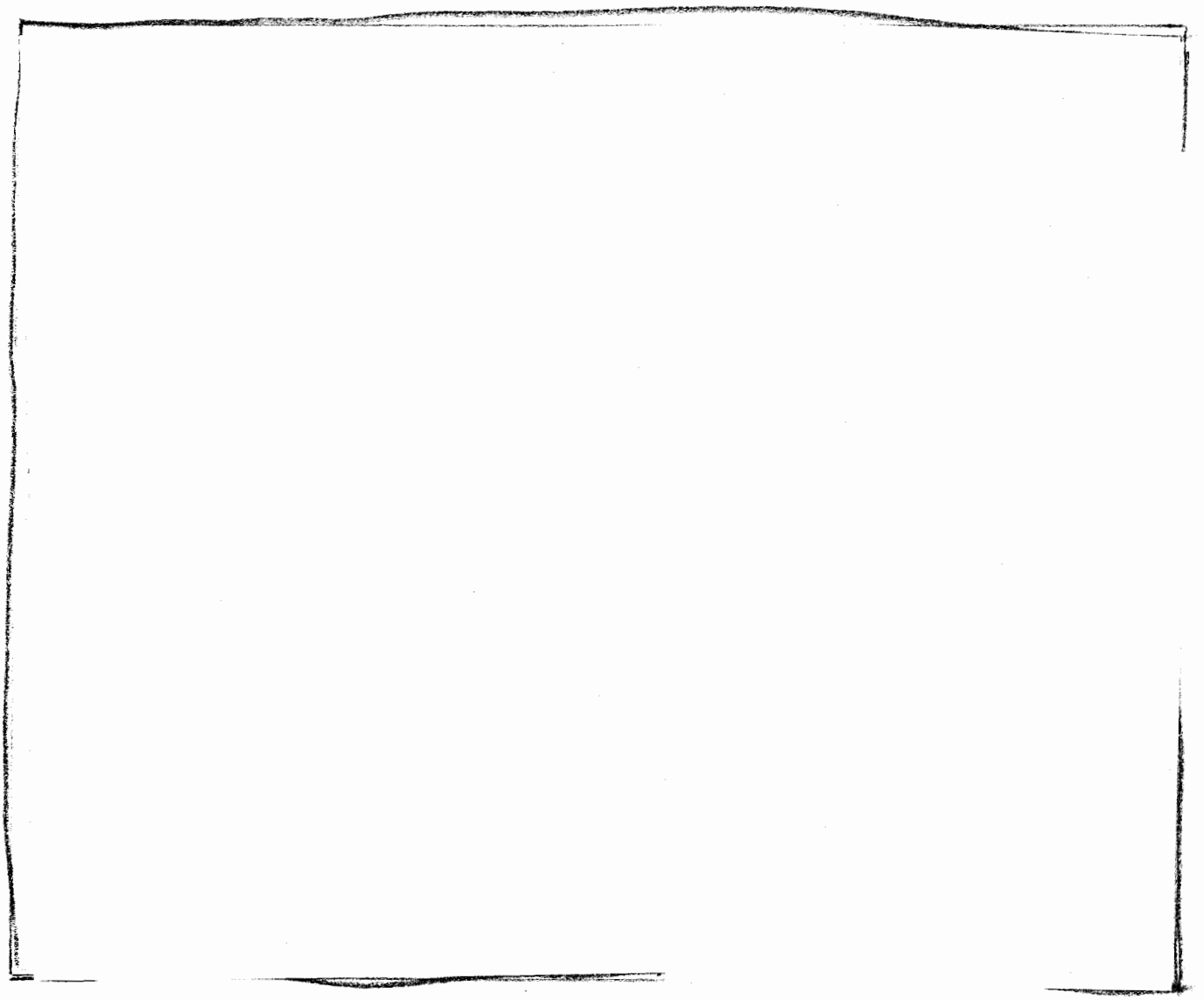

Figure 43: Yield factors as functions of height and depth of burst, using the contact burst as reference.

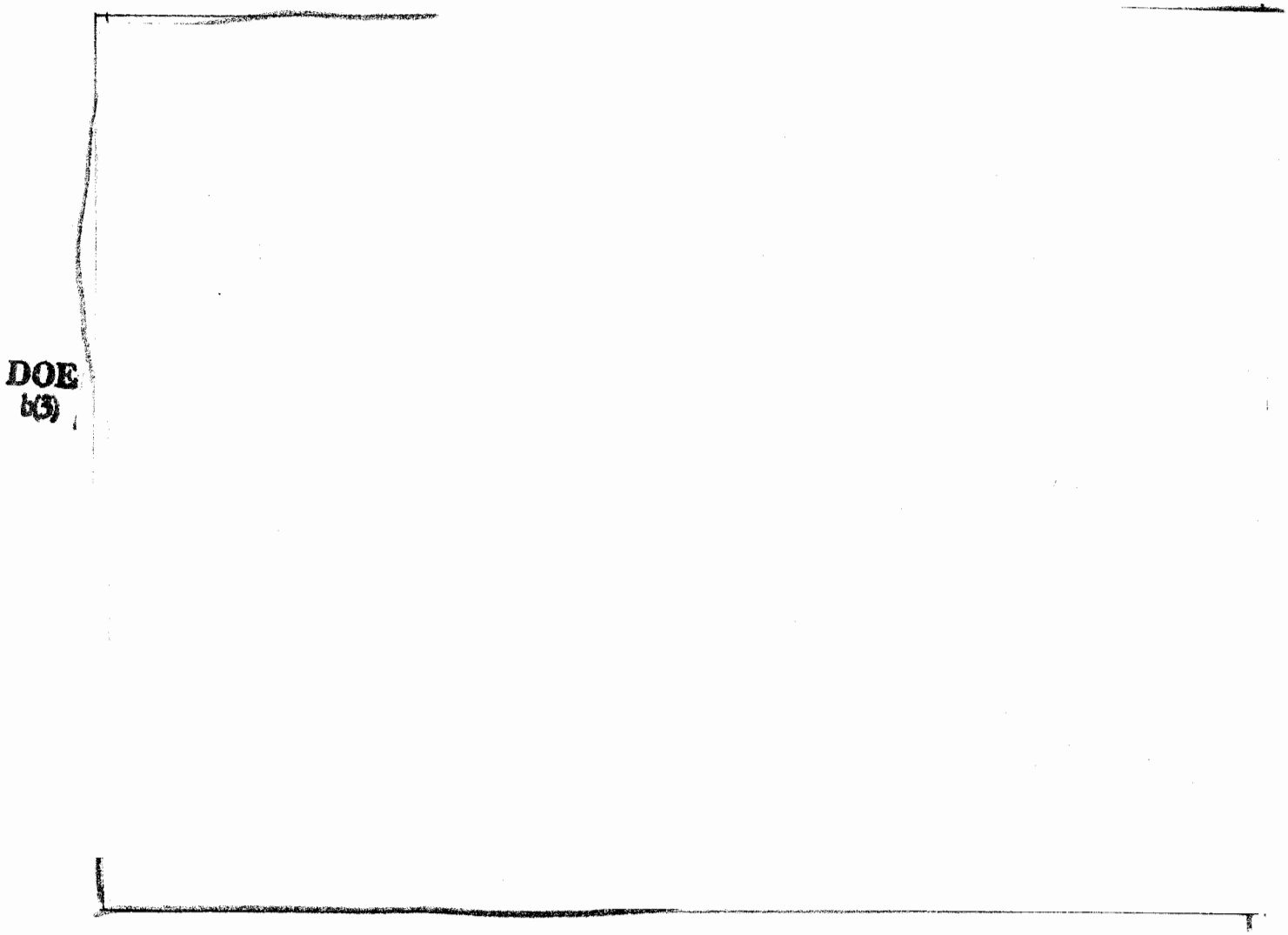

Figure 45: Scaled shallow burst compared with the fully contained burst.

Figure 45: Scaled shallow burst compared with the fully contained burst.

of earth, (this results in an early reduction of cavity pressure), and (2) a low pressure boundary condition on the ground shock imposed at the air/ground interface after the shock emerges from the radiatively heated region and begins to propagate in unheated material.

DOE b(3)

The above-surface bursts are scaled to compare with the deeply buried case in Figure 47.

DOE b(3)

After the airblast causes a rise above the fully contained curve (in a scaled sense) the phenomenon of rapid attenuation from surface relief is again seen.

In Figure 48, the pressure distribution with depth and range for the shallow buried burst is shown in three dimensional relief, at about the time of arrival of the expansion wave from the surface, as deduced from the attenuation curves (40 ms, here). The expansion wave is, of course, spread out over a large distance and is therefore difficult to identify in the figure. The airblast wave, and the elastic precursor to the main pulse, however, are readily discerned (the low level waves preceeding the main stress pulse).

The preceeding discussion of yield factor and effectively coupled energy for ground shock stress attenuation, and the earlier comparison of the airblast with the 250 kT surface burst reference curve from Brode[12], allows the interesting observation that these effects suggest the late time partitioning of the energy of the shallow burst nearly equally between the airblast and ground shock.

DOE b(3)

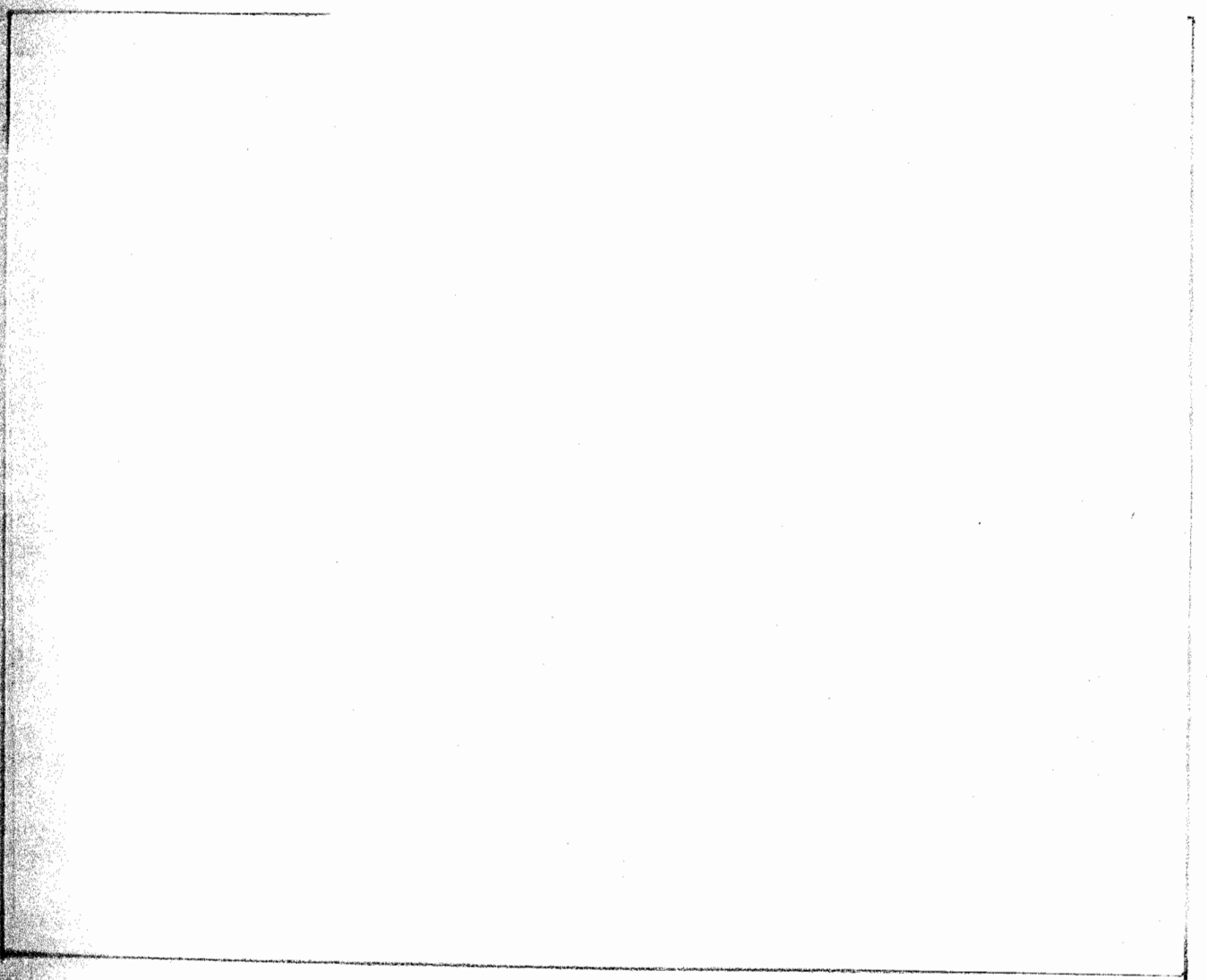

Figure 47: Above surface bursts scaled to compare with fully contained burst.

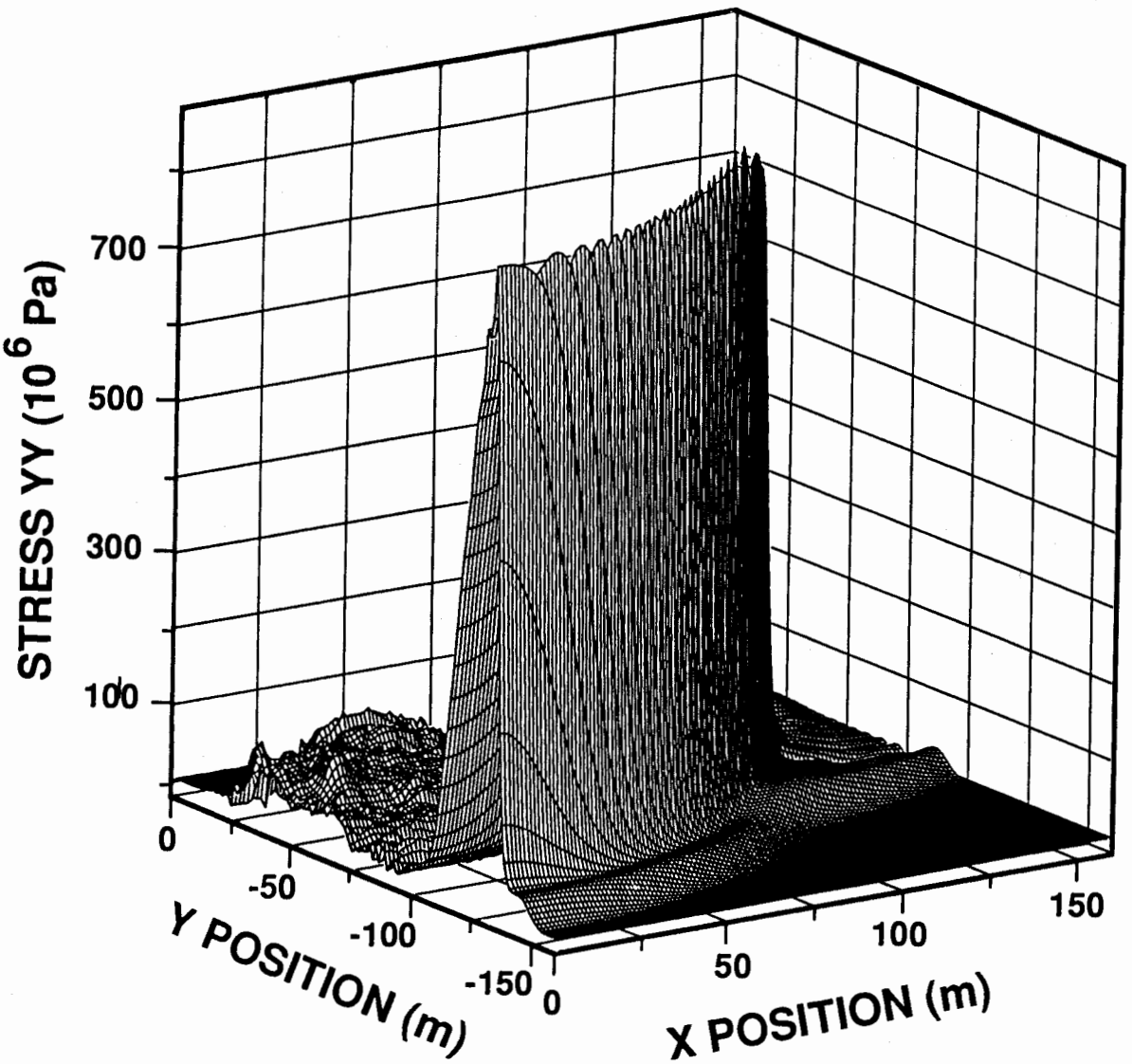

Figure 48: Pressure profile of the shallow burst calculation at 40 ms. The pulse representing the elastic precursor is seen slightly below the main shock wave. Slightly to the right, the airblast wave can be seen.

DOE
b(3)

8 Summary and Conclusions

The calculation of a shallow buried nuclear burst described here, combined with calculations presented elsewhere[1,2], completes a study of the effect of height and depth of burst on ground shock effectiveness against deeply buried and/or hardened targets.

DOE
b(3)

Several measures of energy coupling effectiveness with height and depth of burst have been discussed, here and elsewhere.

DOE
b(1)

DOE
b(1)

REFERENCES

1. W. R. Davey and P. Yarrington, *"Proximity and Contact Fuze Calculations for the W88/Mk5 (U),"* SAND88-0569, Sandia National Laboratories, Albuquerque, N. M., (in preparation) (SRD).

2. Paul Yarrington, *"Ground Shock from Earth Penetrator Weapons,"* SAND88-1497, Sandia National Laboratories, Albuquerque, NM, 11/88.

3. M. W. McKay, M. B. Gross, M. R. Warburton, and W. S. Vance, *Weapon Systems to Counter Deeply Buried Targets (CDBT) (U),"* SAIC LJ/DC No. 86:1344.1,Science Applications International Corp., La Jolla, CA, 11/27/87.

4. K. D. Pyatt, *"Enhanced Coupling,"* SSS-R-86-7747, S-CUBE report, presented to Silo Hardness Panel, at Aerospace Corporation, Los Angeles, CA, 2/4/86.

5. G. B. Zimmerman, *"The LASNEX Computer Code (U),"* UCID-19202, Lawrence Livermore National Laboratory, Livermore, CA, 9/23/81 (SRD).

6. S. L. Thompson, *"CSQII - An Eulerian Finite Difference Program for Two-Dimensional Materials Response - Part I. Materials Section,"* SAND77-1339, Sandia National Laboratories, Albuquerque, NM, January 1979 (reprinted 6/85).

7. A. V. Farnsworth, Jr, *"A Nuclear Device Model for Ground Shock Studies (U),"* SAND88-0310, Sandia National Laboratories, Albuquerque, NM, 6/88.

8. R. C. Bass and G. E. Larson, *"Shock Propagation in Several Geologic Materials of Interest in Hydrodynamic Yield Determination,"* SAND77-0402, Sandia National Laboratories, Albuquerque, NM, 3/77.

9. Paul Hooper and Richard Howell, *"Interim Earth-Penetrator Weapon Test Series (U),"* SAND88-2268, Sandia National Laboratories, Albuquerque, NM, 1/89.

10. A. V. Farnsworth, Jr. *"LASTRAN: A System for Coupling the LASNEX and CSQ Hydrocodes,"* SAND86-0866, Sandia National Laboratories, Albuquerque, NM, 7/86.

11. W. R. Davey, S. L. Thompson, T. K. Bergstresser, and A. J. Chabai, *"Nuclear Explosion Height-of-Burst Study I, 0.17 m and .77 m Cases (U),"* SAND78-0546, Sandia National Laboratories, Albuquerque, NM, March 1978, (SRD); also, T. K. Bergstresser, A. J. Chabai, W. R. Davey, *"Nuclear Explosion Height-of-Burst Study (U),"* SAND80-2358, Sandia National Laboratories, Albuquerque, NM, 3/83, (SRD).

12. H. L. Brode and S. J. Speicher, *"Air Blast from Nuclear Bursts - Analytic Approximations (U),"* PSR Report 1419-1, Pacific-Sierra Research Corp., Los Angeles, CA, 10/84.

13. Memo, W. T. Brown to P. Yarrington, *"Spherically Symmetric Explosion in Tuff,"* Sandia National Laboratories, Albuquerque, NM, dated 8/11/87.

14. Steven Peyton, *"Coupling Predictions"*, SSS-R-87-8607, presented at DNA, meeting on Ground Shock Calculations for Strategic Applications, R & Associates, Marina del Rey, CA, 3/19/87.

15. R. E. Crawford, C. J. Higgins, and E. H. Bultmann, "The Air Force Manual for Design and Analysis of Hardened Structures," AFWL-TR-74-102, Air Force Weapons Laboratory, Kirtland Air Force Base, N. M., 10/74, p. 266.

16. Samuel Glasstone and Philip J. Dolan, *"The Effects of Nuclear Weapons, 3rd Ed."* U. S. Gov. Printing Office, Wash. D. C., 1977, p. 100.

APPENDIX 1. Sensitivities to Modeling Assumptions

In connection with the shallow burst study discussed in the text, a number of calculations were performed to test early time sensitivities to changes in the initial conditions assumed. The computing times for running LASNEX using the implicit Monte-Carlo radiation transport method were long ($\approx$ 50 - 100 cpu hours), so most of these sensitivity checks were performed using the much faster diffusion options, especially the three temperature single group diffusion model. The interest here was primarily in determining the effect of different assumptions on the prompt radiative energy loss to the atmosphere. In every case tested, the diffusion treatments of radiation in the ground and debris in the hole led to larger estimates of radiation energy loss than the IMC treatment gave, which does not seem surprising, when one considers the limits inherent in the diffusion treatment.

The parameters varied in these calculations were, primarily, (a) the radiation transport approximation employed, (b) the density and opacity of the debris filling the hole, (c) the diameter of the hole, (d) the depth of the hole, and various combinations of these that the writer deemed interesting. The goal of these calculations was to investigate radiative energy loss sensitivities, rather than to provide a systematic study of the effects of parameter variation; however, the work hopefully provides some modest insights in that direction.

DOE b(3) 5 5(1)

DOE
b(3)
b(1)
1.5(d): X2

DOE
b(3)

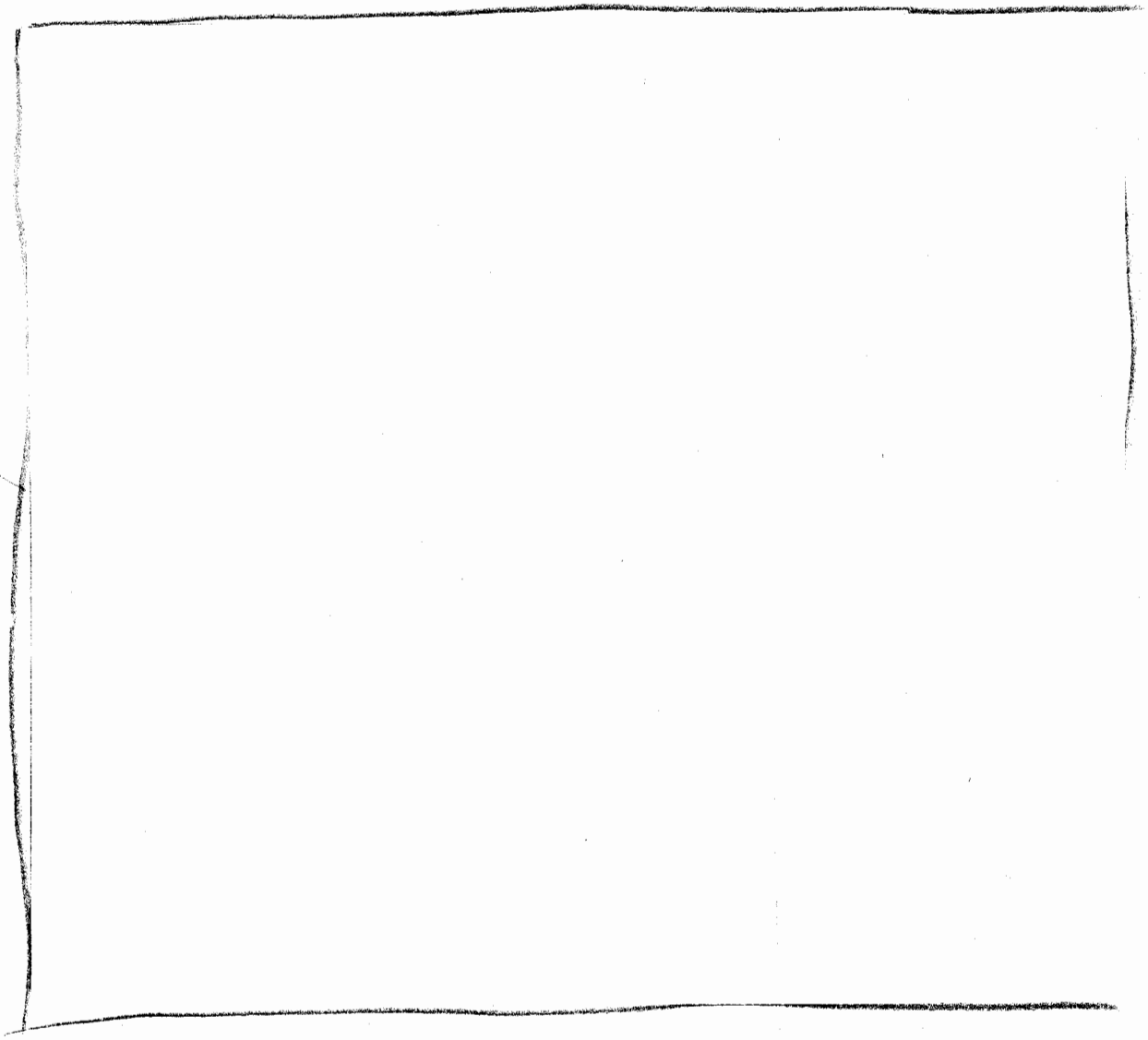

DOE
b(3)
+
+(1)

DOE
b(1)

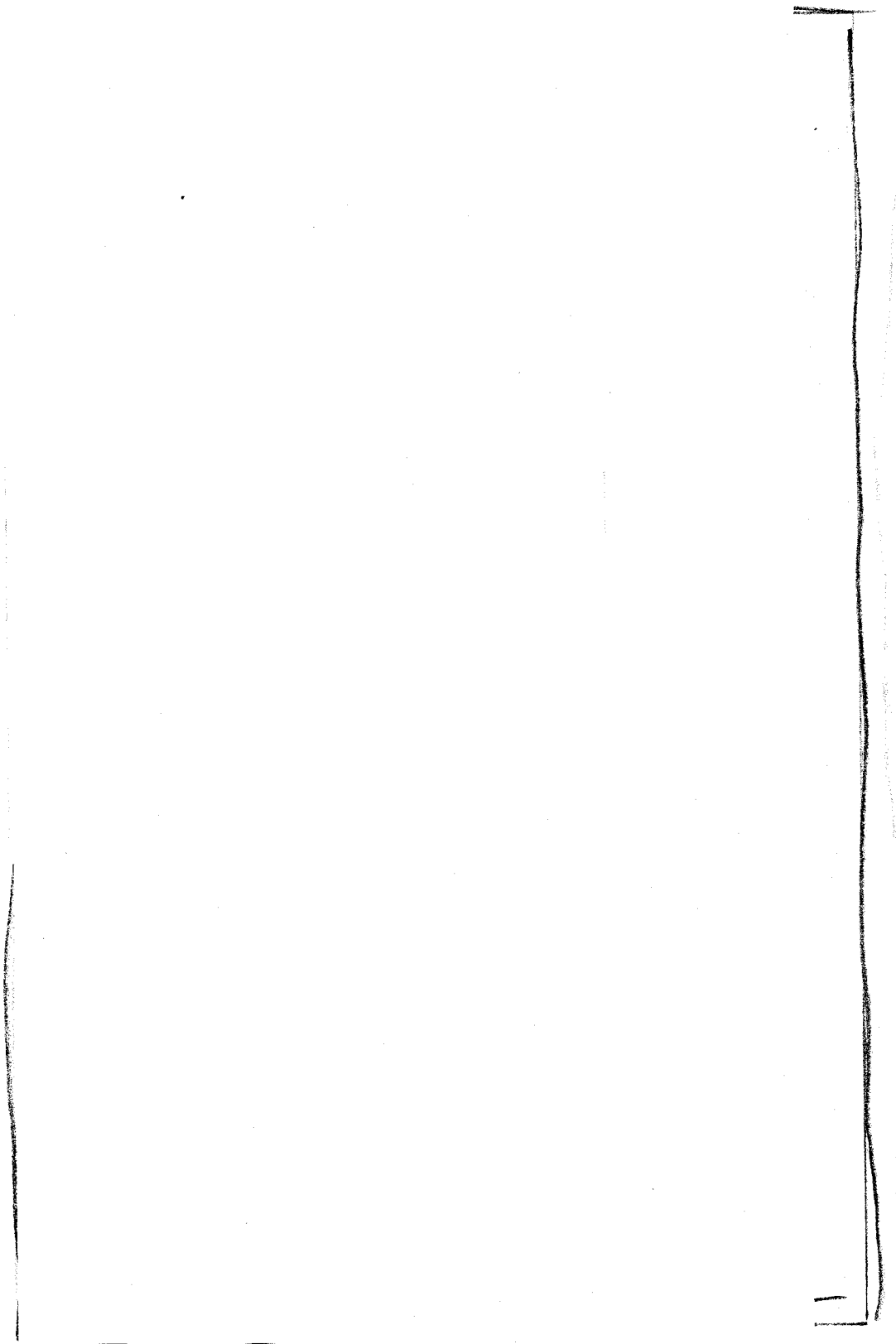

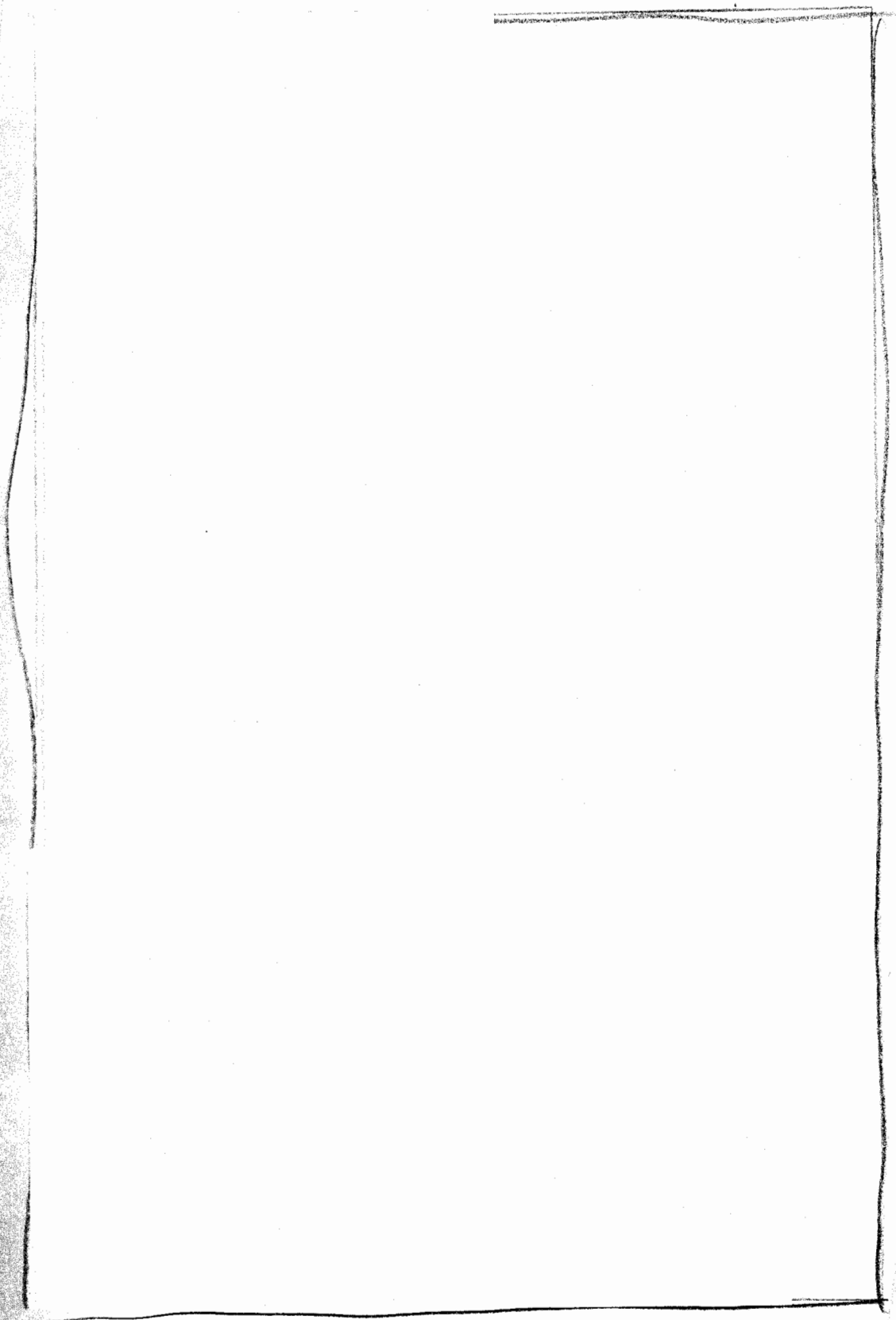

Doe
b(1)

DOE
b(3)

DoE
b(1)

DOE
b(1)

DOS
b(1)

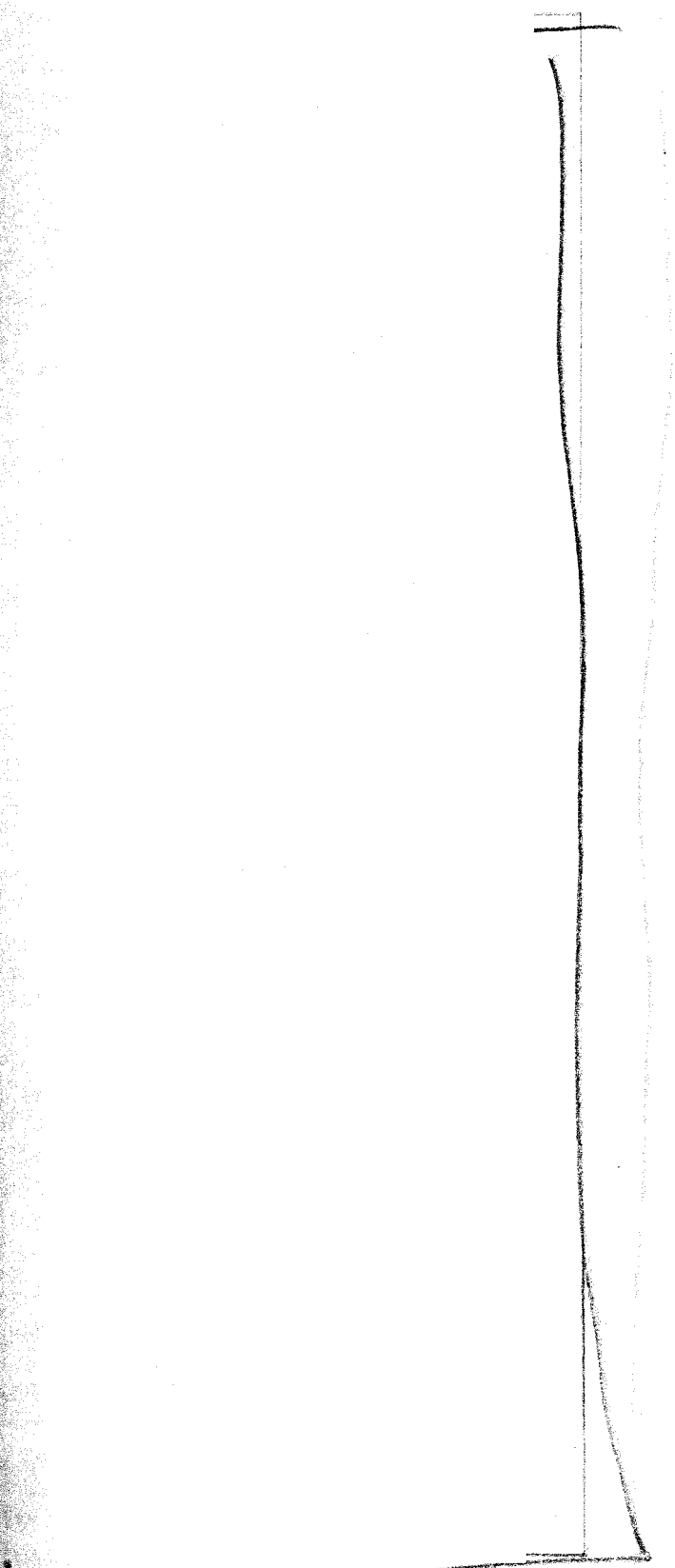

DOE
b(1)

DOE
b(1)

DOE
b(1)

DOE
b(1)

DOE
(C)

DOE
b(1)

DOE
b(1)

DOE
b(1)

DoE
b(1)

APPENDIX 3. Input to the CSQGEN and CSQ Codes

The CSQ calculation was performed in ten runs, each having two input sets, the first to the CSQGEN program, the second to CSQ. The following are the input for those runs. The versions of those programs were: CSQGEN version 3.0, dated 9 Nov. 1986, and CSQ version 3.0, dated 9 Nov. 1986. The modifications to CSQ used for this work are discussed in References 1 and 2.

Input for CSQGEN, run 1.

DoE
b(1)

```
*** Many more material insert cards from LASNEX output. ***
```

Input for CSQ, run 1.

DOE
b(1)

Input for CSQGEN, run 2.

DOE
b(1)

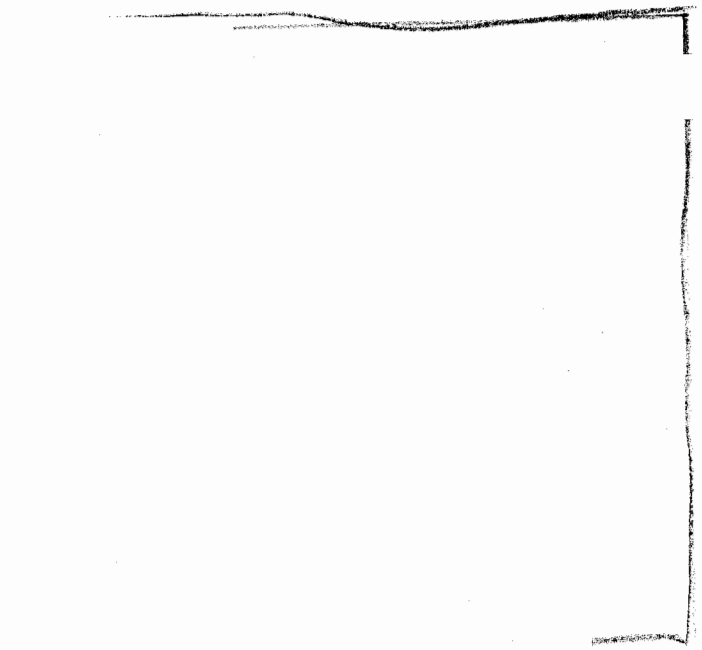

Input for CSQGEN, run 3.

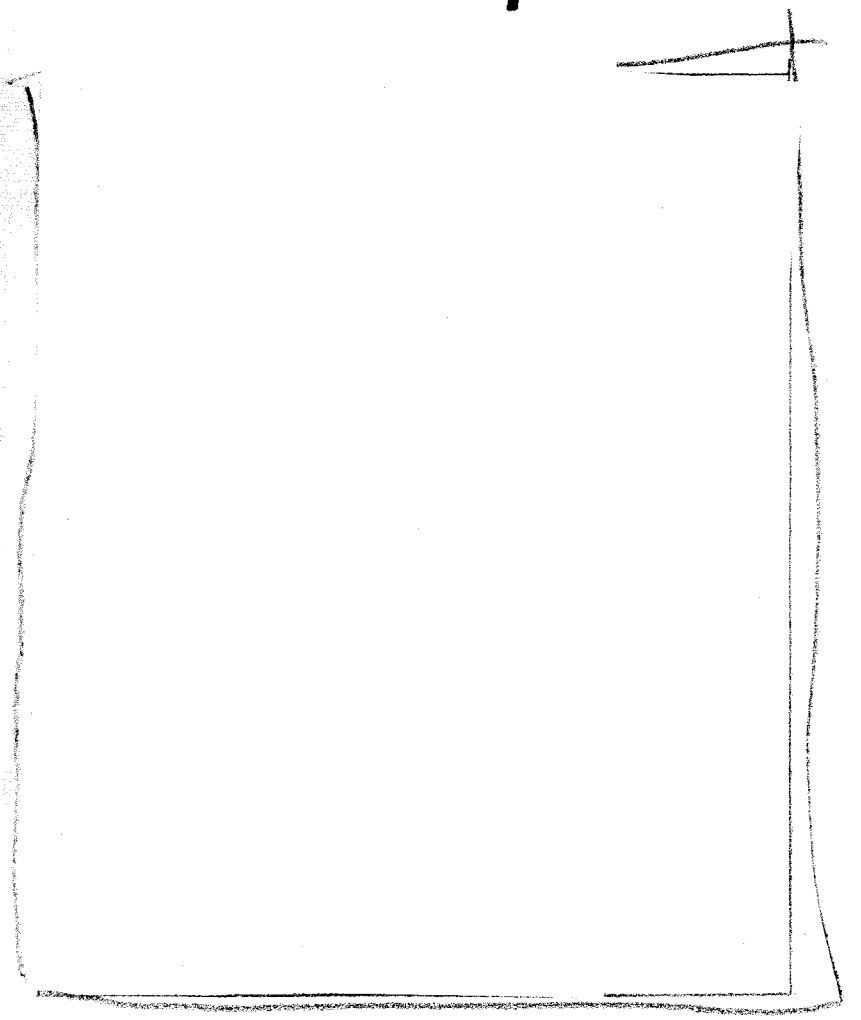

DOE
b(1)

Input for CSQGEN, run 4.

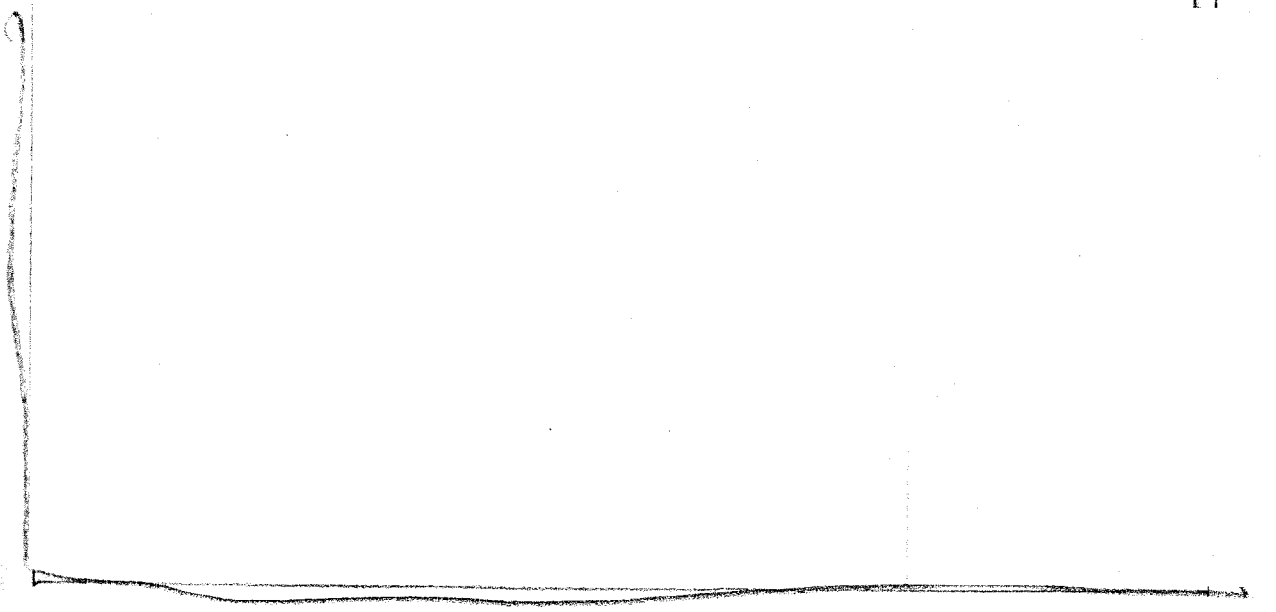

Input for CSQ, run 4.

DOE
b(1)

Input for CSQGEN, run 5.

D02
b(1)

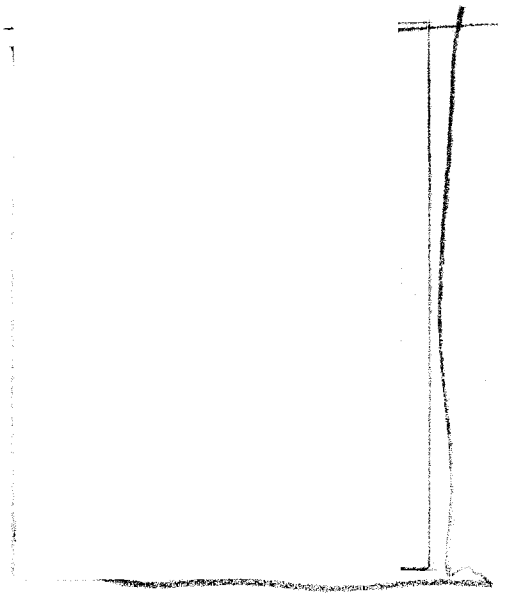

DOE
b(1)

Input for CSQGEN, run 6.

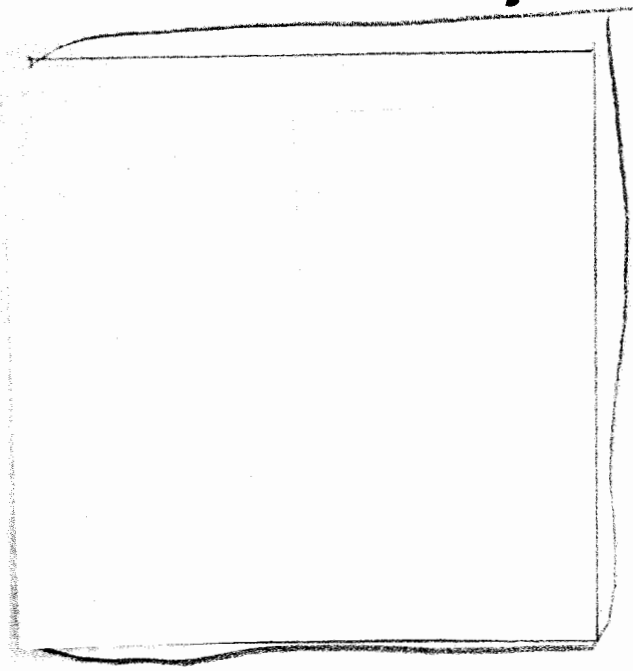

DOE
b(1)

Input for CSQGEN, run 7.

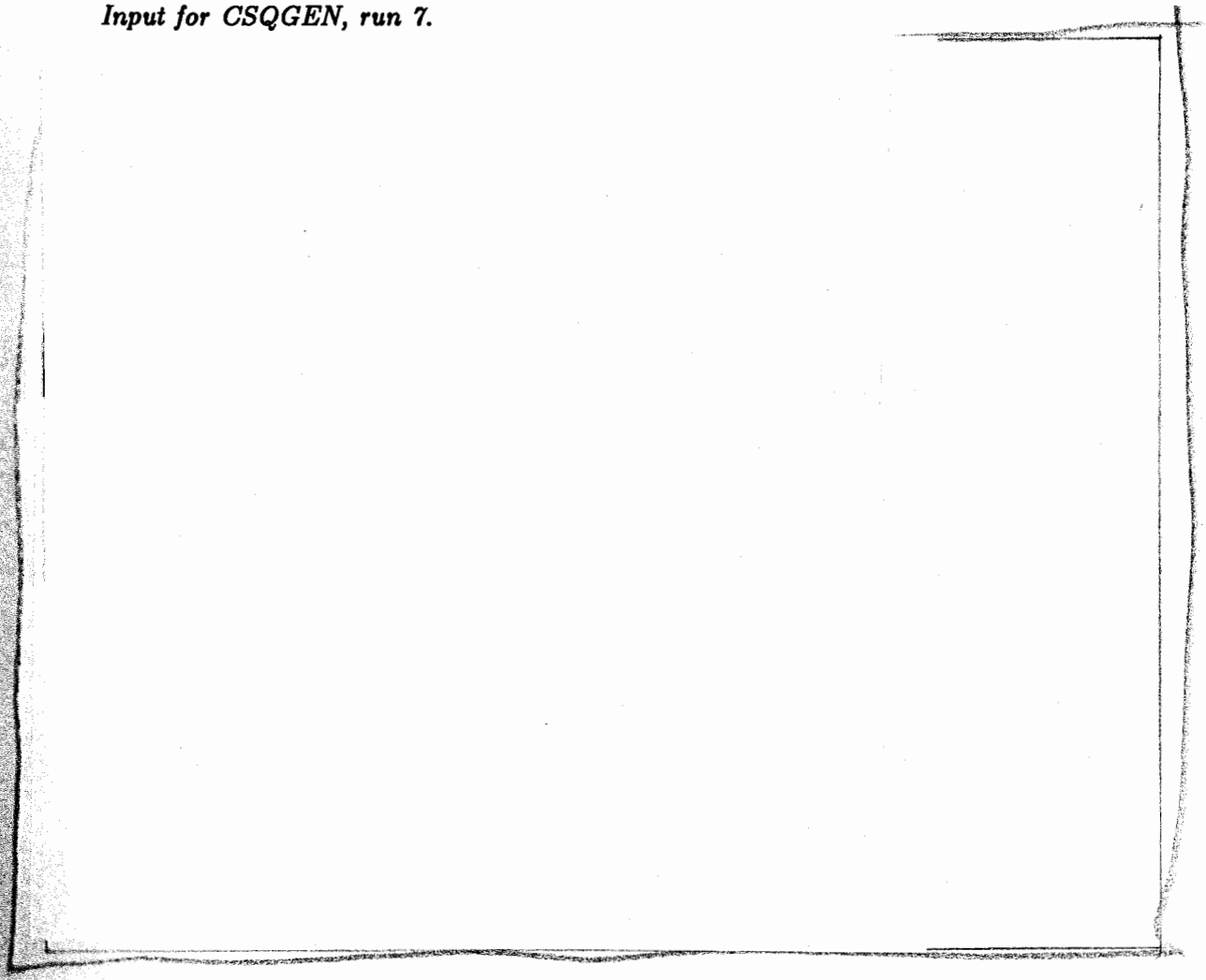

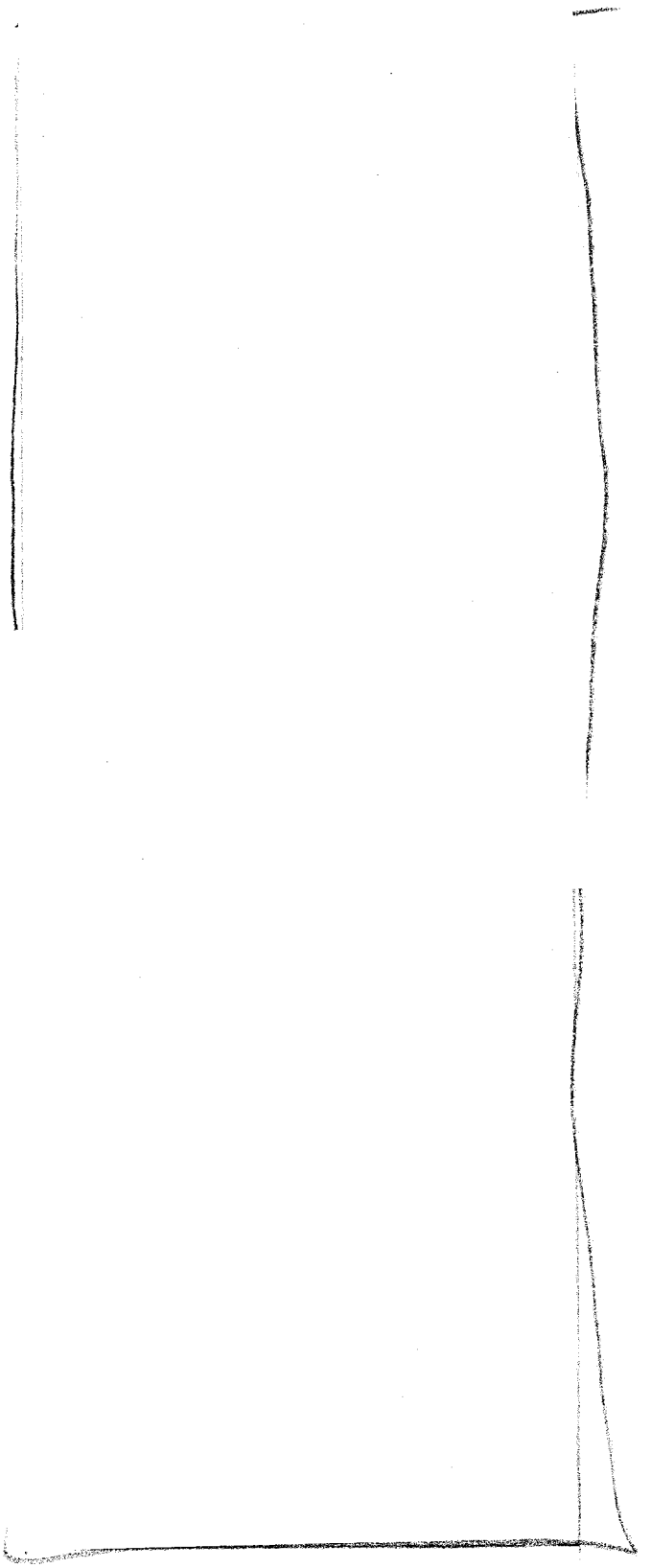

DOE
b(1)

DOE
b(1)

Input for CSQGEN, run 9.

DOE
b(1)

-1.000e+00-1.000e+00

DOE
b(1)

Input for CSQGEN, run 0.

DOE
b(1)

-1.000e+00-1.000e+00

DoE
b(1)

DOE b(1)

Input for CSQGEN, run 10.

DOE b(1)

DOE
b(1)

[redacted]

DOE
b(1)

[redacted]

APPENDIX 4. Additional Information and Plots

A few figures not included in the text are presented here, for the use of those interested in additional detail on the evolution of the ground shock with time or some other features of the calculation. The first two figures, A1 and A2, provide early time density, temperature, and velocity profiles as a function of horizontal range, starting from the center of the burst (1.13m below the ground surface). The next seven figures provide density, temperature and pressure profiles vs. depth on axis, at each decade in time from 10^{-7}s to 10^{-1}s. The next four figures provide time histories of the maximum principles stress off axis, at a range of 400m, and depths at 100m intervals. Finally, Figure A14 provides a log-log version of the depth vs. time plot of Figure 17 of the text.

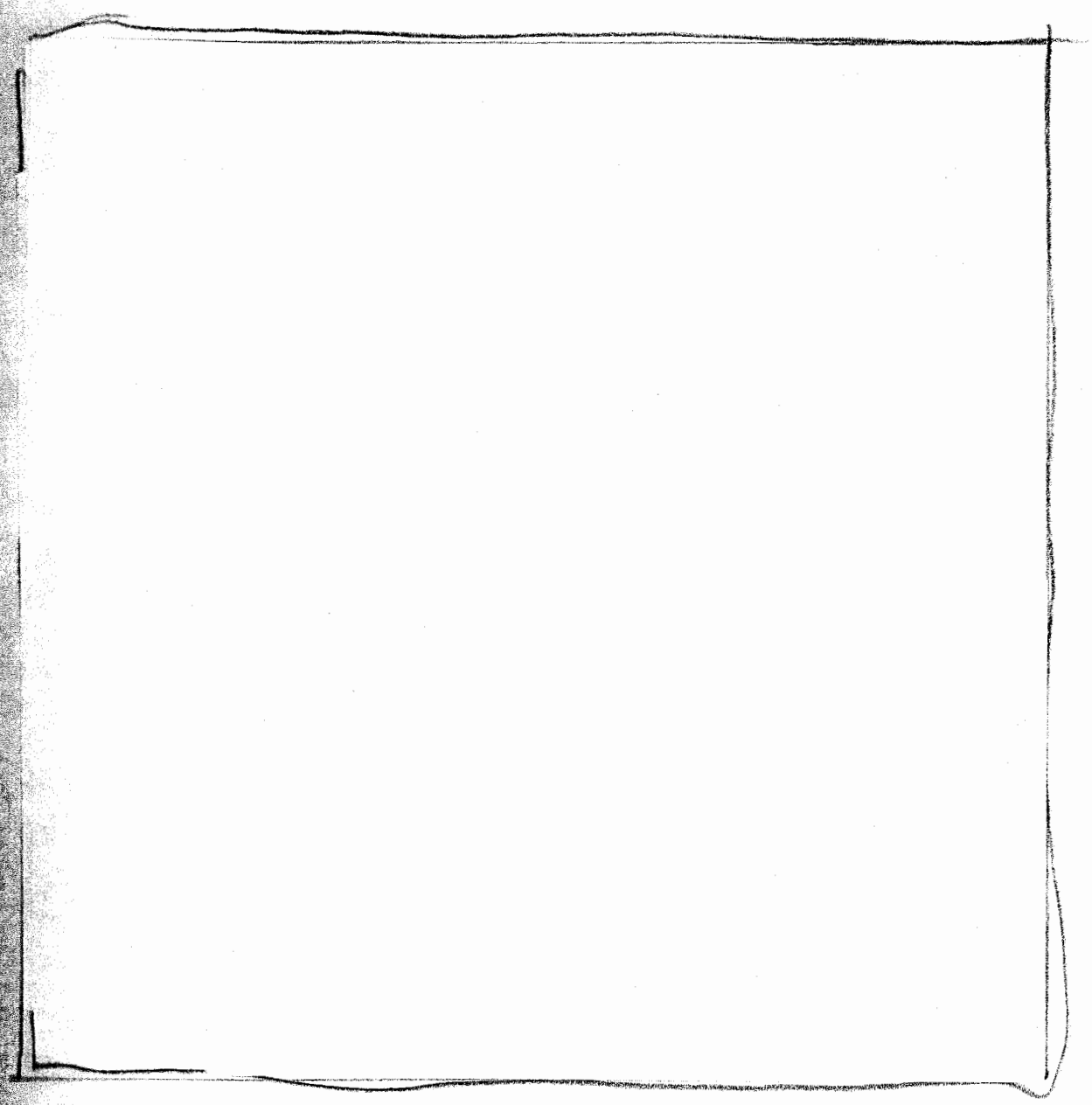

DOE
b(3)

Figure A1. Density, temperature, and horizontal velocity vs. horizontal range, at 10^{-7}s.

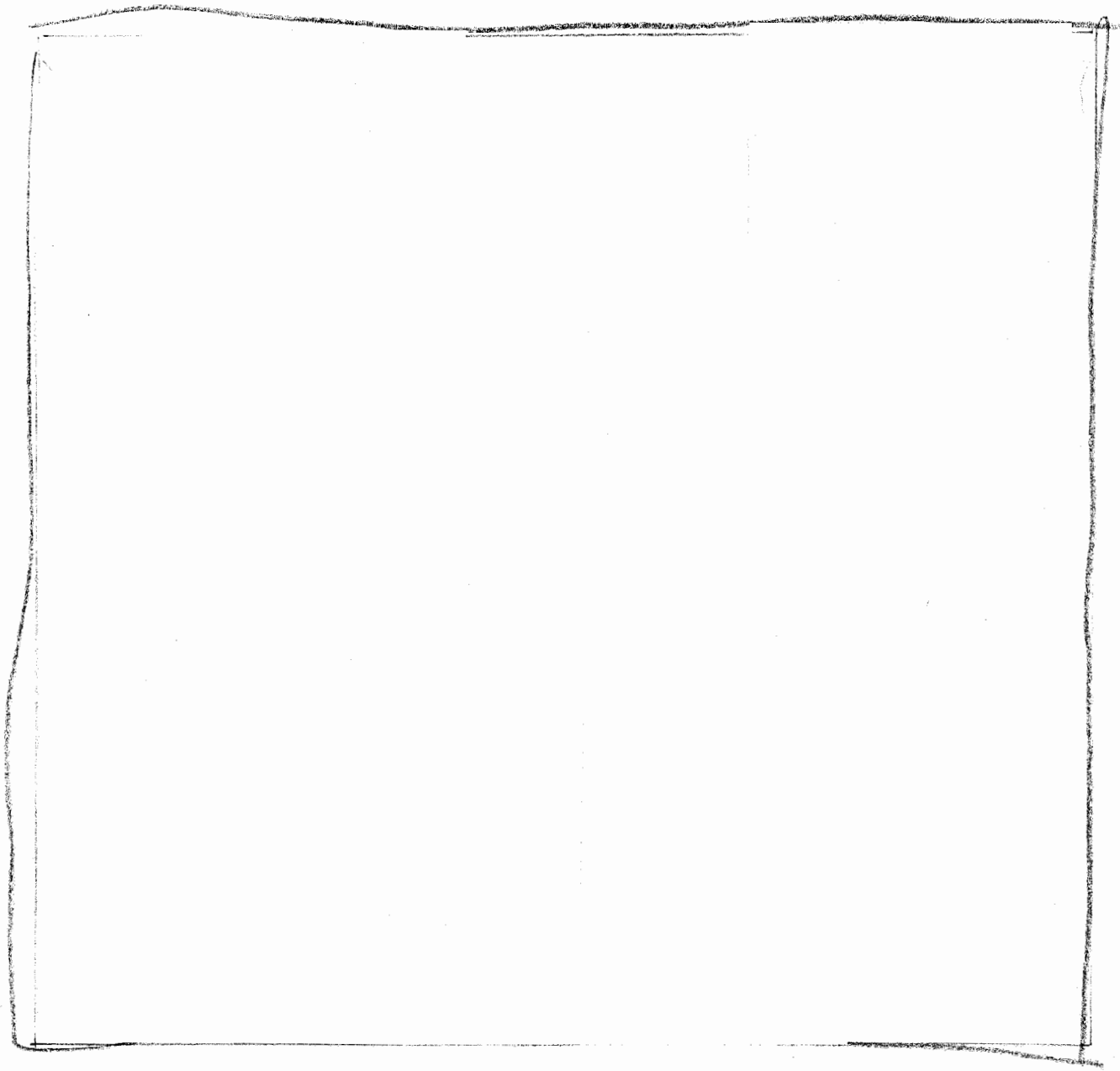

DOE
b(3)

Figure A2. Density, temperature, and horizontal velocity vs. horizontal range, at 10^{-6}s.

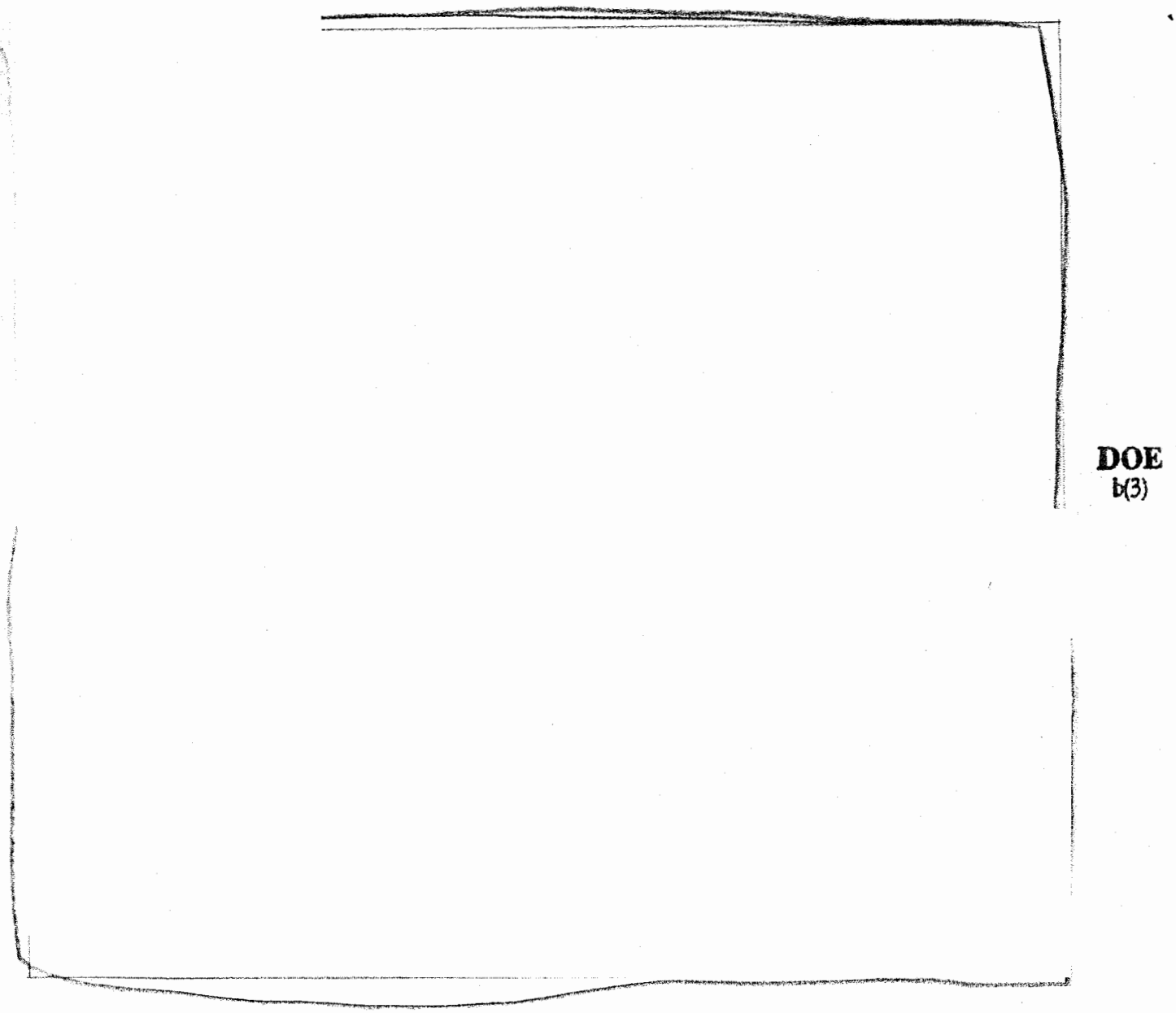

DOE
b(3)

Figure A3. Density, temperature, and pressure vs. depth on axis, at 10^{-7}s.

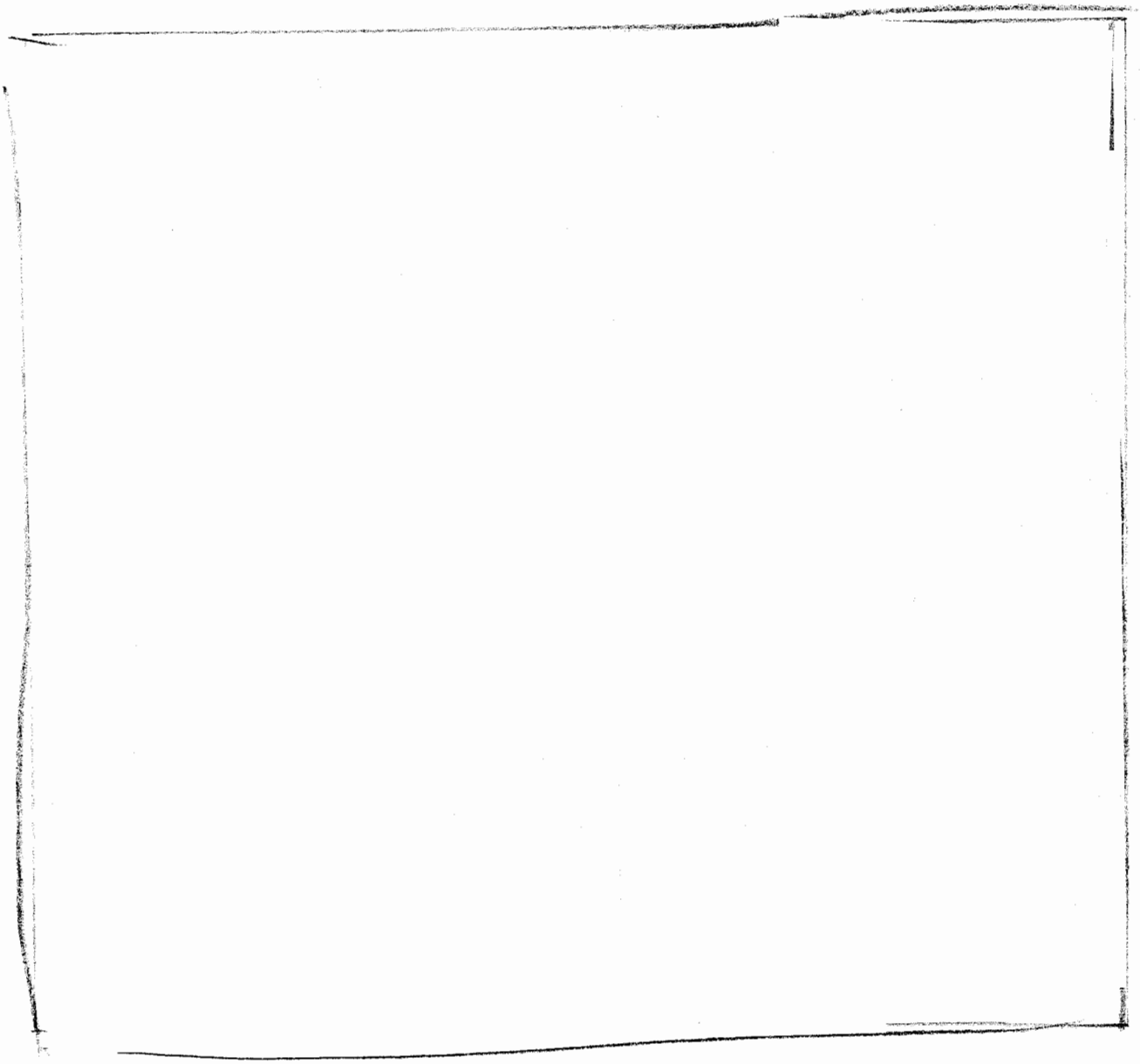

Figure A4. Density, temperature, and pressure vs. depth on axis, at 10^{-6}s.

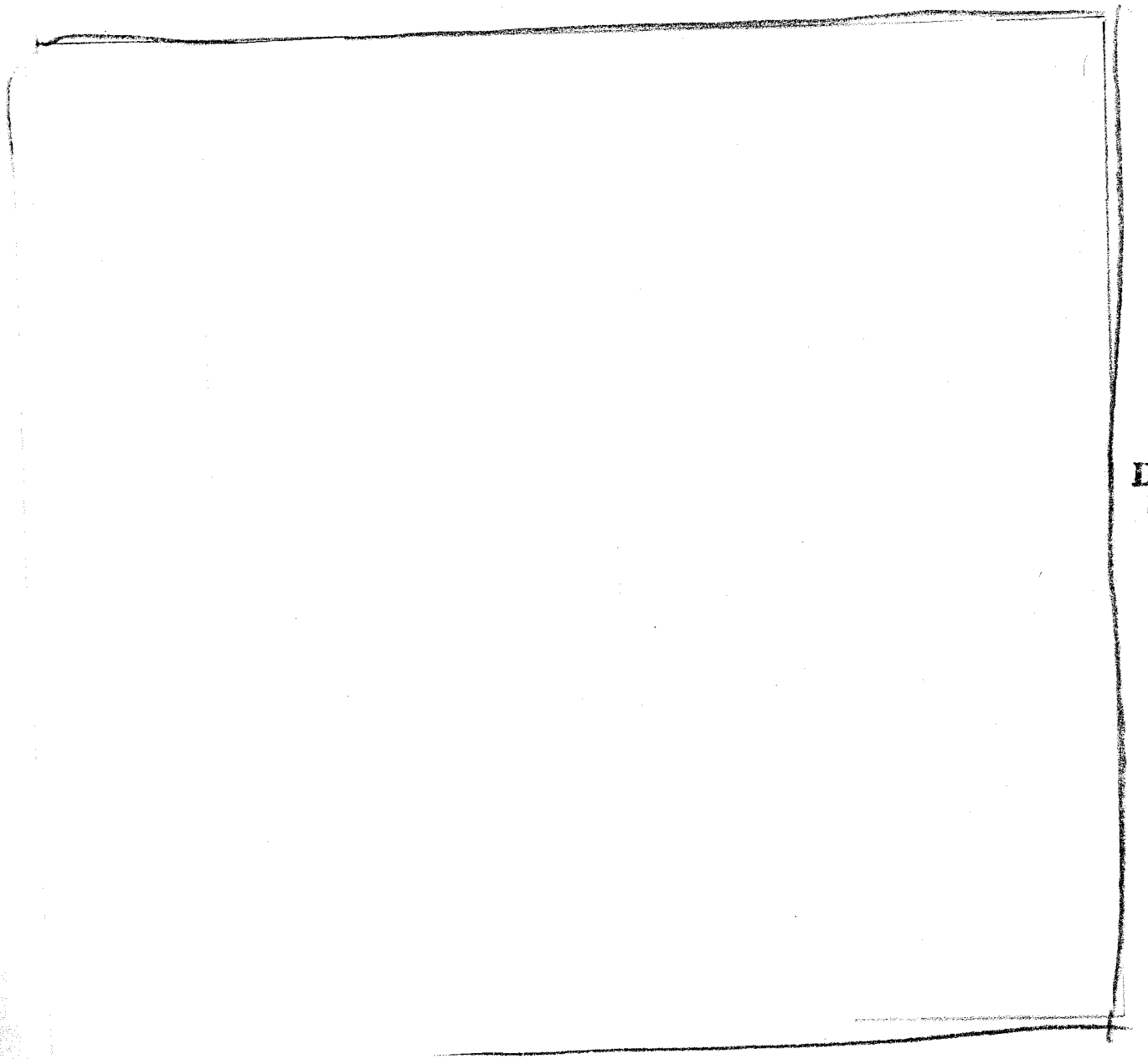

DOE
b(3)

Figure A5. Density, temperature, and pressure vs. depth on axis, at 10^{-5}s.

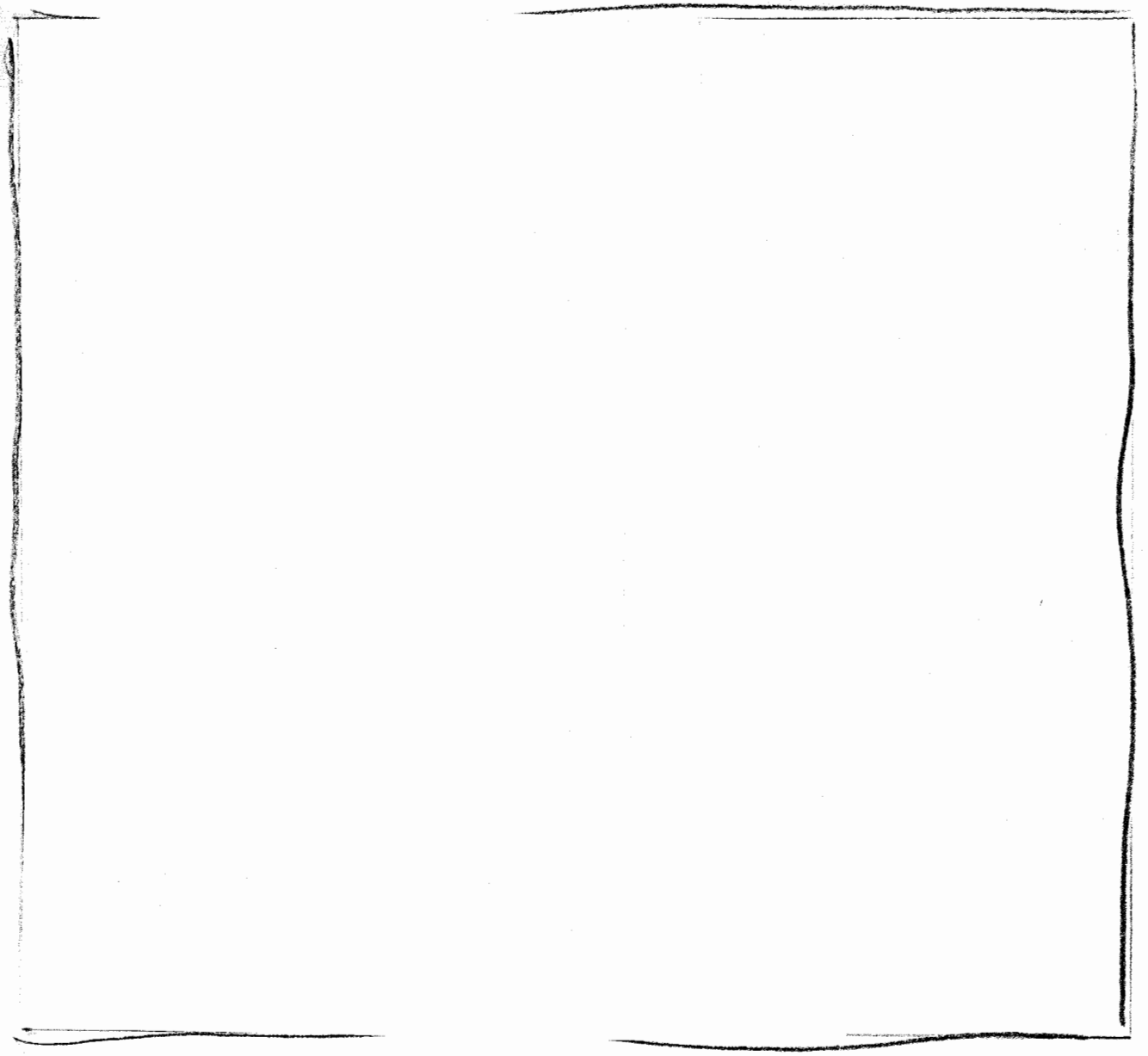

DOE
b(3)

Figure A7. Density, temperature, and pressure vs. depth on axis, at 10^{-3}s.

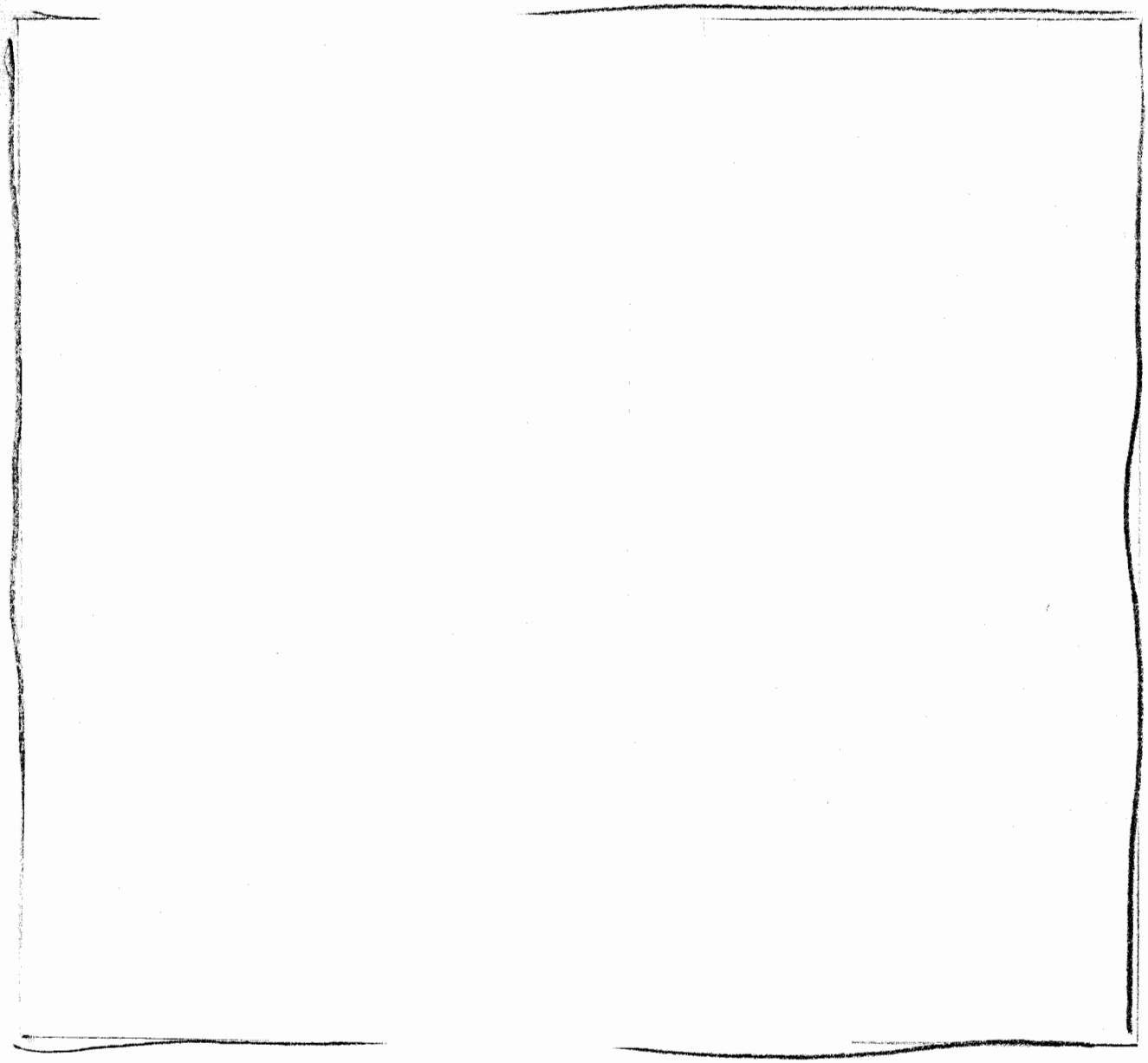

DOE
b(3)

Figure A7. Density, temperature, and pressure vs. depth on axis, at 10^{-3}s.

DOE
b(3)

Figure A8. Density, temperature, and pressure vs. depth on axis, at 10^{-2}s.

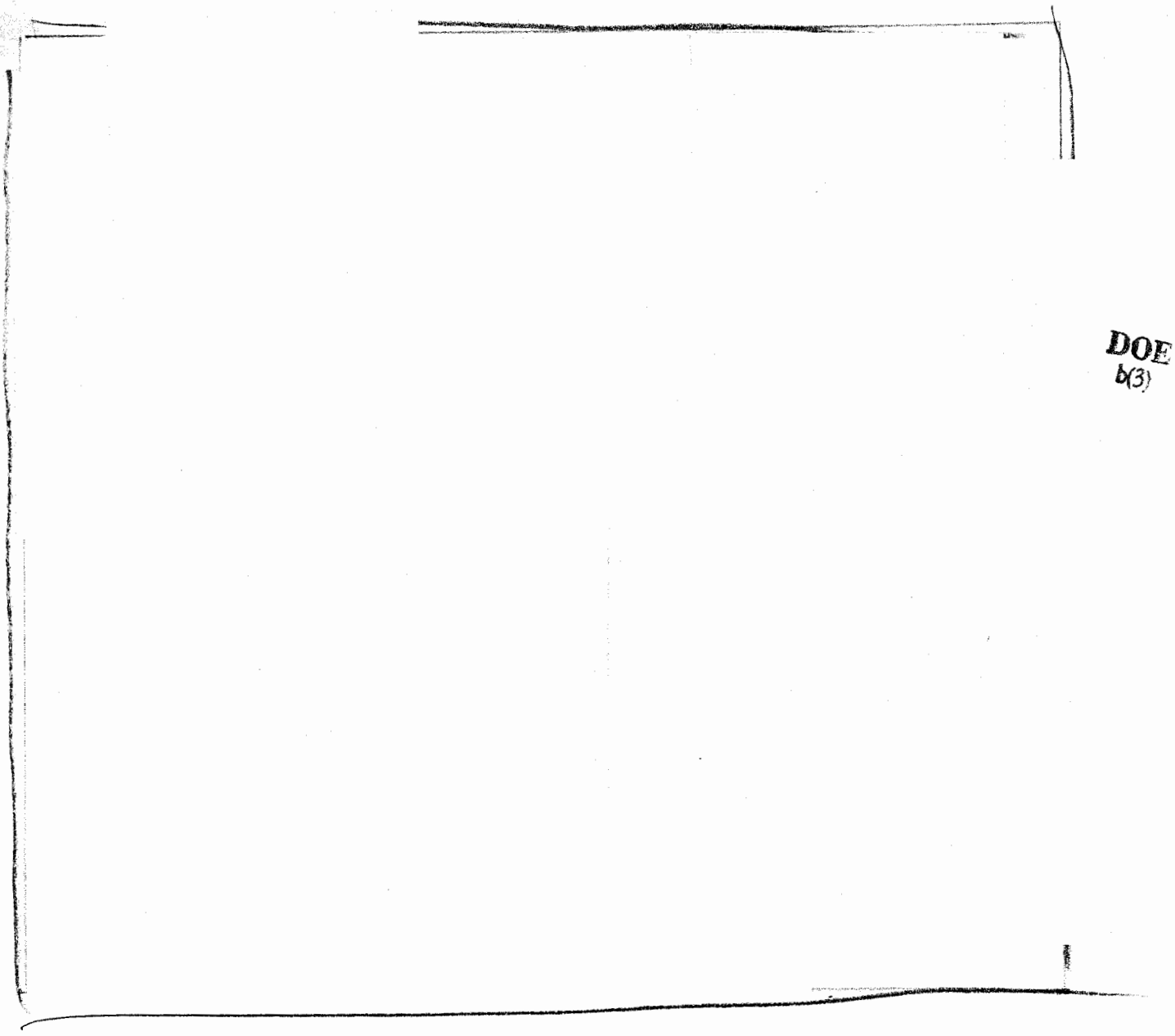

Figure A9. Density, temperature, and pressure vs. depth on axis, at 10^{-1}s.

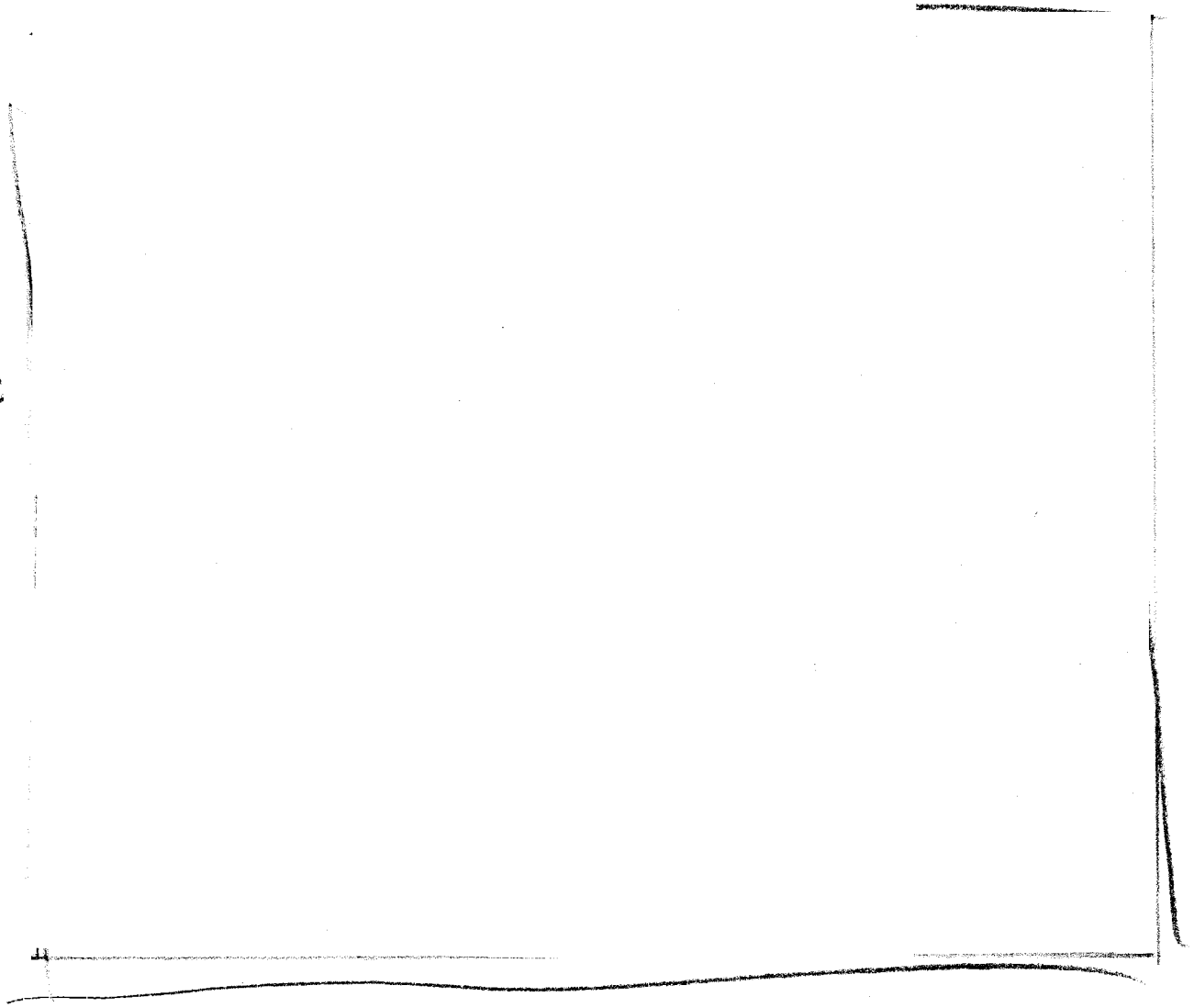

Figure A10. Maximum principle stress vs. time at 400m range and 100m depth.

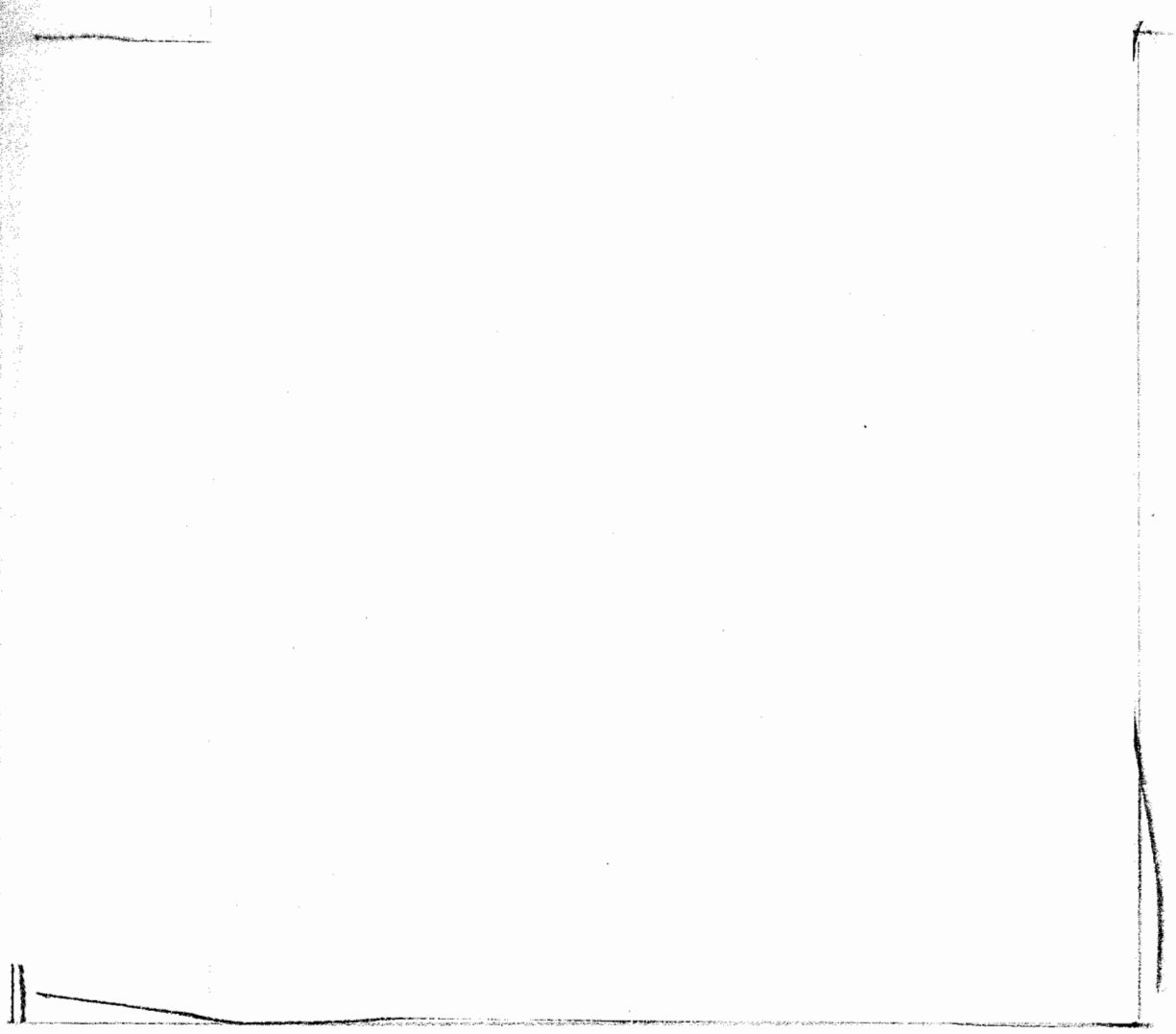

DOE
b(3)

Figure A11. Maximum principle stress vs. time at 400m range and 200m depth.

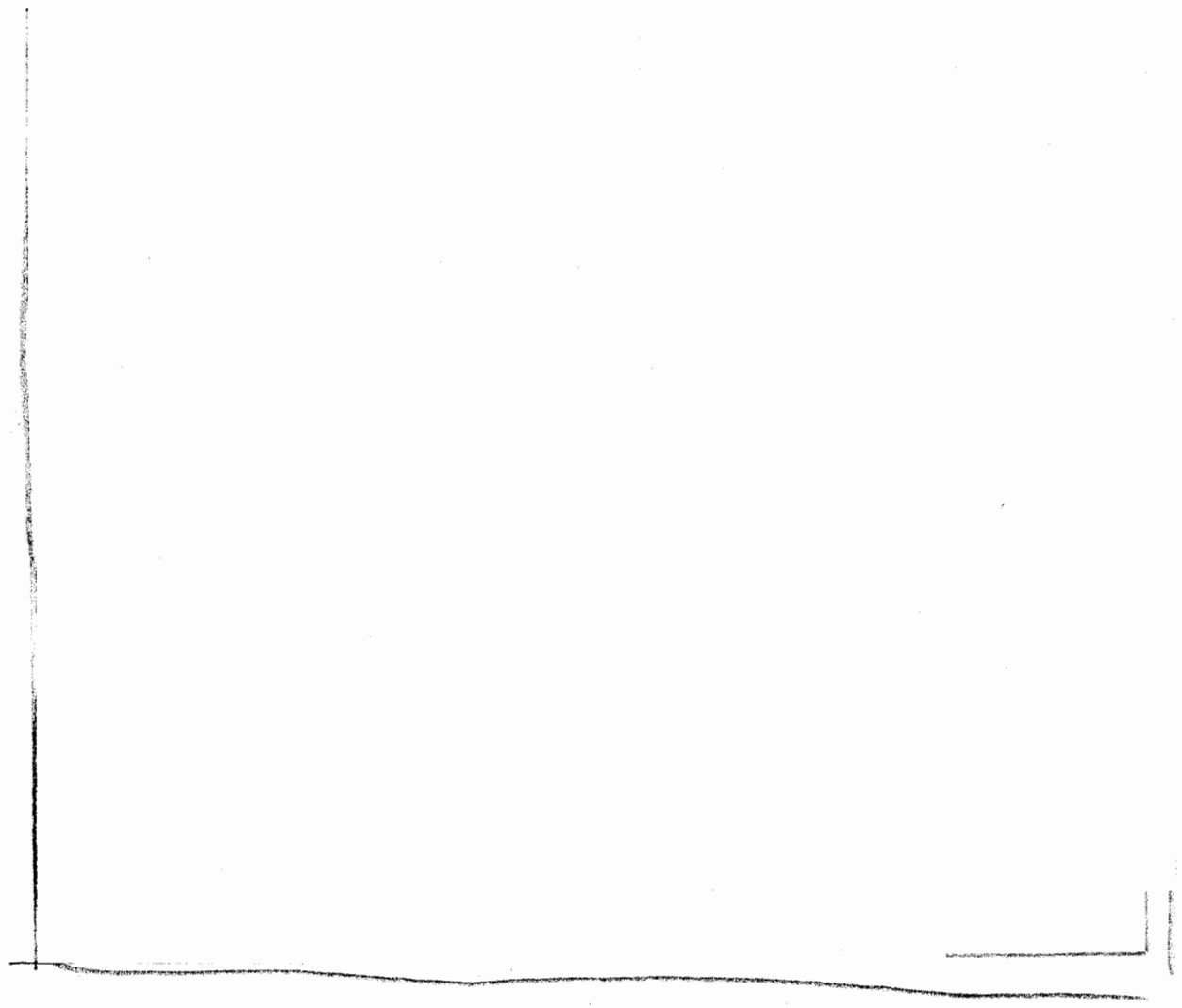

Figure A12. Maximum principle stress vs. time at 400m range and 300m depth.

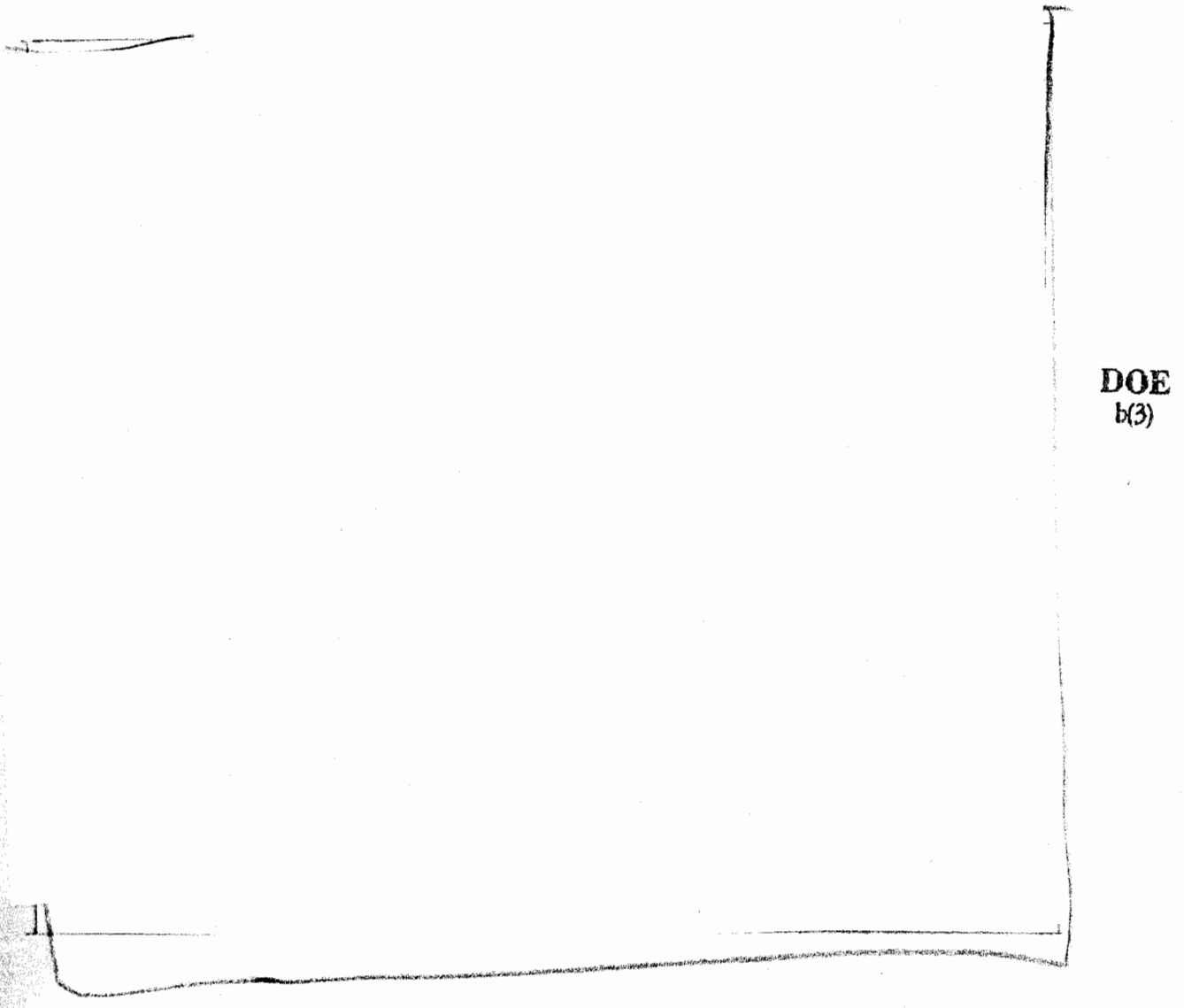

Figure A13. Maximum principle stress vs. time at 400m range and 400m depth.

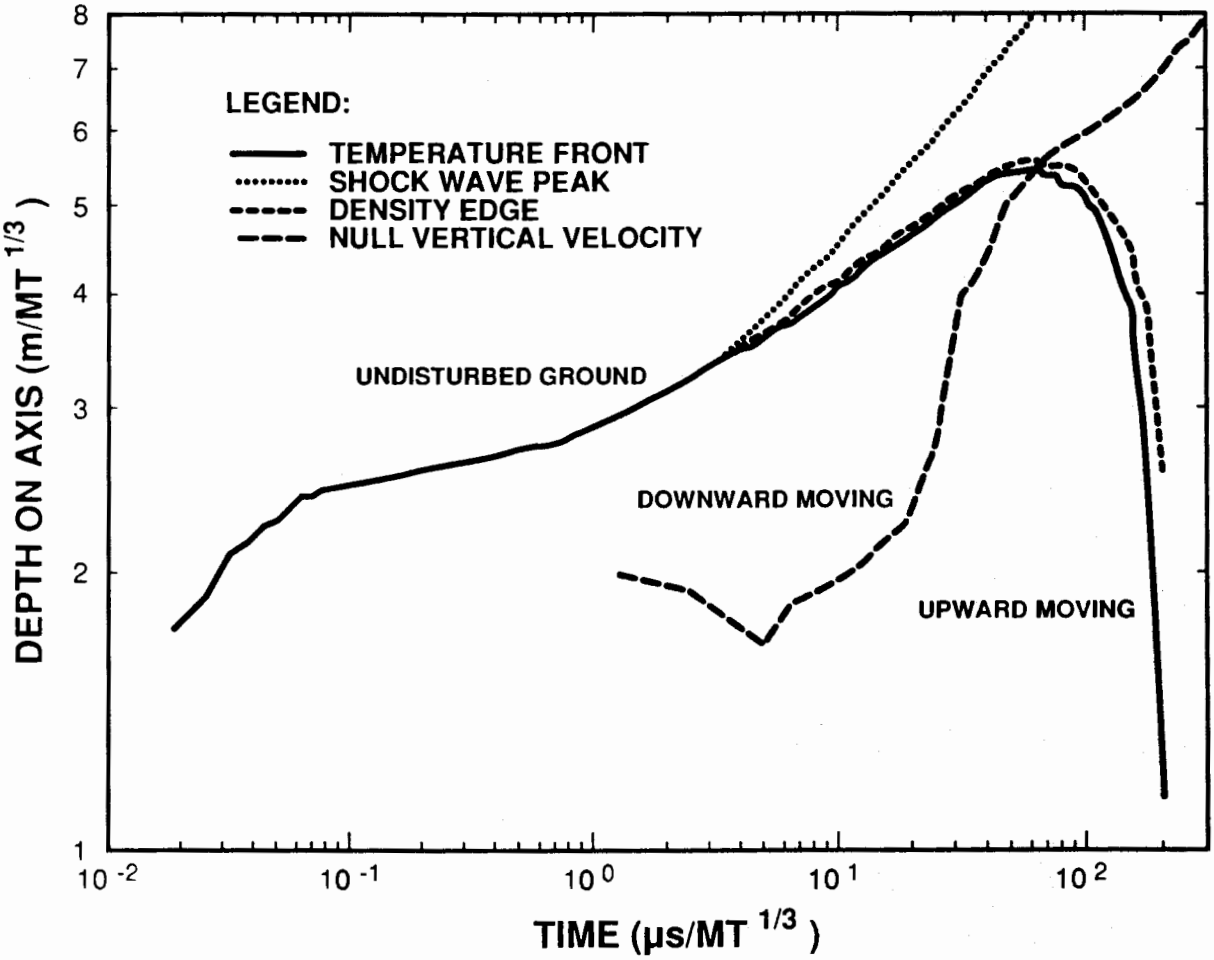

Figure A13. Plot of depth vs. time for some significant features down axis.

APPENDIX 5. Airblast: An Unsettled Issue

An intriguing feature of the airblast attenuation with range plot of Figure 14 of the text is that the rate of attenuation with range appears, on the average, to be somewhat less than that of the reduced-yield above-surface burst, as seen by the fact that at high pressures the present calculated curves lie slightly

below the Brode points while at low pressures they seem to lie slightly above the corresponding points. This feature appears to have its origin in the previously noted phenomenological difference with the above surface burst airblast: the large quantity of ground ejecta driving the airblast, in the shallow buried case.

An above-surface burst exhibits an impulsive delivery of most of the airblast energy by radiation, which forms the familiar fireball from which a shock wave subsequently emerges. In the present case, most of the energy is delivered over a much longer time interval, by the $\int pdv$ work performed on the atmosphere by the expanding column of ground ejecta. This quasi-cylindrical push against the atmosphere may result in a less rapidly attenuating shock front. The airblast from the Baker event (relatively shallow burial in ocean water) has been reported[1] to have produced a reduced attenuation rate at low pressures. Goertner[2] has suggested that the origin of the reported reduced attenuation rate might be the 2-D aspect of the air shock wave, as it develops, quasi-cylindrically, under the influence of an expanding column of water. This phenomenon could take on considerable significance in the context of aircraft delivered systems, for aircraft safety. The issue can not, at this time, be said to be resolved on the basis of either theoretical understanding, which does not clearly support the claim so far as this author has determined, or by the Baker data itself, which shows considerable scatter, and could be subject to alternative explanations.

---

[1] Norma O. Holland, *"Airblast from Underwater Nuclear Bursts (U),"* NOLTR 70-115, Naval Surface Weapon Center, White Oak, Md., 7/70.

[2] John F. Goertner, private communication with the author.

Specified External Distribution:
RS1533/89/00062, Series A, 139 pages, 78 copies, SRD, 7/1/89
SUBJECT: Relative Effectiveness of a Shallow Earth-Penetrating Nuclear Weapon (U)

Specified External Distribution:

1 – MO737 Thomas N. Dey, ESS-5, MS F665
Los Alamos National Laboratory
P. O. Box 1663
Los Alamos, NM 87545

2 – MO737 Tom Dowler, A-5, MS F602
Los Alamos National Laboratory
P. O. Box 1663
Los Alamos, NM 87545

3 – MO737 Michael Henderson, X-DO, MS B218
Los Alamos National Laboratory
P. O. Box 1663
Los Alamos, NM 87545

4 – MO737 Donald G. Shirk, X-5, MS F669
Los Alamos National Laboratory
P. O. Box 1663
Los Alamos, NM 87545

5 – MO737 Robert P. Weaver, X-2, MS B220
Los Alamos National Laboratory
P. O. Box 1663
Los Alamos, NM 87545

6 – MO737 John Kammerdiener, NWAP, MS F632
Los Alamos National Laboratory
P. O. Box 1663
Los Alamos, NM 87545

7 – MO737 Jim Conn, WT/WP, MS F631
Los Alamos National Laboratory
P. O. Box 1663
Los Alamos, NM 87545

8 – MO737 Mike O. Schick, A5, MS F602
Los Alamos National Laboratory
P. O. Box 1663
Los Alamos, NM 87545

9 – MO828 D. Clark, L-81
Lawrence Livermore National Laboratory
P. O. Box 808
Livermore, CA 94550

10 – MO828 K. Rosenkilde, L-81
Lawrence Livermore National Laboratory
P. O. Box 808
Livermore, CA 94550

11 – MO828 R. Swift, L-200
Lawrence Livermore National Laboratory
P. O. Box 808
Livermore, CA 94550

12 – MO828 Jim Kervin, L-120
Lawrence Livermore National Laboratory
P. O. Box 808
Livermore, CA 94550

13 – MO828 Harry C. Vantine, L-35
Lawrence Livermore National Laboratory
P. O. Box 808
Livermore, CA 94550

14 – MO828 Paul Chrzanowski, L-85
Lawrence Livermore National Laboratory
P. O. Box 808
Livermore, CA 94550

15 – M4470 J. Lewis
R & D Associates
P.O. Box 9295
Marina del Rey, CA 90295
ATTN: Binky Lee

16 – M4470 C. McDonald
R & D Associates
P.O. Box 9295
Marina del Rey, CA 90295

17 – M5294 K. Kreyenhagen
California Research & Technology
20943 Devonshire St.
Chatsworth, CA 91311
ATTN: A. Frederickson

18 – M5101 Robert Allen
Pacifica Technology
Div. of Science Application
P. O. Box 148
Del Mar, CA 92014

19 – M5246 H. Wilson
Science Application Int'l Corp.
10260 Campus Point Drive
San Diego, CA 92121

20 – M3296 K. D. Pyatt
S-Cubed
Division of Maxwell Labs
P.O. Box 1620
La Jolla, CA 92038-1620
ATTN: Steve Peyton

21-25 – M0654 Defense Nuclear Agency–HQTRS
ATTN: SPWE, G. Ulrich
SPWE, D. Linger
SPWE, C. McFarland
SPWE, E. Tremba
SPWE, D. Wade
6801 Telegraph Rd.
Alexandria, VA 22310-3398

26 – M0649 Commander, Field Command
Defense Nuclear Agency
ATTN: FCSAC
FOR: E. Rinehart, TD
Kirtland AFB, NM 87115-5000

27 – M1409 Strategic Systems Program Office
ATTN: B. Hannah
Department of the Navy
Washington, DC 20376-5002

28 – M1358 Joint Strategic Target Planning
Staff (JSTPS/JSMAD)
HQ/SAC
FOR: Lt. Col. Jack Strickland, JSTPS/JK
Offutt AFB, NE 68113

29 – M5253 Lt. Col. William Davis, AFCSA/Rm 10431
HQ USAF/XOXFS
Room 4D1018, Pentagon
Washington, DC 20330-5057

30 – M5200 M. J. McAlister
HQ SAC/NRE
Offutt AFB, NE 68113-5001

31 – M1946 Deputy under Secretary of Defense (S&TNF)
Room 3E130, The Pentagon
ATTN: Eugene Sevin, OUSD
Washington, DC 20301

32 – M5333 HQ BMO/MYS
ATTN: Lt. Col. A. Wassilgrim
Norton AFB, CA 92409-6468

33 – M0759 Lt. Col. L. Mills, ATSD/AE
Office of the Assistant to the Sc'ty
of Defense, (Atomic Energy)
Room 3E1074, The Pentagon
Washington, DC 20301-3050

34 – M0647 AFWL/DAA
ATTN: D. R. Fischer, WL
Kirtland AFB, NM 87117-6008

35 – M5303 ASD/VCA
ATTN: Maj. M. Heil
Wright-Patterson AFB, OH 45433-6503

Sandia Internal:

36 – 1510 J. W. Nunziato
37 – 1520 L. W. Davison
38 – 1530 D. B. Hayes
39 – 1531 S. L. Thompson
40 – 1533 P. Yarrington
41 – 1533 W. R. Davey
42-46 – 1533 A. V. Farnsworth (5)
47 – 1534 J. R. Asay
48 – 1550 C. W. Peterson
49-53 – 3141 S. A. Landenberger (5)
54-55 – 3151 W. L. Garner (2)
56 – 5110 C. C. Burks
57 – 5111 D. N. Bray
Attn: P. R. Hooper
Attn: R. E. Howell
58 – 5111 W. J. Patterson
59 – 5115 S. D. Meyer
60 – 5120 W. R. Reynolds
61 – 5150 K. D. Hardin
62 – 5151 W. C. Nickell
63 – 5160 G. R. Otey
64 – 5161 K. D. Nokes
65 – 5161 J. E. Gronager
66 – 5165 J. M. Freedman
67 – 5166 R. C. Hartwig
68 – 7110 J. D. Plimpton
69 – 7112 A. J. Chabai
70 – 8130 J. D. Gilson
71 – 8150 J. B. Wright
72 – 8170 J. W. Hickman
73 – 8524 P. W. Dean
74 – 9010 W. C. Hines
75 – 9013 W. H. Ling
76 – 9013 R. A. Paulsen
77 – 9120 M. M. Newsom
78 – 9122 R. H. Braasch

THIS PAGE INTENTIONALLY LEFT BLANK